

Dissertation
submitted to the
Combined Faculties for the Natural Sciences and for Mathematics
of the Rupertus-Carola University of Heidelberg, Germany
for the degree of
Doctor of Natural Sciences

presented by

Dipl.-Phys. Stephen Koszudowski
born in Bad Soden/Ts., Germany

Oral examination: 08.07.2009

Developments for the HITRAP Cooler Trap and mass measurements around $A = 96$ at SHIPTRAP

Referees: Priv. Doz. Dr. Wolfgang Quint
Prof. Dr. Andreas Wolf

Developments for the HITRAP Cooler Trap and mass measurements around $A = 96$ at SHIPTRAP Die HITRAP-Anlage (Highly charged Ions Trap - Falle für hochgeladene Ionen) wird zur Zeit an der GSI in Darmstadt aufgebaut und in Betrieb genommen. Sie wird Bündel von 10^5 hochgeladenen schweren Ionen, z.B. wasserstoffartigem Uran (U^{91+}), für hochpräzise atomphysikalische Experimente zur Verfügung stellen. Die Ionen werden vom GSI-Beschleunigerkomplex produziert und im Experimentierspeicherring auf 4 MeV/u abgebremst. Ein zweistufiger Linearabbremsler entschleunigt die Ionen dann auf 6 keV/u. Die erste Abbremsstufe auf 500 keV/u wurde erfolgreich in Betrieb genommen. Die abgebremsten Ionen werden in eine Penning-Falle injiziert (die Kühlerfalle), wo sie mit Hilfe von Elektronen- und Widerstandskühlen auf 4 K abgekühlt werden. Resonante Schwingkreise zum zerstörungsfreien Nachweis und zum Widerstandskühlen der gefangenen Teilchen wurden konzipiert und getestet. Die Zeitsteuerung des Fallenzyklus (Ionen-Einfang, Kühlen, Extraktion) mit einer Auflösung von 25 ns wurde in das Kontrollsystem *CS* integriert. *CS* wird auch an der Massenmessungs-Penning-Falle SHIPTRAP verwendet, wo die neue Zeitsteuerung erfolgreich genutzt wird. SHIPTRAP vermisst radioaktive Ionen, die in Fusions-Evaporations-Reaktionen am Geschwindigkeitsfilter SHIP produziert werden. Die Massen von 9 Nukliden ($^{93,94,95}\text{Technetium}$, $^{94,96}\text{Ruthenium}$, $^{95,96,97,98}\text{Rhodium}$) nahe der Stabilität wurden präzise vermessen und mit der Atomaren Massen Evaluation verglichen. Der Nachweis von isomeren Zuständen mit SHIPTRAP wurde untersucht.

Developments for the HITRAP Cooler Trap and mass measurements around $A = 96$ at SHIPTRAP The HITRAP (Highly charged Ions Trap) facility is currently being set up and commissioned at GSI in Darmstadt. It will provide bunches of 10^5 heavy highly-charged ions, for example hydrogen-like uranium (U^{91+}), to high-precision atomic physics experiments. The ions are produced by the GSI accelerator complex and decelerated to 4 MeV/u in the Experimental Storage Ring. Then the ions are decelerated by a two-step linear decelerator down to 6 keV/u. The first deceleration step down to 500 keV/u was successfully commissioned. The decelerated ions are injected into a Penning trap (the Cooler Trap), where they are cooled to 4 K by electron and resistive cooling. Resonant circuits for non-destructive detection and the resistive cooling of the trapped particles were designed and tested. The time control of the trap-cycle (trapping, cooling, extraction) with a time resolution of 25 ns was implemented into the control system *CS*. *CS* is also used at the mass measurement Penning trap SHIPTRAP, where the new time control is successfully operated. SHIPTRAP measures radioactive ions stemming from fusion evaporation reactions at the velocity filter SHIP. The masses of 9 nuclides ($^{93,94,95}\text{Technetium}$, $^{94,96}\text{Ruthenium}$, $^{95,96,97,98}\text{Rhodium}$) near the line of stability were precisely measured and compared with the Atomic Mass Evaluation. The detection of isomeric states with the present SHIPTRAP set-up was studied.

for $N^2 + x$

It is a mistake to think you can solve any major problems just with potatoes.

Douglas Adams

Contents

1	Introduction	1
2	HITRAP and SHIPTRAP within GSI	7
2.1	Penning trap basics	7
2.2	Ion production at GSI	10
2.2.1	Production of highly charged ions	10
2.2.2	The accelerator complex at GSI	12
2.3	The SHIPTRAP facility	12
2.3.1	The velocity filter SHIP	12
2.3.2	The SHIPTRAP gas cell	15
2.3.3	The RFQ buncher and transfer section	17
2.3.4	The SHIPTRAP Penning traps	18
2.4	The HITRAP facility	21
2.4.1	Overview	21
2.4.2	The Double-Drift-Buncher and the IH-Linac	23
2.4.3	The Radio Frequency Quadrupole Decelerator	27
2.4.4	The Low Energy Beam Transport (LEBT)	28
2.4.5	The Cooler Trap	31
2.4.6	The Vertical Beamline and EBIT	32
2.4.7	HITRAP experiments	34
3	The HITRAP Cooler Trap	37
3.1	The design of the HITRAP Cooler Trap	37
3.1.1	Working cycle of the Cooler Trap	39
3.2	Ion detection and manipulation at HITRAP	41
3.2.1	FT-ICR	41
3.2.2	Cooling of the ion motion	43
3.3	Cryogenic electronics	45
3.3.1	The electronics box	46
3.3.2	The coils	47
3.3.3	Cryogenic preamplifier	58
3.3.4	Filters	60
3.4	Room temperature electronics	64
3.4.1	Power supplies	64
3.4.2	Detection electronics	64

4	Cooler trap control system	67
4.1	Trap cycle	67
4.2	Control system	69
4.2.1	Requirements on the control system	69
4.2.2	<i>CS</i>	69
4.2.3	Implementation of the <i>CS</i> -system	70
4.3	The interface to the timing system	71
4.4	The timing system	71
4.4.1	Requirements on the timing system	71
4.4.2	The NI PCI-7811R FPGA card	72
4.4.3	Design of the timing system	73
4.4.4	Implementation and performance	75
5	On-line mass measurements at SHIPTRAP around $A = 96$	79
5.1	Experimental results	82
5.2	Data analysis procedure	85
5.3	Data Evaluation and Atomic Mass Evaluation	87
5.3.1	Statistical analysis on the resolving power of the two- resonances fit	90
5.3.2	Discussion of the isomeric state admixtures	103
5.4	Discussion of the obtained results	105
5.4.1	Comparison between this work and the Atomic Mass Evaluation	105
5.4.2	Discussion of the results	107
6	Summary, conclusions and outlook	109
A	Fast-Fourier-Transformation	113
B	Detailed description of the timing software	115
	Bibliography	121
	Acknowledgments	135

List of Tables

2.1	Calculated performance of the decelerator elements.	23
3.1	Q-factors from the measurement of the 440 kHz coil	53
3.2	Q-factors from the measurement of the 35 MHz coil	57
3.3	Amplification of the cryogenic amplifier with respect to the bias voltages	61
5.1	Half-life, spin and parity of the measured nuclides	82
5.2	Experimental results	84
5.3	Atomic mass results	89
5.4	Results of the statistical analysis on the isomer resolution for the spectra without jitter	96
5.5	Results of the two resonances fit with distance and weight running .	96
5.6	Results for the statistical analysis on the isomer resolution for spectra with jitter	99
5.7	Results of the t-test on the mean χ^2 of the single and the two reso- nances fit	100

List of Figures

1.1	Regions of the nuclear chart addressed by SHIPTRAP	2
1.2	Electrical field strength in low-lying states of hydrogen-like ions. . .	4
2.1	Penning trap schematics	8
2.2	Ion motions in a Penning trap	9
2.3	Compensated cylindrical Penning trap	10
2.4	Overview of the GSI accelerator complex.	11
2.5	Overview on the SHIPTRAP facility.	13
2.6	Overview of the SHIP velocity filter.	14
2.7	The SHIPTRAP gas cell.	15
2.8	Schematic of the SHIPTRAP RFQ buncher.	17
2.9	Schematic of the SHIPTRAP transfer section.	18
2.10	Schematic of the SHIPTRAP Penning traps.	19
2.11	Time-of-flight resonance.	20
2.12	HITRAP overview	22
2.13	The Double Drift Buncher	24
2.14	The IH-linac	25
2.15	Decelerated beam after the IH-linac	26
2.16	The radio-frequency quadrupole	27
2.17	Velocity independent ion loss due to charge exchange	28
2.18	Electrostatic potential and magnetic flux on the LEBT axis	29
2.19	The LEBT installed in the reinjection channel	30
2.20	LEBT Einzel-lens	30
2.21	Nested trap configuration of the Cooler Trap	31
2.22	The Vertical Beam Transport	33
3.1	Working cycle of the Cooler Trap	40
3.2	Electron cooling of 10^5 U^{92+} ions	44
3.3	The electronics box	47
3.4	The axial frequency coil	48
3.5	The cyclotron frequency coil	50
3.6	Q-measurement set-up	51
3.7	Example for a resonance for the transmission-type Q-measurement .	52
3.8	Mechanical set-up of the 440 kHz coil	53
3.9	Cross- and basket-winding technique for coils	54
3.10	Reflection-type measurement in the Smith-chart	56
3.11	The cryogenic preamplifier	59
3.12	Amplification versus gate 1 voltage	60
3.13	Amplification versus frequency	61

3.14	Schematic of the noise filter for the electrodes	62
3.15	Transmission curve of the noise-filter: Comparison of simulation and measurement	63
3.16	Rise time test of the noise-filter	63
4.1	Example of a timing sequence	68
4.2	The trap control architecture	70
4.3	Sequence diagram of the FPGA_HI class	73
4.4	State diagram of the FPGA_VI state machine	74
5.1	Isomeric state configurations.	80
5.2	Nuclear chart displaying the nine measured isotopes	81
5.3	Cooling resonances in the purification trap for ions with mass $A = 96$	83
5.4	Comparison of the frequency ratios obtained in both beamtimes	87
5.5	Mass results without isomeric correction	88
5.6	Mass results with isomeric correction	88
5.7	Location of the artificial isomeric state resonances	91
5.8	Overview on the spectrum creation for the statistical analysis	93
5.9	Results for the statistical analysis on the isomer resolution (-0.5 Hz and -0.8 Hz)	97
5.10	Results for the statistical analysis on the isomer resolution (-1.1 Hz and -1.5 Hz)	98
5.11	Results for the statistical analysis on the isomer resolution for spectra with jitter (-0.5 Hz and -0.8 Hz)	101
5.12	Results for the statistical analysis on the isomer resolution for spectra with jitter (-1.1 Hz and -1.5 Hz)	102
B.1	Screenshot of the timing information in the MM6.cpp	117

Horror vacui

Into the pit
into the darkness
into the trap
into the cold

Frostbite
I'm slowing
down
My legs
give in

I
am
frozen

Ravens Grave

Chapter 1

Introduction

Precise mass measurements deliver important input information in various domains in physics. The most striking examples are the element synthesis in stars and the mapping of the boundaries of the nuclear chart. Today's abundance of heavy elements (i.e. elements heavier than iron, where fusion does not release energy any more) in the universe can be explained by various stellar production paths. All these theoretical paths depend strongly on parameters as Q-values, branching ratios and decay constants, obtained from experiments and extrapolations. A precise knowledge of the proton separation energy of nuclides near the proton drip-line is needed to validate the models for the rp-process, for example. At the endpoint of the rp-process precise mass measurements provide essential information, especially when spectroscopic investigations are not possible [Sch98].

The precise location of the borderline of nuclear stability is a second important question in nuclear physics. Whereas the neutron drip-line can be accessed experimentally only for very light elements, the proton drip-line is approachable even for heavy nuclei [Woo97]. The experimental challenge in determining, whether an isotope is proton unstable or not, lies in the discrimination of the direct proton-decay and the competing β -decay. On the one hand, the proton-decay might have a comparatively low branching ratio, if it has a small Q-value and therefore a long partial half-life. On the other hand, it is very hard to discriminate the low energy protons against a high background from the β -decay. Because of these effects, proton emitters are found mostly at some distance to the proton drip-line and are therefore not suitable to retrace the drip-lines position accurately.

Furthermore, high-precision mass measurements can resolve isomeric states of isotopes and hence determine their excitation energy, even in regions of the nuclear landscape that are hardly accessible for other techniques. This can provide a valuable input in nuclear structure models [Wal06].

Other fields, where the precise knowledge of nuclear masses is crucial, are weak interaction studies in super-allowed β -decays [Har05], CPT tests by com-

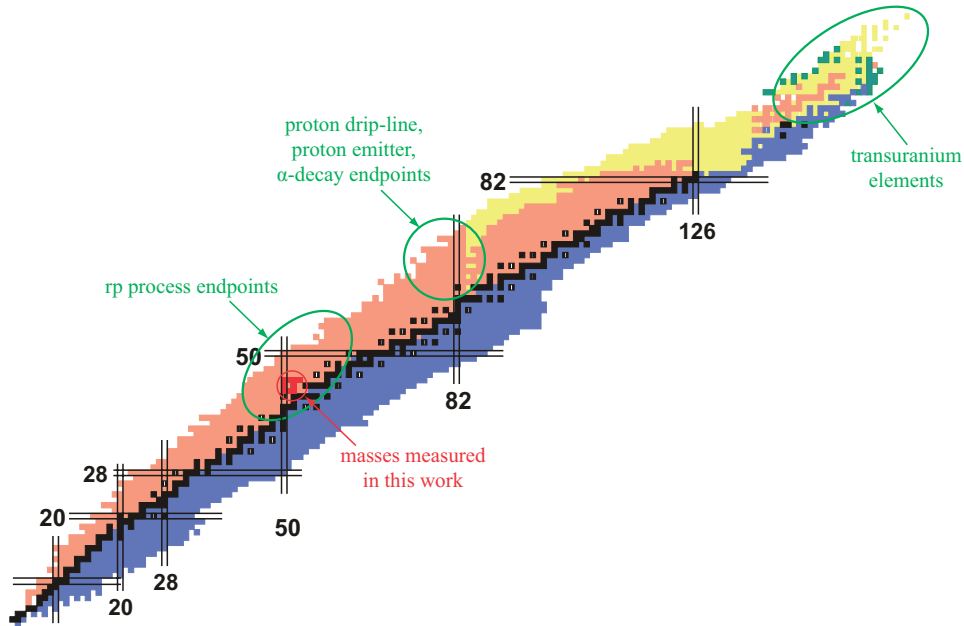


Figure 1.1: Regions of the nuclear chart addressed by SHIPTRAP. The masses measured in this work are marked in red.

parison of the masses of particles and their antiparticles [Gab99b] and many others [Sch06b, Lun03, Bla06]. Finally, new experimental ideas for the measurement of the neutrino mass depend on the input from high-precision mass measurements [Klu07a].

Depending on the type of investigation, the required precision ranges from 10^{-5} (molecular mass spectroscopy) to 10^{-11} (CPT and QED tests). The most precise mass measurements with relative uncertainties of $8 \cdot 10^{-9}$ for radioactive [Bol06] and $1 \cdot 10^{-11}$ for stable ions [Dyc04] were performed in Penning traps.

In the near future two Penning traps dedicated to mass spectrometry will be available at GSI. The future five-fold Penning trap at HITRAP and the already running SHIPTRAP facility. The latter investigates radioactive ions produced in fusion evaporation reactions at the velocity filter SHIP. The produced neutron-deficient isotopes range from medium-heavy to transuranium elements. Figure 1.1 shows the three regions of main interest for investigations at SHIPTRAP. The region below ^{100}Sn is the assumed end of the rp-process in the tin-antimony-tellurium cycle [Sch01]. Here, precise mass values are needed to deduce the proton separation energies. In this work the masses of isotopes in this region were measured. The transuranium region is of special interest, since here many masses are only known from extrapolations, which become more and more imprecise when moving away from experimentally determined masses [Wap03]. Since many of these masses are linked by well-known α -decay chains, pinning down one mass value has a big effect.

The quest for the determination of the neutrino mass motivates new ultra-precise mass measurements [Nov09]. The mass of the antineutrino is known to an upper limit of 2 eV. This value is obtained by determining the endpoint of the tritium β -decay spectrum. But the upper limit of the neutrino mass - deduced from internal bremsstrahlung spectra from the electron capture decay of ^{163}Ho - is still at 225 eV. In electron capture decays the total energy of the neutrino - including its rest mass - equals the mass difference of the mother and the daughter nuclei minus the electron binding energy. Therefore a precise knowledge of the masses will open a door to the neutrino mass.

Due to its small electron capture decay Q-value, ^{163}Ho is by now the most favorable candidate for this type of neutrino mass determination. Penning trap mass spectrometers like SHIPTRAP at GSI and ISOLTRAP at CERN can investigate the suitability of other possible candidates. The five-fold Penning trap dedicated to ultra-precise mass measurements at HITRAP can then determine the masses of the candidates to an uncertainty of 1 eV [Klu07a].

But HITRAP will also address several other fields in physics apart from mass spectrometry. The HITRAP facility itself is dedicated to trap and cool highly charged ions coming from the GSI accelerator chain down to the sub-meV range before delivering them to experiments [TDR03]. These experiments include the already mentioned high-precision mass measurements and high-precision g -factor measurements as well as collision studies between slow ions and atoms and between slow ions and surfaces, looking for new effects [Her06, Klu07].

The highly charged ions provided by HITRAP give the unique possibility to perform high-accuracy tests of quantum electrodynamics (QED), which is one of the best confirmed theories in physics. The perturbative QED reaches its impressive predictive power from very low relative uncertainties in the calculated observables. The g -factor of the free electron has been calculated to a relative accuracy in the order of 10^{-13} [Kin06]. Other examples are the atomic levels of the hydrogen atom and of few-electron atoms, where many-body effects can be neglected [Pac96, Pac98]. QED uses the fine-structure constant $\alpha \approx 1/137$ as perturbation term. Inter-particle interactions in light atoms can be expanded as a function of $Z\alpha$, which limits the precision of the calculation only by the finite size of the nucleus. For heavy, highly charged ions, this expansion breaks down. In these systems the term $Z\alpha$ becomes comparable to 1, so that it cannot longer be used as perturbation term [Moh98, Moh08] (see figure 1.2). This is the so-called strong-field regime, since the electromagnetic fields of heavy nuclei are extremely high. The $1s_{1/2}$ electron of uranium sees an electric field in the order of 10^{16} V/cm, which is close to the Schwinger limit, where spontaneous production of an electron-positron pair is possible. To explore this regime, non-perturbative techniques in QED have been developed [Moh98, Bei00].

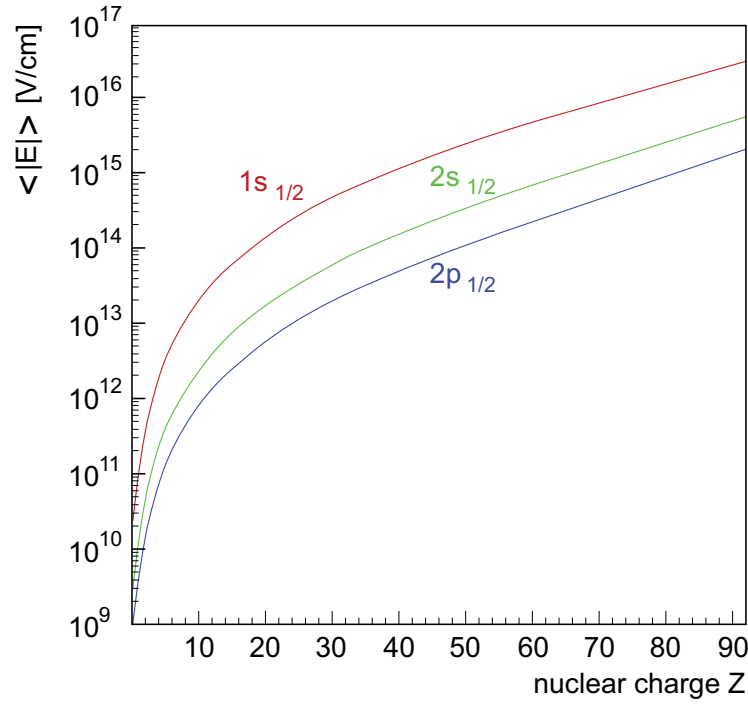


Figure 1.2: Electrical field strength in low-lying states of hydrogen-like ions as described in [Bei00].

In light systems the uncertainty of experiments is comparable to the QED calculations. Van Dyck and Dehmelt have measured g with a relative accuracy of $4.3 \cdot 10^{-12}$ [Dyc87]. This result was surpassed in 2006 by Gabrielse and collaborators, who measured g to $7.6 \cdot 10^{-13}$ [Odo06]. From this measurement α was determined with an accuracy of $7 \cdot 10^{-10}$ [Gab06]. Very recently the result for $g/2$ was improved to a relative uncertainty of $2.8 \cdot 10^{-13}$, which is 2.7 times smaller than the previous value. α is known with an accuracy of $3.7 \cdot 10^{-10}$ [Han08]. Trusting the QED calculations and using the experimental values of g from measurements of the bound electron in $^{12}\text{C}^{5+}$ and $^{16}\text{O}^{7+}$, the electron mass is determined to a relative accuracy of $7.3 \cdot 10^{-10}$ [Bei02, Bei03].

To explore the boundaries of the non-perturbative QED calculations for the strong-field regime, experiments with heavy, highly charged ions are the perfect approach. The unique facility to conduct these experiments is the GSI accelerator complex. A combination of linear acceleration and prestripping with synchrotron acceleration and in-flight stripping on a solid target with high ion beam energy produces intense relativistic beams of heavy, highly charged (up to bare uranium) ions [Fra87]. The aim of ultimate accuracy is reached by decelerating the highly charged ions and therefore eliminating the uncertainty coming from the Doppler-shift.

In 1990, the late Helmut Poth organised a workshop at GSI, which was

dedicated to the deceleration and low-energy storage of highly charged ions. This workshop was followed by the development of the carbon g -factor trap in Mainz, where the g -factor of the bound electron in $^{12}\text{C}^{5+}$ was determined with a relative accuracy in the order of 10^{-10} [Häf00]. In 1998 the first proposal for HITRAP (Highly charged Ion TRAP) was submitted, but it took until 2006, when the construction of HITRAP was started.

The HITRAP project uses the whole accelerator facility of GSI. The ions are fully stripped after acceleration in the SchwerIonenSynchrotron (SIS - Heavy Ion Synchrotron). Then a first deceleration step is undertaken in the ExperimentierSpeicherRing (ESR - Experimental Storage Ring). Here the beam is cooled by stochastic and electron cooling. After the ESR the actual HITRAP facility starts. It consists of two linear decelerators, an IH-linac and a radio-frequency quadrupole, and the Cooler Trap. In this multi-ring Penning trap a large sample of heavy, highly charged ions will be cooled to 4 K and then sent to the various experiments. Later on HITRAP will become part of FLAIR (Facility for Low-energy Antiproton and Ion Research) and SPRAC (Stored Particles Atomic Physics Research Collaboration) at the new accelerator facility built on the GSI site, FAIR (Facility for Antiproton and Ion Research).

The crucial part of the HITRAP facility is the Cooler Trap. Here the ion bunch will be cooled down to 10 eV by electron cooling or even further to the sub-meV range by resistive cooling, depending on the requirements of the experiments. Extensive studies on the cooling of an ion bunch of 10^5 highly charged ions in a 6 T Penning trap have been undertaken in the design phase and to further understand the cooling processes [Mae08]. The focus of the here presented work was the design and the set-up of the detection/cooling electronics for the resistive cooling, as well as the implementation of a timing device for the trap.

Chapter 2 gives an overview on the SHIPTRAP and the HITRAP facilities and their role within the GSI accelerator complex, with detailed description of the single components of each facility. The following chapter 3 gives a short overview on the basic principles of Penning traps, Fourier transform - ion cyclotron resonances and resistive cooling before describing the developed detection and cooling electronics in detail. Chapter 4 describes the implementation of a field programmable gate array as a pattern generator within the existing control system for HITRAP. In chapter 5 the mass measurements conducted at SHIPTRAP in the region of $A = 96$ and the statistical analysis on the detectability of a low lying isomeric state are presented and discussed. The following, last chapter concludes the results obtained in this work and gives an outlook on the final commissioning of the HITRAP facility and further investigations at SHIPTRAP.

Chapter 2

HITRAP and SHIPTRAP within GSI

In this chapter both experimental facilities - HITRAP and SHIPTRAP - are discussed within the framework of the GSI accelerator complex. After a short introduction to the basic principles of Penning traps, the ion production and delivery to the experiments is discussed. Then, the various components of each facility will be discussed in detail. Since HITRAP is not yet fully operational, all of its sections will be presented in their present status.

2.1 Penning trap basics

A Penning trap is a device which enables three-dimensional confinement of a charged particle. This is realized using the superposition of an electrostatic and a magnetic field, since the Laplace equation $\nabla^2 V = -\nabla \cdot \vec{E} = 0$ restricts electrostatic confinement to two dimensions (also known as Earnshaw's theorem [Ear42]). A simple realization of such a trap is a cylindrical electrode in the center with a plate (or a cylindrical) electrode at each end, that is immersed in the axial magnetic field of a solenoid [Mal75]. A voltage between the outer electrodes (endcaps) and the central electrode provides trapping in the axial direction, whereas the radial confinement is done by the Lorentz force

$$\vec{F}_L = q\vec{v} \times \vec{B}. \quad (2.1)$$

which forces the particles to gyrate around the B-field lines. Cylindrical Penning traps are commonly used by plasma physicists to confine large numbers of particles (see fig. 2.1)

For high-precision experiments a more sophisticated trap design is necessary to gain better control on the motions of the trapped particle. The underlying theory of such a trap has been devised by J. R. Pierce [Pie49], whereas Nobel laureate H. G. Dehmelt has first built a precision trap and conducted first experiments on charged particles in it [Deh58, Deh67, Deh68, Deh69]. In this trap design the central electrode as well as the endcaps have a hyperbolic

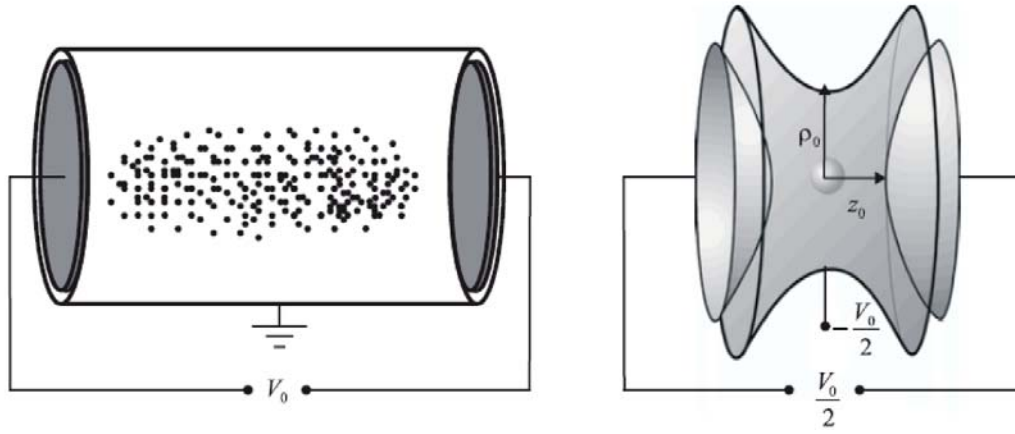


Figure 2.1: Penning trap schematics

On the left the Penning-Malmberg trap is shown. This is used widely in plasma physics to confine large numbers of particles. On the right the hyperbolic Penning trap is shown. This is used for high-precision experiments on single particles in atomic physics. Picture courtesy of G. Maero [Mae08].

shape as shown in fig. 2.1 on the right. This shape makes it easier to achieve an exact quadrupolar electrostatic potential in the trapping region, which allows for an analytical treatment of the trapped particles dynamics.

It has been shown, that a trapped particle in a quadrupolar potential follows three well-defined eigenmotions [Bro86]: the axial motion, the reduced cyclotron and the magnetron motion (see fig. 2.2). The axial motion is defined by the electrostatic potential V_0 and the trap size $d_o = \frac{1}{2}\sqrt{z_o^2 + \rho_o^2/2}$ as well as the mass-to-charge ratio:

$$\omega_z = \sqrt{\frac{qV_o}{md_o^2}} \quad (2.2)$$

The frequency of the axial motion is independent of the particles energy, which enables the detection and resistive cooling via a circuit tuned to the particles oscillation frequency. The same detection principle, using a tuned circuit, is also applicable to the cyclotron motion (one of the radial motions of the particle). In a magnetic field, the ion follows a circular orbit in the orthogonal plane. The frequency is given by:

$$\omega_c = \frac{qB}{m}; \quad (2.3)$$

The simultaneous presence of an electric field now adds an $\vec{E} \times \vec{B}$ circular drift (the magnetron motion) to the radial motion. This splits the pure cyclotron motion in two superimposed motions: the reduced cyclotron motion with a slightly lower frequency ω_+ than the pure cyclotron frequency and the slow magnetron drift motion around the symmetry axis with the frequency ω_- . This results in an epicyclic motion in the radial plane (fig. 2.2, left). The

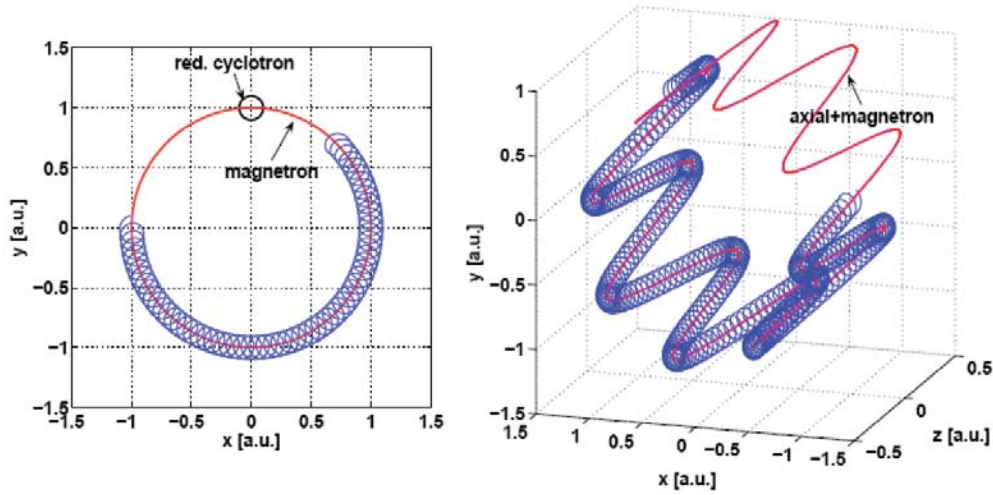


Figure 2.2: Ion motions in a Penning trap

The motions in the radial plane are shown on the left, whereas on the right side all three motions in three dimensions are seen. Picture courtesy of G. Maero [Mae08].

frequencies are given by:

$$\omega_{\pm} = \frac{\omega_c}{2} \pm \sqrt{\frac{\omega_c^2}{4} - \frac{\omega_z^2}{2}}, \quad (2.4)$$

Usually the fields are chosen in a way, that $\omega_c \approx \omega_+ \gg \omega_z \gg \omega_-$.

The three eigenfrequencies are connected by the relations: $\omega_c = \omega_+ + \omega_-$ (in an ideal trap) and $\omega_c^2 = \omega_z^2 + \omega_+^2 + \omega_-^2$ (invariance theorem [Bro86, Gab08]). These can be exploited for the manipulation of the particles in the trap. Exciting the sum of two eigenfrequencies, for example, results in a periodic energy transfer from one motion to the other. This is used at SHIPTRAP for cleaning the ion sample, preparing the single ion for measurement and for the mass measurement itself (see chapter 2.3.4). At HITRAP we can use this energy transfer to cool all degrees of freedom while acting on just one mode - in our case the axial frequency.

At SHIPTRAP and HITRAP a cylindrical Penning trap design is used. The advantages of the cylindrical design are obvious: the injection and ejection is much simpler due to open endcaps and the effective trapping volume is larger. A disadvantage of the cylindrical design is the higher field anharmonicity. This can be reduced using the *orthogonalized anharmonicity compensation* [Gab84]. The central quadrupole potential $V \propto z^2 - r^2$ can be expanded in Legendre polynomials to

$$V = \frac{1}{2}V_0 \sum_{k \text{ even}=0}^{\infty} C_k \left(\frac{r}{d_0}\right)^k P_k(\cos\theta) \quad (2.5)$$

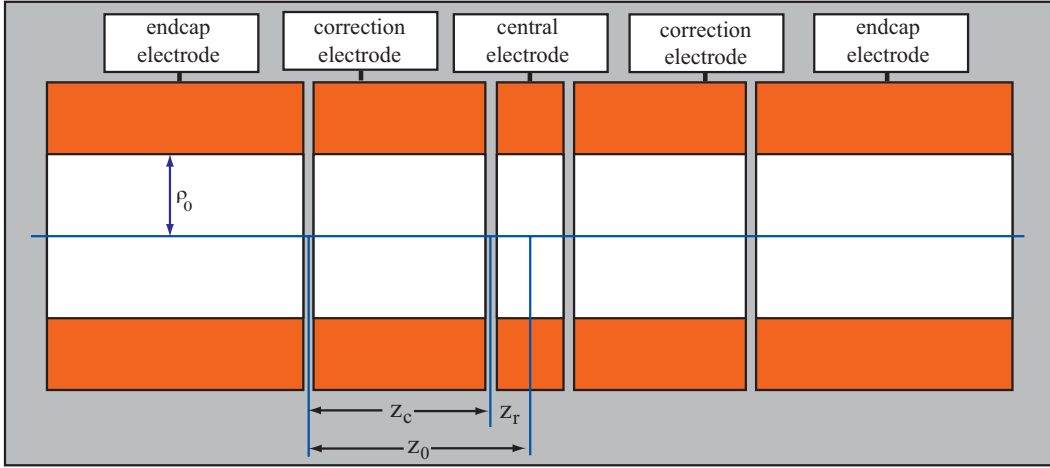


Figure 2.3: Compensated cylindrical Penning trap.

The trapping potential is defined by the voltages applied to the endcaps and the central ring. The voltage applied to the correction electrodes is optimized to improve the harmonic field region.

with V_0 being the trapping potential and the characteristic trap size d . To meet the request for harmonicity C_k should be zero for all $k > 2$. At least C_4 , the first anharmonic contribution, should be zero.

Introducing a correction electrode at either side of the central electrode (see figure 2.3), the harmonic region can be extended and C_4 vanishes by choosing the right correction voltage. But this correction voltage also alters the other coefficients C_k . It has been shown, that by choosing the proper ratio of ρ/z_0 and z_c/z_0 the unwanted effect on C_2 can be avoided - this is the *orthogonalization*. In addition, choosing $z_c/z_0 = 0.835$, C_6 also vanishes [Gab89].

2.2 Ion production at GSI

2.2.1 Production of highly charged ions

There are two methods to produce highly charged ions. Either multiple ionization by collisions with energetic electrons or in-flight stripping. The first method is employed in electron cyclotron resonance (ECR) sources and in electron beam ion sources and traps (EBIS/EBIT) [McD02]. Here the energy used for the ionization process comes from the electrons, therefore, the extracted ions have rather low energies. But generally the charge states available for heavy nuclides from such a source are limited to medium charged ions in case of the ECR method and few electron ions for EBIS/EBIT devices. To reach bare uranium electron energies of several hundred keV are necessary. Only in the SuperEBIT [Mar94] a few U^{92+} were observed together with large amounts of hydrogen- and helium-like uranium.

At the GSI accelerator complex highly charged ions are produced via the

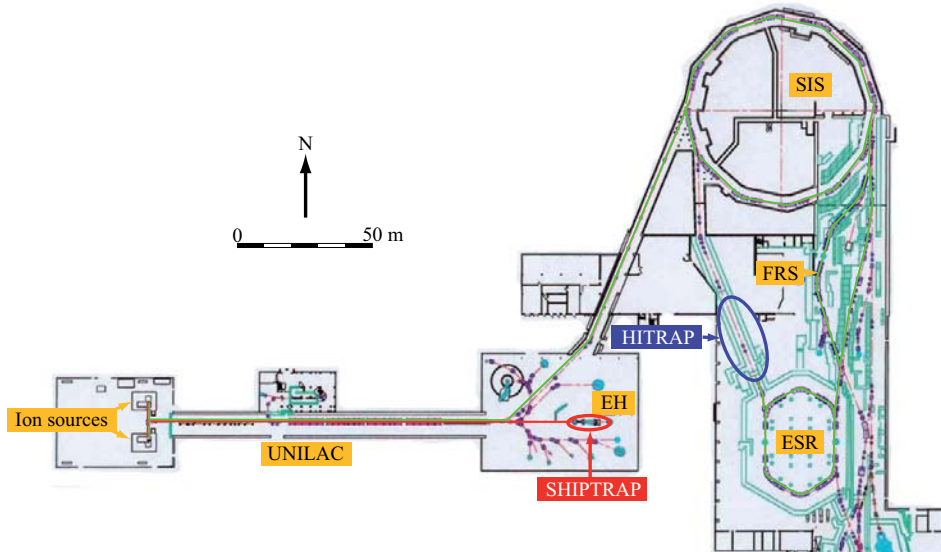


Figure 2.4: Overview of the GSI accelerator complex.

The ions are first accelerated by the UNILAC linear accelerator, where they can also be stripped to medium charge states. SHIPTRAP (red) is situated in the low energy experimental hall after the UNILAC. For HITRAP the beam is further accelerated in the SIS synchrotron and subsequently stripped to bare or few electron ions in the stripper target. The FRagment Separator (FRS) can provide selected radioactive ions produced by nuclear reactions. In the ESR the beam is cooled and decelerated. Then it is extracted to HITRAP (blue) in the reinjection channel. The beamline to SHIPTRAP is marked in red, the beamline to HITRAP in green.

in-flight stripping technique [Kie89]. Here a high-energy ion beam impinges on a gas or a solid target. The shell electrons of the projectiles are removed by collisions with the target atoms. The yield of highly charged ions (HCI) depends on the target material and thickness, ion species and beam energy [Shi82]. For a 400 MeV/u beam of U^{73+} on a copper foil with $40 \mu\text{g}/\text{cm}^2$ a high yield of bare uranium can be achieved [Dah04].

There are three stripper targets at the GSI accelerator complex: the gas stripper target in the UNILAC provides medium charge states up to U^{28+} with a stripping efficiency of about 13%; the foil stripper target in the transfer section to the Heavy Ion Synchrotron (SIS) enhances the charge state up to U^{73+} , which is needed to reach high energies through the acceleration in the SIS. This stripper target has an efficiency of 17% [Bar08]. The last stripper target is another foil after the Heavy Ion Synchrotron, which finally produces charge states up to bare uranium.

2.2.2 The accelerator complex at GSI

In Fig. 2.4 the accelerator complex at GSI is sketched. The complex consists of three main parts: UNILAC, SIS and ESR (Experimental Storage Ring). After the injection from the ion sources, the beam is accelerated by the UNILAC up to 11.4 MeV/u. The gas stripper in the UNILAC beamline provides medium charge states. For the SHIPTRAP primary beam from the UNILAC lower energies and charge states are sufficient. Crucial is here a high beam intensity, so that usually the charge state at which the ion source has the highest yield is used. The energy is tuned to enable the ions to overcome the Coulomb barrier of the target atoms - which is about 4 to 5 MeV/u. A closer discussion can be found in chapter 2.3.

Before injection into the SIS, the ions are further stripped in a stripper foil up to U^{73+} . This enhances the maximum reachable energy in the acceleration process in the Heavy Ion Synchrotron, up to 1 GeV/u. This beam can then be sent through another stripper foil target, so that highly charged ions (HCI) - i.e. bare, hydrogen-like, helium-like or lithium-like ions - are created. After that, the beam can either be sent directly to the Experimental Storage Ring (ESR) or can be used beforehand to produce radioactive ions by fragmentation or Coulomb dissociation. From these secondary ions the species of interest is selected by the FRagment Separator (FRS). In the ESR stochastic as well as electron cooling are applied to reduce the emittance. Cooling in combination with the possibility of deceleration by synchronous down ramping of the dipole magnets and the applied radio-frequency allows for high-precision experiments at selected energies.

2.3 The SHIPTRAP facility

The Penning trap mass spectrometer SHIPTRAP has been designed for high-precision experiments on radioactive and stable ions produced at the Separator for Heavy Ion Products (SHIP). The ions are stopped in a buffer gas cell, the first stage of the SHIPTRAP facility. Then they are extracted to a radio-frequency quadrupole (RFQ) structure, where they are cooled by helium buffer gas and accumulated. The bunched ions are then sent to a double Penning trap structure immersed in a superconducting magnet, where they are mass separated and prepared. SHIPTRAP is situated in the low energy experimental hall after the UNILAC at GSI, directly behind the SHIP velocity filter. In this section the major elements of SHIPTRAP will be described in some detail.

2.3.1 The velocity filter SHIP

One of the first experiments at GSI was the Separator for Heavy Ion Products (SHIP) [Mün79], at which the superheavy elements from 106 to 111 [Hof00]

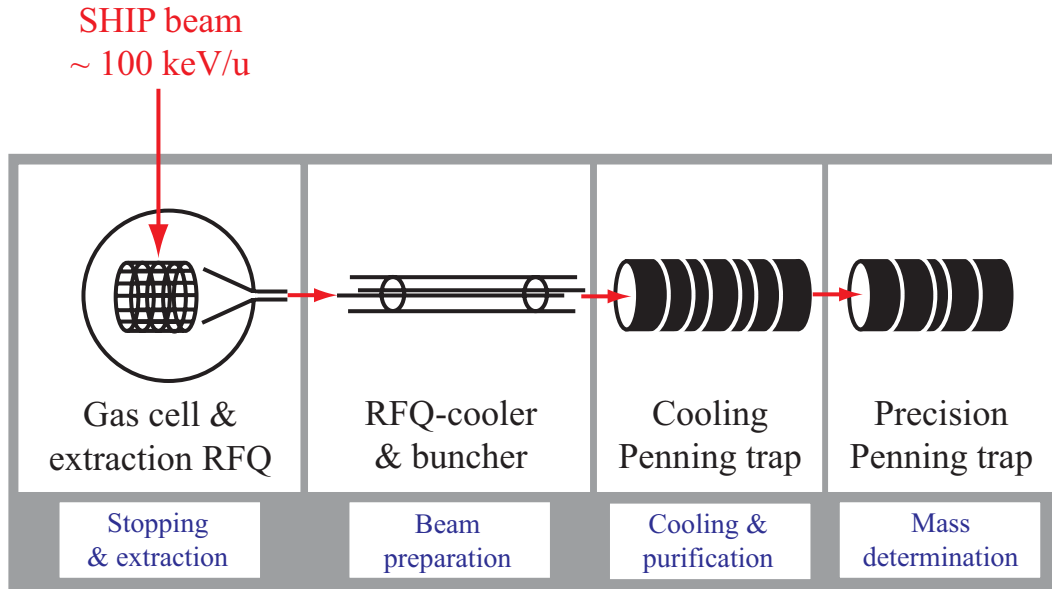


Figure 2.5: Schematic of the SHIPTRAP facility.

The ions coming from the SHIP velocity filter are stopped in the gas cell. Then they are extracted to the RFQ buncher, for accumulation and cooling. In the Penning traps RF-centering and mass-measurements take place.

were discovered, bringing world-wide renown. An overview on the SHIP facility is found in fig. 2.6. The heavy and superheavy elements are produced by fusion-evaporation reactions, triggered by a high-intensity (particle- μA) primary beam impinging on a thin target foil (metal or covered carbon). The beam energy has to be tuned carefully, so that the Coulomb barrier of the target nucleus is just slightly overcome. Too low energies will not lead to fusion. Too high energies lead to highly excited compound nuclei, which will almost immediately decay by fission. But with the right energy chosen, the compound nucleus cools its rather small excitation energy by evaporation of few nucleons or α -particles.

From the target wheel a mixed beam of two components enters the SHIP separator: the remainder of the primary beam and the fusion reaction products. The latter have typical energies of a few 100 keV/u due to recoil momentum transfer, which distinguishes them kinematically well from the primary beam ions. Therefore the SHIP separator is a double Wien filter, in which the deflection of the ions depends on their velocity and not on their mass-over-charge ratio m/q . This is realized by a special combination of electrostatic and magnetic deflectors, whose homogeneous fields are perpendicular to each other and the beam axis. By setting the electric and magnetic field strength the transmitted velocity class is chosen.

The primary beam suppression in the filter is determined by the velocity

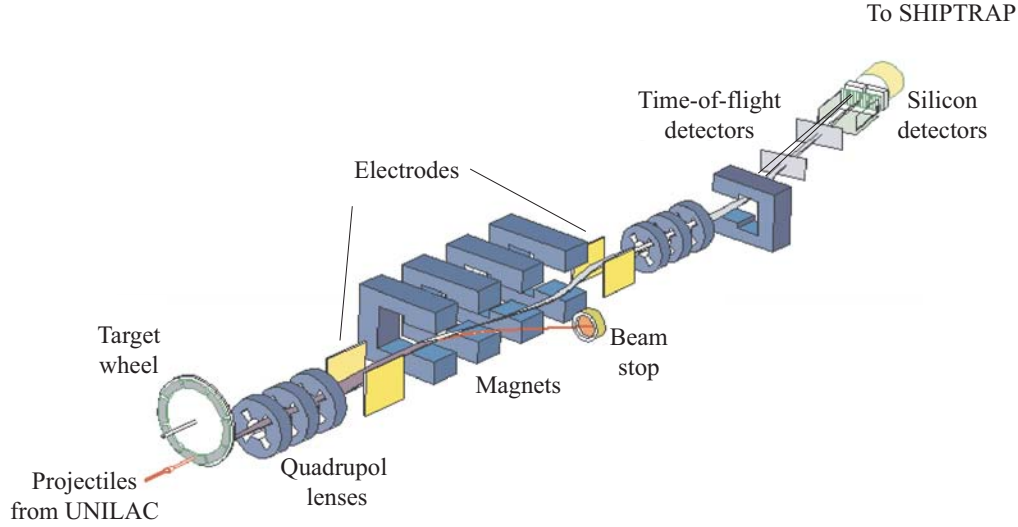


Figure 2.6: Overview of the SHIP velocity filter.

The fusion reactions take place in the targets mounted on a wheel. The following Wien filter separates the fusion reaction products from the primary beam. The products are identified by a time-of-flight measurement combined with a decay chain detection in the Si detector. For online measurements at SHIPTRAP the Si detector is removed. The overall length of SHIP is about 11 m [Neu06].

ratio between primary beam v_p and reaction products v_c

$$\frac{v_c}{v_p} = \frac{m_p}{m_c} \quad (2.6)$$

with m_p being the mass of the projectile and m_c the mass of the compound nucleus, i.e. the sum of projectile and target nucleus. For a given compound nucleus equation 2.6 shows, that the best suppression is reached by impinging a light projectile on a heavy target. Typical suppression rates are 10^7 to 10^{10} [Mün79].

The transmitted beam is focused and steered onto position-sensitive silicon detectors by quadrupole triplet lenses and an electric dipole magnet (see fig. 2.6). The superheavy elements implanted in the detector are identified by their α -decay chains. For online SHIPTRAP experiments this detector is replaced by a beamline leading to the gas cell.

The energy spread of the fusion reaction products ranges from 10% to 30%, since the energy of a single particle is mainly determined by the target foil thickness. Depending on the place of production within the foil, the energy loss on the remaining path through the foil varies.

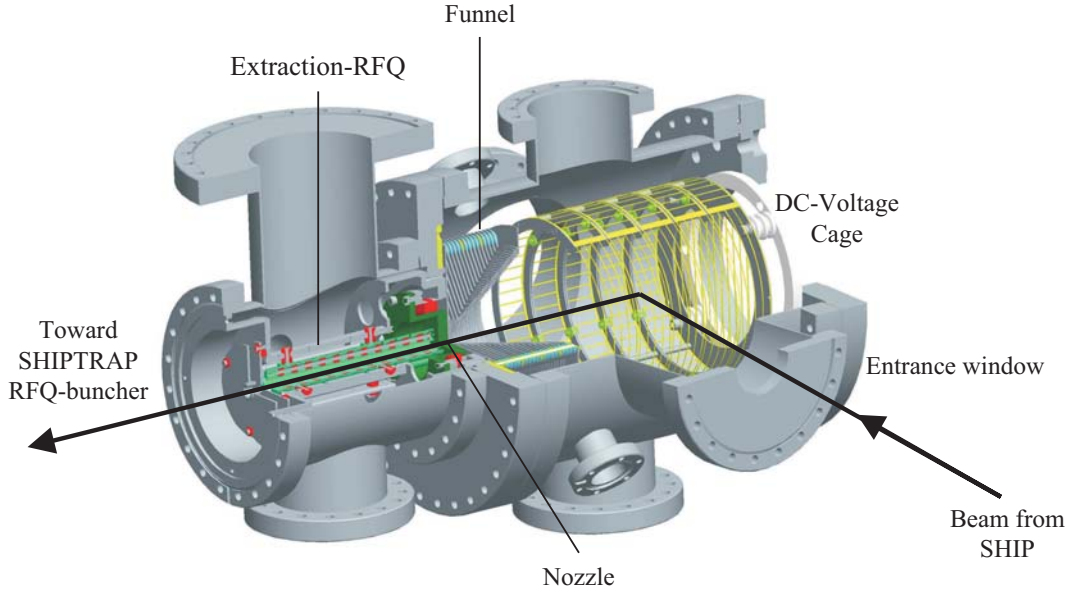


Figure 2.7: The SHIPTRAP gas cell.

The technical drawing shows the gas cell and the adjacent extraction RFQ. The cell is filled with helium as buffer gas, which stops the ions coming from SHIP entering the cell through a window foil. The electrostatic field from the cage and the RF field from the funnel guide the ions to the nozzle region, where they are dragged out to the extraction RFQ by a supersonic gas jet. The RFQ not only guides the ions but also provides differential pumping [Neu06].

The total efficiency of SHIP is given by the ratio of ions counted at the detector to produced ions. It depends on excitation energy and projectile mass. A higher excitation energy means higher angular straggling due to more evaporated particles [Mün79], which reduces the number of ions at the detector position, due to SHIP's fixed acceptance. The same argument holds for low mass projectiles, which also results in a higher straggling and therefore lower efficiency [Fau79]. A total efficiency of 14(1)% was determined using the reaction $^{150}\text{Nd}(^{40}\text{Ar}, 6n)^{184}\text{Pt}$ [Mün79]. Nevertheless light projectile beams of argon, calcium, chromium and nickel are usually favorable, since they give a better primary beam suppression and the efficiency loss can be compensated by higher beam intensity.

2.3.2 The SHIPTRAP gas cell

The SHIP beam has a rather high energy, compared to other online Penning trap experiments, as ISOLTRAP [Muk08] and JYFLTRAP [Kol04]. Accepting this high energy beam is a quite challenging task. Further so, due to its big energy spread of 10% to 30% at 50 - 100 MeV and great transversal width of $50 \times 30 \text{ mm}^2$. To accept this beam a dedicated gas cell was constructed [Neu06].

Fig. 2.7 shows a technical drawing of the SHIPTRAP gas cell. The gas cell is filled with helium buffer gas at a typical pressure of around 50 mbar. Ions coming from SHIP enter the cell through a thin (few μm) metal foil window, where they already loose the major part of their energy and are finally stopped by collisions with the gas. The stopping efficiency depends on the absolute beam energy and its spread as well as the window thickness and the gas pressure. Therefore the latter properties have to be chosen and optimized individually for each new experiment. A detailed description can be found in [Rau06].

In the stopping process every ion coming from SHIP produces at least 10^5 $\text{He}^+ + \text{e}^-$ pairs [Huy02]. Since the ions of interest can have charge exchange by collisions with the buffer gas atoms, they have to be dragged out of the stopping volume fast. Therefore a five-fold segmented DC cage within the cell creates a field gradient (between 100 V/m and 300 V/m) towards the funnel electrode (see fig. 2.7). The funnel consists of 40 concentric electrodes, which create a DC slope towards the extraction nozzle with a diameter of 0.6 mm. Additionally, a radio-frequency (RF) field applied at the funnel electrodes prevents the ions from hitting the electrodes. At the end of the funnel, the ions are dragged through the nozzle by the gas flow into the extraction radio-frequency quadrupole (RFQ). Therefore, the potential difference between the last funnel electrode and the nozzle electrode has to be tuned such, that the ions' drift velocity is matched to the velocity of the helium gas diffusing from the gas cell. The extraction RFQ consists of four rods, which are longitudinally 12 times segmented. It has an overall length of 18 cm. In the extraction RFQ the RF field focuses the ions on the beam axis while a DC gradient transports them to the RFQ buncher. The extraction RFQ also acts as a differential pumping stage, where the helium flowing from the gas cell is pumped away. The typical extraction time of about 10 ms (determined by the drift time depending on the gas pressure and the DC-gradient applied) limits the measurable species. If the half-life is shorter than the extraction time, most of the ions decay within the gas cell.

The total efficiency of the gas cell is defined by the ratio of extracted ions to ions entering through the window foil. It can be described by the product of the stopping efficiency and the extraction efficiency

$$\epsilon_{\text{GasCell}} = \epsilon_{\text{stop}} \times \epsilon_{\text{extr}} \quad (2.7)$$

While ϵ_{stop} could be only deduced from simulations to about 30% yet, ϵ_{extr} was studied thoroughly using a ^{223}Ra ion source inside of the gas cell to be typically between 10% and 20% [Eli07b]. The overall efficiency of the gas cell was measured online at the Maier-Leibnitz Laboratory (MLL) in Garching and at GSI to be 5-8% maximum [Neu06].

The efficiency is highly influenced by contaminants of the buffer gas, coming from the gas itself and from the residual gas pressure in the cell. These con-

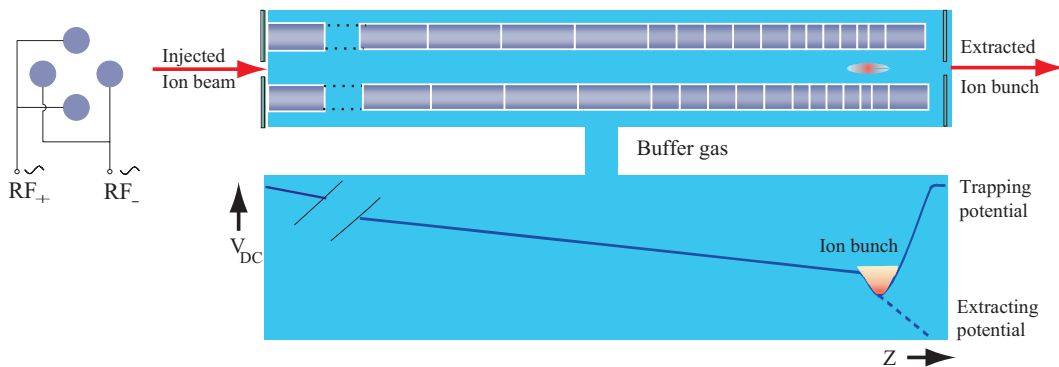


Figure 2.8: Schematic of the SHIPTRAP RFQ buncher.

A RF quadrupole field guides the ions through this structure. The RF feed is shown at the left. Ion cooling is done by buffer gas. The segmentation of the electrodes allows for trapping and accumulation of the ions. The structure has a length of 1 m and an inner diameter of 7.8 mm [Rod03].

taminants lead to charge exchange reactions and molecule formation, thereby neutralizing the ions of interest. This effect can be drastically reduced by good vacuum conditions. These are achieved by using stainless steel and Al_2O_3 as well as oil-free pumps. Furthermore, the cell is baked for one to three days at about 150°C . This results in a residual gas pressure below $1 \cdot 10^{-9}$ mbar. Impurities from the helium itself are minimized by using purity grade 6.0 helium (i.e. 99.9999% He) and by guiding the helium line through a liquid nitrogen bath, freezing remaining contaminants.

2.3.3 The RFQ buncher and transfer section

From the quasi-continuous beam coming from the gas cell, the RFQ buncher prepares a bunched and cooled beam for optimized trapping. A schematic of the buncher is shown in fig. 2.8. Its four rod structure is segmented in 29 parts to enable the creation of a DC potential well. The radio-frequency applied to the rods creates a pseudopotential well, confining the ions radially. Helium buffer gas (about $5 \cdot 10^{-3}$ mbar) cools the radial motion. The loss of longitudinal energy helps trapping in the DC potential well. Typical accumulation times are about 1 s. Lowering the potential of the last electrode gives a time-defined pulse in the order of 200 ns [Wer08].

The buncher can also be operated in a RF-only mode (without quadrupolar DC-field) as a high-pass mass filter, with a typical resolving power of less than 50. This way, the amount of low-mass contaminants like helium, water and nitrogen stemming from charge exchange processes in the gas cell is reduced. Medium-mass contaminants can be cleaned away by dipole excitation at the potential minimum. The transmission efficiency of the buncher is nearly 100% without and about 50% with bunching [Rod03].

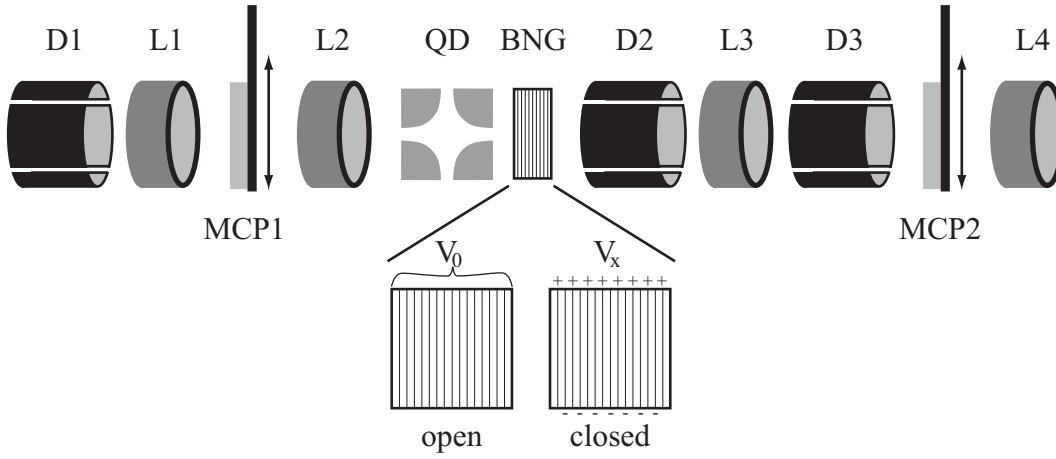


Figure 2.9: Schematic of the SHIPTRAP transfer section.

The beam is focused through the small aperture of the quadrupole deflector (QD) by two lenses (L1 and L2) and one deflector (D1). The Bradbury-Nielsen gate (BNG) is situated direct behind the quadrupole deflector. A schematic of the open and closed voltage is shown (V_0 is the common transfer voltage). The lenses L3 and L4 as well as the deflectors D2 and D3 are used for the efficient injection of the ions in the trap. For optimizing the transfer efficiency, two multi-channel plate (MCP) detectors can be introduced.

The transfer section guides the ions from the buncher to the Penning traps. A schematic is shown in figure 2.9. The section consists mainly of three electrostatic deflectors and four Einzel-lenses to steer and focus the ion bunch into the superconducting magnet. Furthermore, there is a quadrupole deflector, which allows for offline ion sources or diagnostic tools perpendicular to the beam line. Behind the quadrupole deflector a Bradbury-Nielsen gate [Bra36] was installed in August 2008. It consists of thin wires on a DC potential. If the gate is open, all wires are on drift potential. The gate is closed, when the wires have all the same potential difference to the drift potential, but with different sign at adjacent wires, which results in a deflection of the ions. The gate is switched on for a certain period of time, while the ions are in the transfer section. The efficiency of the gate was tested with a radioactive ion source, which emits ions of the masses 207, 211 and 219. Closing the gate for $1 \mu\text{s}$ at the right moment, the ions of the mass 211 pass loss-free, while the other masses are reduced by more than 80% [Wer08]. In the transfer line there are two multi-channel plate detectors (MCP), one after the gas cell, used for optimizing the gas cell and buncher settings, and one before the traps used to confirm the undisturbed transfer or measure the ions coming from the offline ion sources.

2.3.4 The SHIPTRAP Penning traps

The Penning trap system of SHIPTRAP consists of two cylindrical Penning traps: the purification trap and the measurement trap [Sik03]. The traps are

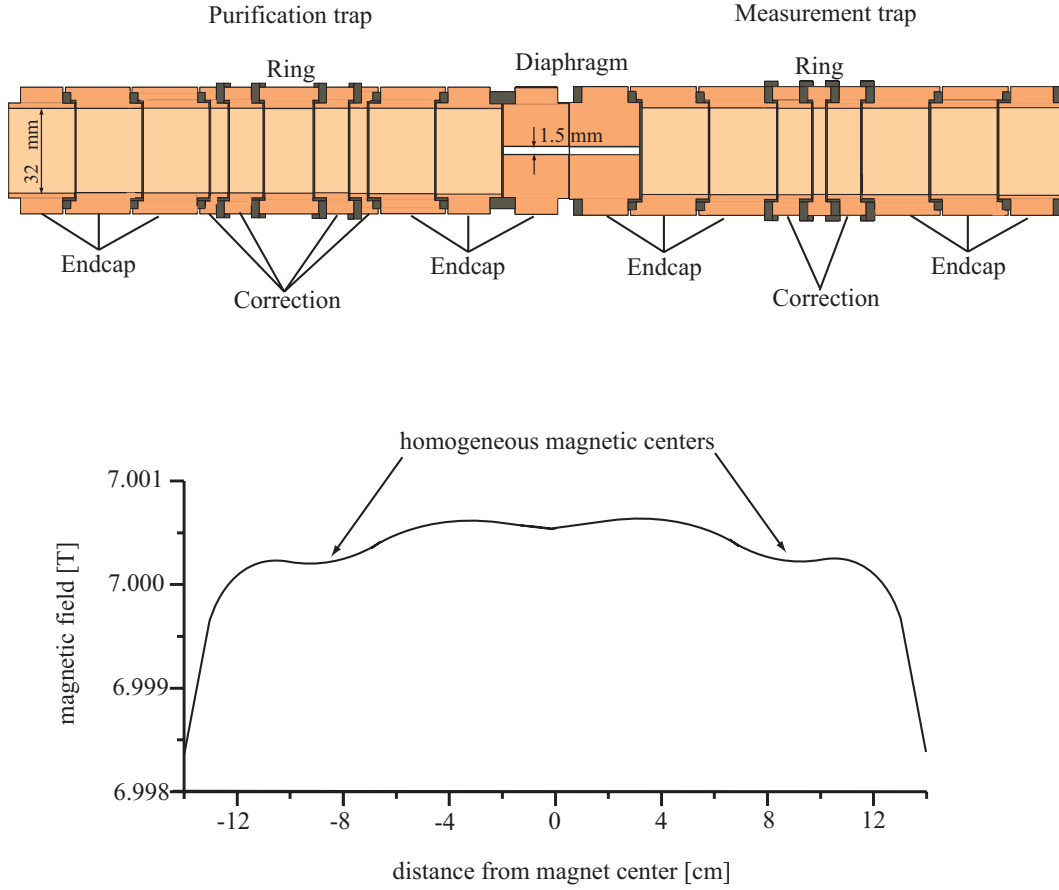


Figure 2.10: Schematic of the SHIPTRAP Penning traps.

In the upper part the two Penning traps are seen: on the left the 7-pole purification trap, on the right the 5-pole measurement trap. Both traps are separated by a diaphragm with a length of 52 mm and an inner diameter of 1.5 mm. The magnetic field distribution in the trap is shown in the lower part.

located in the two homogeneous regions of the same superconducting solenoid with a field strength of 7 T. The homogeneity of the magnetic field $\Delta B/B$ within 1 cm³ is 1 ppm in the purification trap and 0.14 ppm in the measurement trap (the traps are at $z = \pm 10$ cm from the center of the magnet) [Mag99]. The electrode set-up and the field distribution are shown in Fig. 2.10. The traps are connected via a diaphragm of 1.5 mm diameter and 52 mm length, which acts as pumping barrier against the buffer gas with a suppression factor of about 1000.

The purification trap is a 7-pole cylindrical Penning trap designed after the one at ISOLTRAP [Rai97]. It consists of an eightfold ring electrode with a pair of correction electrodes at each side and axially threefold segmented endcaps. The overall length is 212.5 mm and the characteristic trap dimension for the harmonic potential is $d = 26.8$ mm [Sik03]. The design leads to a high capture efficiency and high harmonicity at the center. From the captured ion bunch a

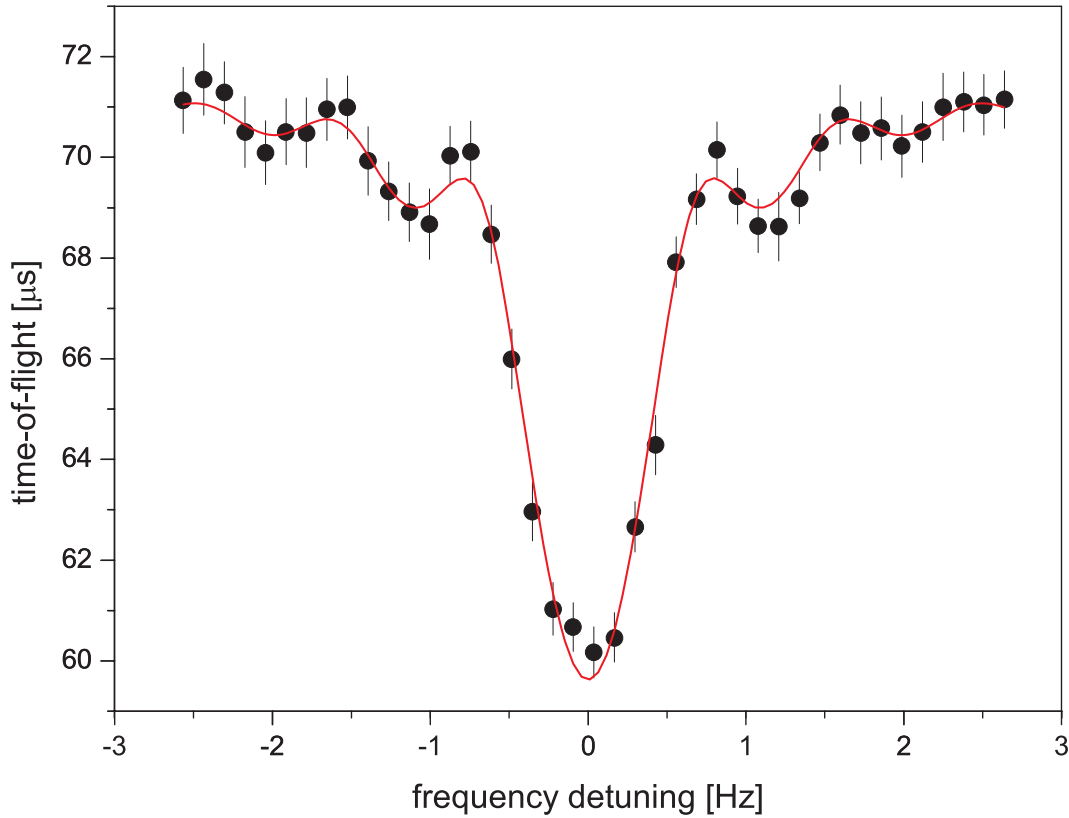


Figure 2.11: Time-of-flight resonance.

The time-of-flight versus the frequency detuning is shown. At the real cyclotron frequency the time-of-flight is lowest. The dots are data points, the red curve is a fit of the theoretical function.

single nuclide is prepared for mass measurement, applying the mass-selective buffer gas cleaning method [Sav91]. Hereby a buffer gas - mostly helium - at a pressure of about 10^{-6} mbar is introduced into the trap. The amplitudes of the axial and the modified cyclotron motion of the ions are reduced by collisions with the buffer gas, while the amplitude of the magnetron motion increases. This would lead to an ion loss within some 100 ms. To prevent the ion loss, a quadrupolar radio-frequency field with the true cyclotron frequency of the species of interest is applied. This leads to an energy transfer from the magnetron motion to the modified cyclotron motion. The latter is damped faster due to its higher velocity, so that the magnetron amplitude decreases and the ions accumulate at the trap center. This process is mass-selective, because the cyclotron frequency depends on the mass.

The actual cleaning is a two-step process. First the magnetron motion of all ions is excited by a dipolar RF field, increasing the magnetron orbit to 5-10 mm, barring the ions from passing through the diaphragm to the measurement trap. Then the cyclotron frequency of the species of interest is excited by a quadrupolar RF field, centering the ions with the corresponding mass-

to-charge ratio. Only these ions can pass to the measurement trap when the potential between both traps is lowered.

The measurement trap has a orthogonal 5-ring structure allowing for the precise mass measurements taking place here. Further technical details of the Penning trap system can be found in [Sik03].

The task of measuring the mass of the ion is reduced to the measurement of the cyclotron frequency by

$$\nu_c = \frac{1}{2\pi} \frac{q}{m} B \quad (2.8)$$

ν_c is obtained by the time-of-flight ion-cyclotron-resonance (TOF-ICR) method [Grä80]. Here the ions are first excited by a dipolar RF field at the magnetron frequency, which leads to an enhancement of their radial kinetic energy. This increases the contrast, but is limited by the fact, that too high amplitudes put the ions into more inhomogeneous field regions and out of the trap volume seen by the detector. Thereafter a quadrupolar RF field at the cyclotron frequency is applied, coupling the magnetron and the modified cyclotron motions. The so prepared ions are ejected from the trap, where they pass a strong magnetic field gradient on their way to the detector, which lies at a magnetic field of 50 mT. This leads to a conversion of radial into axial energy, since the interaction of the magnetic moment

$$\mu = \frac{E_r}{B} \quad (2.9)$$

(with E_r the radial energy of the ion) with the B field leads to an axially accelerating force $F = \nabla(\mu \cdot B)$. The time-of-flight is shortest at the real cyclotron frequency, since here the coupling between magnetron and cyclotron motion is strongest, i.e. the maximum radial energy is available. Therefore the cyclotron frequency is determined by measuring the time-of-flight of the ions depending on the excitation frequency. A typical time-of-flight resonance is shown in figure 2.11.

2.4 The HITRAP facility

2.4.1 Overview

The beam for HITRAP is produced by the GSI accelerator complex as described in section 2.2.2. In the Heavy Ion Synchrotron (SIS) the U^{73+} beam is accelerated to 400 MeV/u, before it is stripped to bare uranium in the stripper foil. About $5 \cdot 10^8$ particles are then delivered to the ESR, where the beam is decelerated to 4 MeV/u. Since the beam quality has been impaired by the stripping process, it is cooled stochastically for 5 to 20 s. Then the first deceleration step to 30 MeV/u is employed. This takes 3 to 10 s, with a loss of about 10%. After this, the beam is electron cooled and rebunched within 2 to

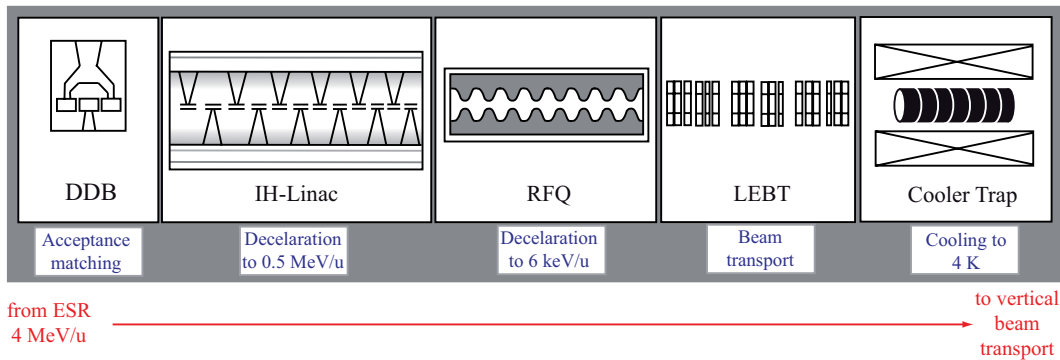


Figure 2.12: Schematic of the HITRAP facility.

All major elements of the HITRAP facility are shown. From left to right there is the Double Drift Buncher which matches the beam coming from the ESR onto the Interdigital H-type linac, the first deceleration stage. This is followed by the radio-frequency quadrupole, which decelerates the beam further, before it is transported to the Cooler Trap via the Low Energy Beam Transport section. In the Trap the beam is cooled and then extracted to the experiments on top of the reinjection channel using the Vertical Beamline.

6 s, to keep the longitudinal momentum spread and the transverse emittance of the beam low [Ste04]. Now the final deceleration phase down to 4 MeV/u takes place, which again takes 2 to 5 s. The final energy of 4 MeV/u was chosen for two reasons: The limitations in the following decelerator excluded higher energies, while at lower energies the losses get to high and the operation of the ESR at its minimum energy of 3 MeV/u is rather complicated [Kes06]. After the deceleration the ions are again electron cooled for 2 to 5 s and then ejected. With the reset of the magnets (3 s) the complete cycle time varies between 17 and 46 s.

After ejection from the ESR the ions enter the HITRAP facility in the reinjection channel, which formerly contained a beamline to reinject ions from the ESR to the SIS. The HITRAP facility itself consists of two decelerating devices, an electrostatic beam transport section, the Cooler Trap and a Vertical Low Energy Beamline to the dedicated experiments on top of the reinjection channel. A sketch is given in Fig. 2.12.

The energy limit for the in-flight capture of the ions in the Cooler Trap is about 6 keV/u. Details can be found in section 2.4.5. Since an efficient decelerating from 4 MeV/u down to 6 keV/u cannot be achieved by one compact structure, the task is distributed to two machines. First an Interdigital H-type linear decelerator (IH) [Dah04] slows the beam down to 0.5 MeV/u. The second deceleration step takes place in a radio-frequency Quadrupole (RFQ) [Hof06]. To fit the beam coming from the ESR into the acceptance of the IH, the decelerating stage is preceded by a Double-Drift-Buncher (DDB). Both, the IH-Linac and the RFQ, are designed to efficiently decelerate beams with a

Table 2.1: Calculated performance of the decelerator elements [Kes06a]. The entrance and exit energies and emittances as well as the transmission of all devices is given. The overall transmission is about 55%.

	DDB	IH	Rebuncher	RFQ & Debuncher
Entrance energy [MeV/u]	4	4	0.5	0.5
Exit energy [MeV/u]	4	0.5	0.5	0.006
Normalized $\varepsilon_{xx'(yy')}$ entrance [mm mrad]	0.2	0.21	0.3	0.34
Normalized $\varepsilon_{xx'(yy')}$ exit [mm mrad]	0.21	0.3	0.34	0.36
Transmission [%]	98	70	95	85

mass-over-charge ratio lower than three, but not to cool them. After the ions are slowed down to 6 keV/u, they enter the low-energy section of HITRAP, where they will be cooled down to 4K before being sent to the experiments. The low-energy section consists of the Low Energy Beam Transport (LEBT), the Cooler Trap and the Vertical Beamline. The LEBT is an electrostatic beam transport section, which connects the RFQ to the Cooler Trap. As its name states, the ions are cooled down to 4K in the Cooler Trap after they have been captured in flight. The cooling techniques employed here are electron and resistive cooling. At last, the cooled particles are sent to the experiments on top of the reinjection channel via the Vertical Beamline.

Since existing UNILAC devices were used to power the HITRAP RF devices, these work at the frequency of the UNILAC Alvarez structure, i.e. 108.408 MHz or higher harmonics of that.

2.4.2 The Double-Drift-Buncher and the IH-Linac

The 1 μ s macropulse coming from the ESR cannot be fed efficiently to the IH-Linac, since this has an acceptance of 10° to 15° from the 360° of the 9.2 ns period of the decelerating radio-frequency. Therefore the beam has to be bunched to fit the acceptance, which is done by the Double Drift Buncher (DDB), consisting of two RF cavities working at 108.408 MHz and 216.816 MHz, respectively. The 108 MHz cavity is a 4-gap buncher, the 216 MHz cavity a 2-gap buncher (see Fig. 2.13). Both cavities are driven by 2 kW RF generators. This solution has the same bunching efficiency as a multiharmonic buncher, while its operation is much easier [Pan01].

The DDB was installed at the HITRAP site in 2007 and was commissioned in the same year in two beamtimes with $^{64}\text{Ni}^{28+}$ and $^{20}\text{Ne}^{10+}$ beams, respectively. During these beamtimes the beam emittance was measured with

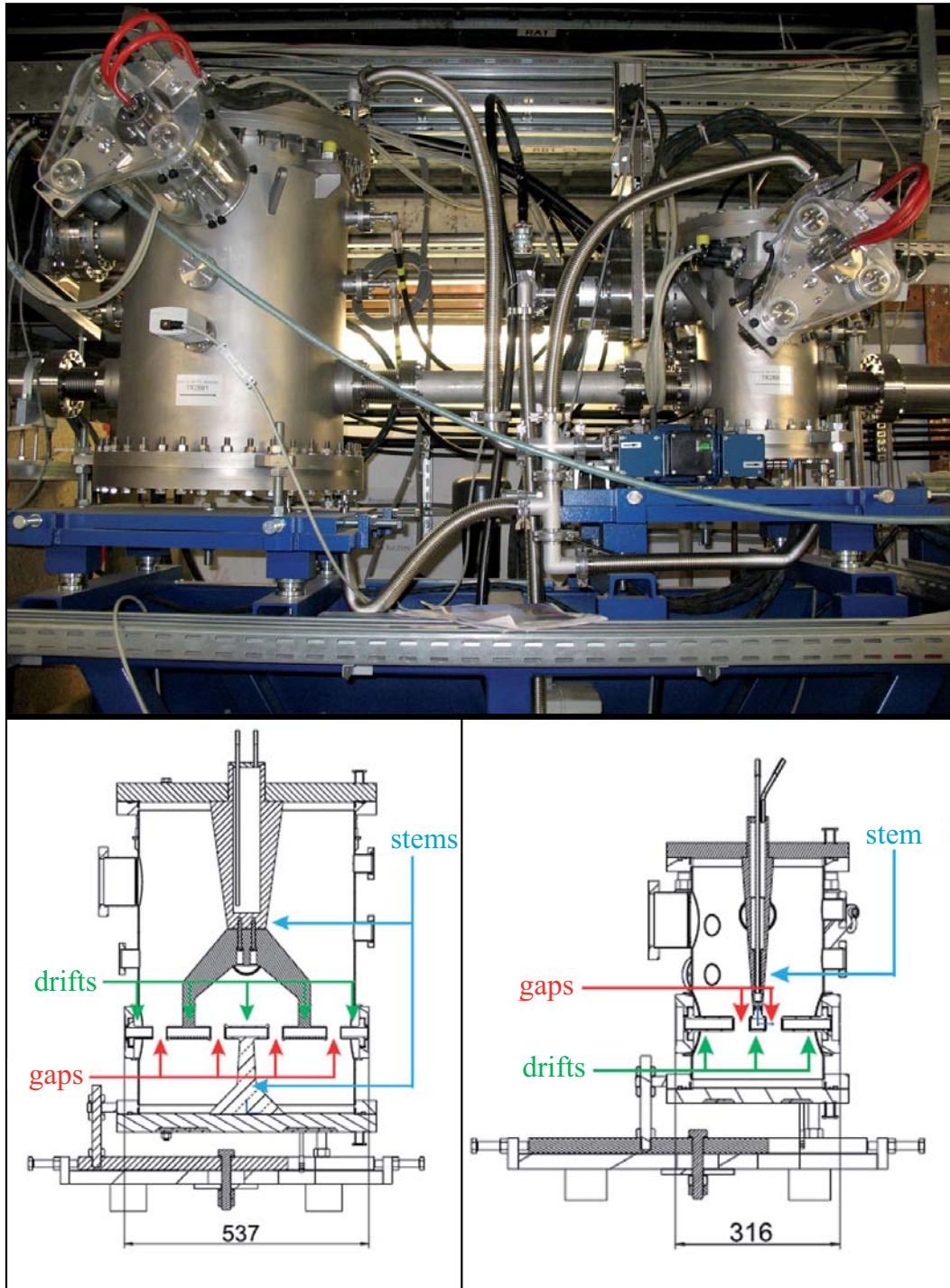


Figure 2.13: The Double Drift Buncher.

On top the DDB in the reinjection tunnel is shown. Below a cut in longitudinal direction through both cavities is shown. Drift tubes and stems are indicated. Left is the 108 MHz cavity (4-gap), while the 216 MHz 2-gap buncher is shown on the right side. All dimensions in mm. See [Dah06] for further details.

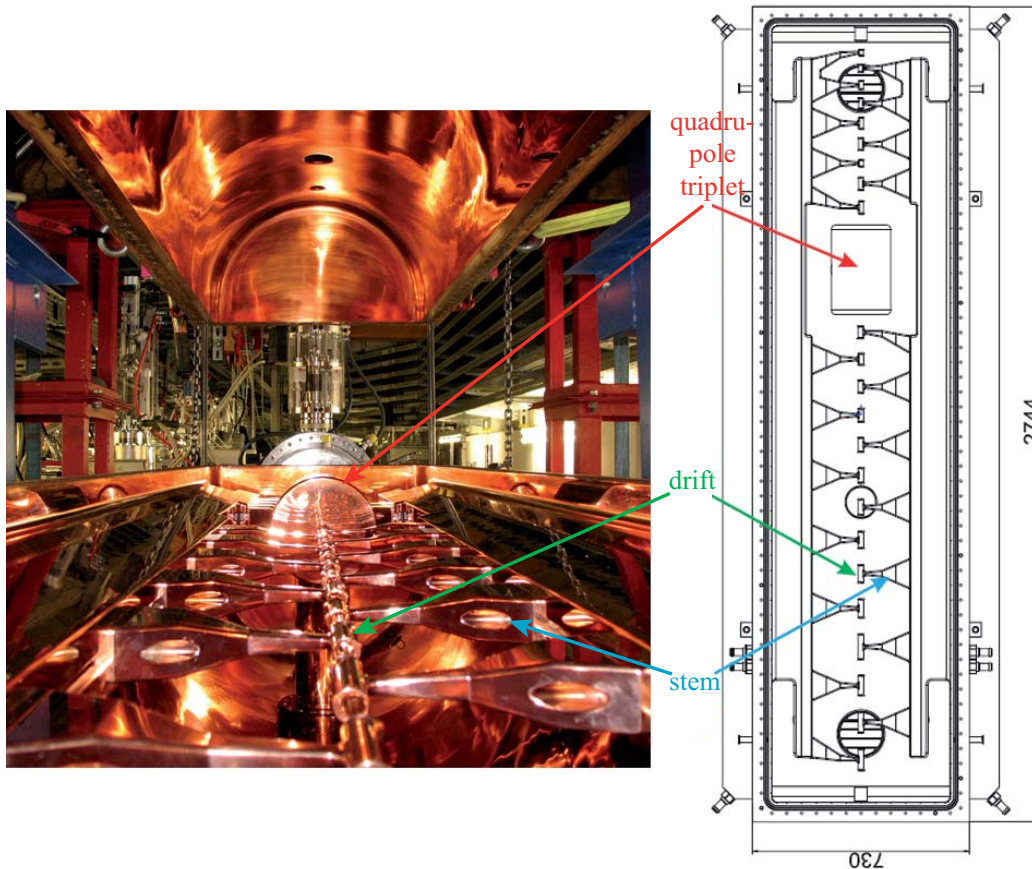


Figure 2.14: The IH-linac.

Shown is a photo and the technical drawing of the IH-linac. The linac was commissioned in 2008. The drawing shows the 25 drift tubes and the inner housing for the transverse focusing quadrupole triplet. All dimensions in mm. See [Dah06] for further details.

a single-shot emittance meter at the location of the entrance to the IH. The so measured values for the root mean square (rms) normalized emittance of $\varepsilon_{xx',n}^{rms} = 0.207$ mm mrad and $\varepsilon_{yy',n}^{rms} = 0.249$ mm mrad are comparable to the nominal values given in Table 2.1, which shows the expected performance and beam parameters for each part of the decelerator. The effective emittance is four times larger than the rms value, which is within the acceptance of the DDB but not of the IH. This enhanced emittance was due to problems in the ESR cooling cycle, which resulted in an uncooled beam. Nonetheless the beam transmission was measured to be 80%, which is near to the envisaged 98 %, and a well focused beam was seen at the entrance position of the IH. The cooling problems have been solved, so that in all other beamtimes a cooled beam was supplied by the ESR.

The IH-Linac decelerator is basically an electromagnetic accelerator operated in reverse direction. It consists of a 2.7 m long stainless steel tank with 25

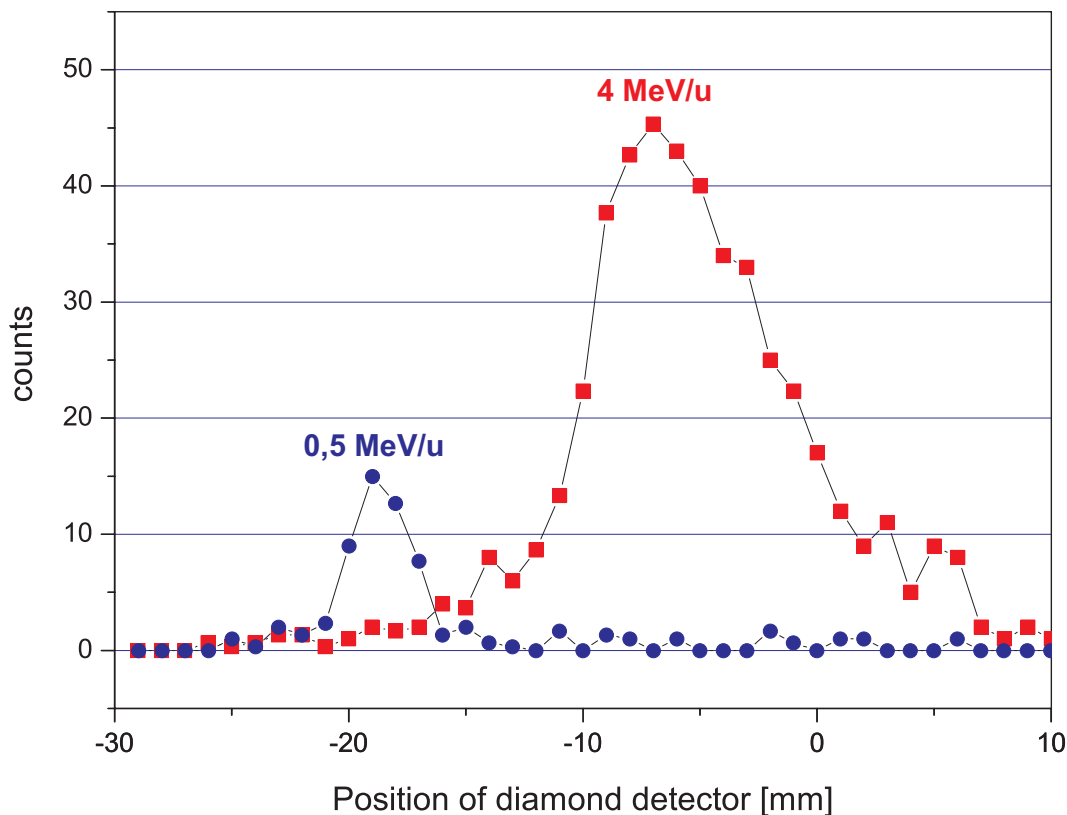


Figure 2.15: Decelerated beam after the IH-linac.

The beam profile versus the position of the diamond detector is shown. Both beams are well separated. The amount of decelerated beam is about 12%.

gaps and an internal quadrupole triplet lens for transverse focusing [Dah04]. All elements are copper plated. Deceleration takes place when the beam is within the gaps and sees the RF-field in the resonant cavity. While the beam is shielded within the drift tubes, the RF phase is switched. Since the lengths of the drift tubes become shorter on the way from injection to extraction, the beam is always in phase with the RF-field. Existing power supplies were used, so that the IH works at a frequency of 108.408 MHz, with a peak power up to 200 kW. In order to decelerate ions with $m/q \leq 3$ from 4 MeV/u to 0.5 MeV/u an effective voltage of 10.5 MV is required. The calculated transmission of the IH-linac is 70%. The IH was commissioned in two beamtimes in August and October 2008. A decelerated beam has been seen, but with very low transmission. The IH was retuned and tested again in February 2009. Here the yield of ions with an energy of 500 keV/u was measured to 12% using beam profile measurements with a diamond detector (see figure 2.15). This is still well under the nominal transmission, so that further tuning is necessary.

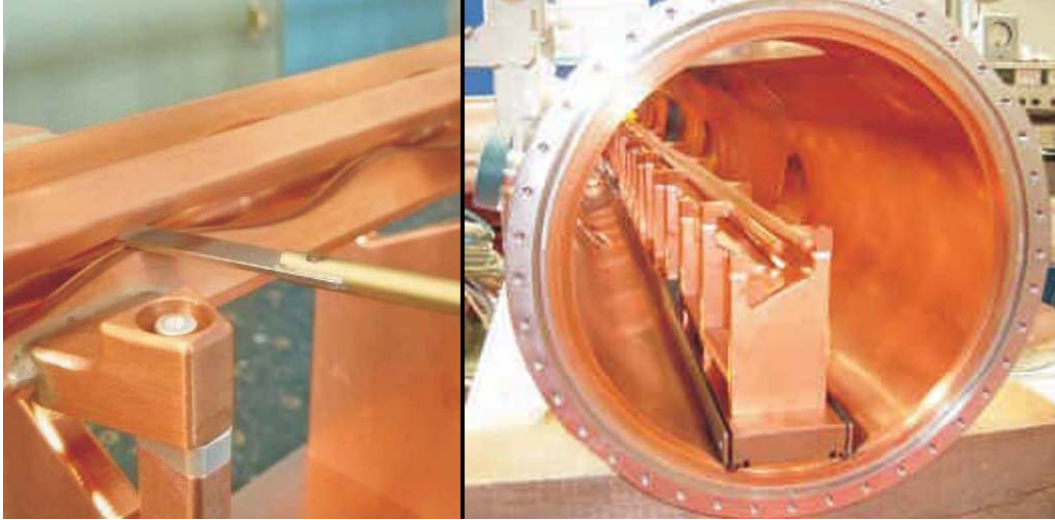


Figure 2.16: The radio-frequency quadrupole.

The sinusoidally modulated rods (left) and the tank with the four rod structure (right) of the radio-frequency quadrupole is shown [Hof08].

2.4.3 The Radio Frequency Quadrupole Decelerator

A radio-frequency quadrupole (RFQ) decelerator uses electric RF fields applied to four longitudinally modulated rods or 'vaness' to confine the beam transversely and decelerate it in the longitudinal direction [Wan98]. This kind of device is used at the AD at CERN to decelerate antiprotons [Lom01]. The HITRAP RFQ is designed for ion species with $m/q \leq 3$, which allows for a relatively short length of 1.99 m. Details on the design and the construction can be found in B. Hofmann's PhD thesis [Hof08]. It is a four rod structure, that follows closely the design of the High Charge Injector at GSI [Fri91], and allows for a maximum rod voltage of 77.5 kV. The internal structure is shown in figure 2.16.

The beam coming from the IH with a phase width of 45° has to be matched to the acceptance of the RFQ, which is 20° . This is done by a two-gap spiral rebuncher directly in front of the RFQ, which has a nominal transmission efficiency of 95%. At the RFQ's exit a single harmonic debuncher is positioned to lower the energy spread of the beam, which is needed for efficient trapping in the Cooler Trap. The beam energy spread is reduced from $\pm 7\%$ to $\pm 4\%$, nonetheless the transverse emittance is estimated to be about $100 \pi \text{ mm mrad}$ due to nonlinearities in the beam optics. This leads to an overall efficiency of the combined RFQ and debuncher of 85%. The complete structure is assembled and conditioned. It was commissioned in a beamtime in April 2009. Transmitted particles were seen behind the RFQ, but with undefined energies. A 4 MeV/u beam was still detected after the RFQ. Another commissioning beamtime is planned for the second half of 2009.

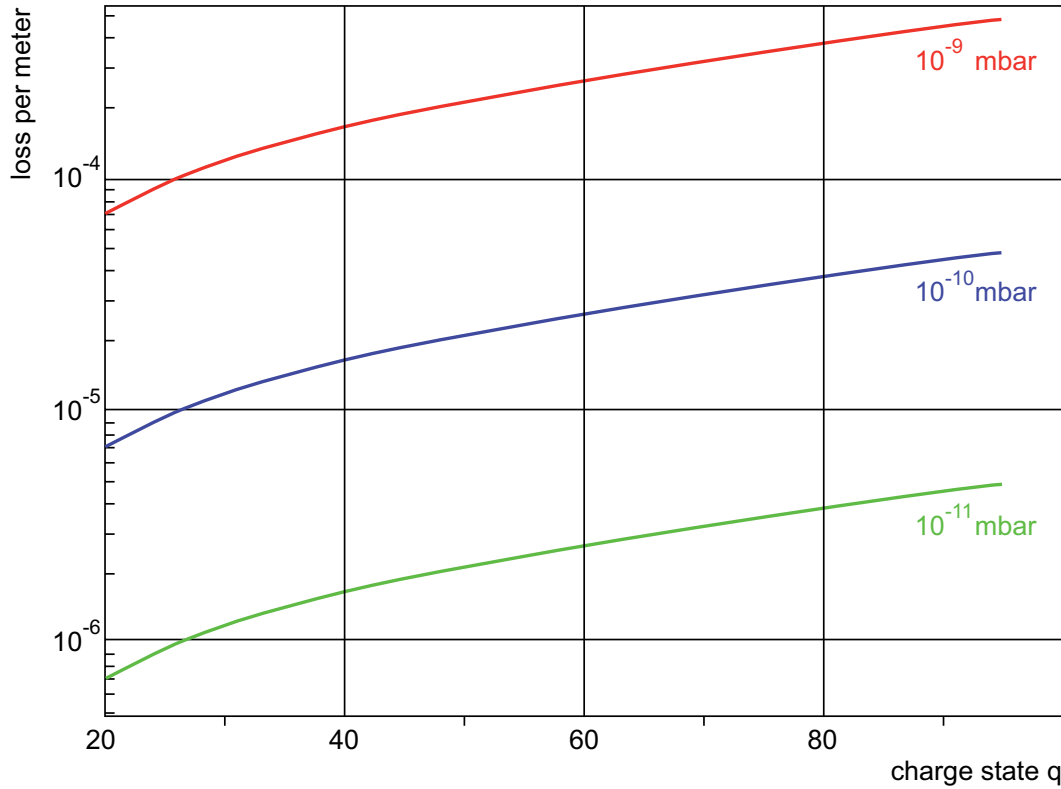


Figure 2.17: Velocity independent ion loss due to charge exchange over charge state q . Calculated from the Schlachter model [Sch84] for ion energies below 25 keV/u.

Summarizing we find that the deceleration from 4 MeV/u to 6 keV/u will be accomplished by the HITRAP decelerating stage. With an overall transmission efficiency of 55% and an injection of some 10^5 ions from the ESR we can expect to get at least 10^5 ions into the low-energy part of HITRAP.

2.4.4 The Low Energy Beam Transport (LEBT)

The Low Energy Beam Transport (LEBT) line connects the decelerator with the Cooler Trap. Whereas the decelerator beamline can work with a standard vacuum of 10^{-8} mbar, the cooling time of at least 10 s requires a much better vacuum in the Cooler Trap due to loss from charge exchange reactions [Sch84, Man86]. Between 10 eV and 25 keV/u the cross section for one electron capture is described by the velocity independent semi-empirical formula [Sch84]

$$\sigma_{q,q-1} = 1.43 \cdot 10^{-12} q^{1.17} I^{-2.76} [cm^2], \quad (2.10)$$

where q is the ion's initial charge state and I the ionization potential of the residual gas. For U^{92+} a cross section of $5 \cdot 10^{-13} cm^2$ is calculated. The losses per meter are plotted in Fig. 2.17. A pressure of 10^{-9} mbar gives a loss rate of about 0.1 %/m. With these numbers it can be estimated that a maximum pressure of 10^{-13} mbar is needed in the trap to keep the losses below 10^{-3}

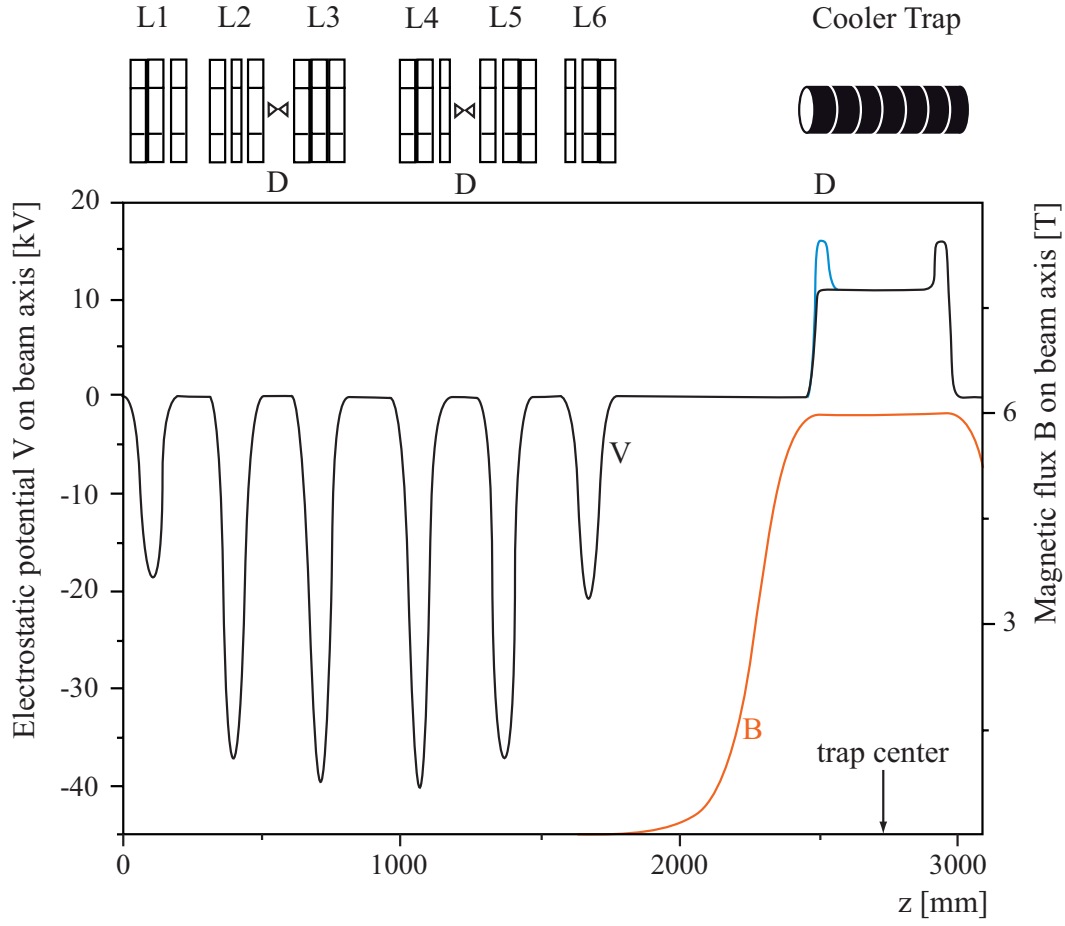


Figure 2.18: Electrostatic potential and magnetic flux on the LEBT axis.

The beamline lenses (L1÷L6), diaphragms (D) and the Cooler Trap are indicated at their position (sketch not to scale). The trap endcap constitutes the last diaphragm. The solid black/blue line in the diagram below represents the electrostatic potential with the trap open/closed and the orange line shows the magnetic field of the trap solenoid.

within a storage time of 10 s [Her05].

Therefore the LEBT should serve two purposes: First it decouples the vacuum of the trap from the one in the decelerator beamline. To achieve this, the LEBT contains two diaphragms serving as pumping barriers, whereas the endcap of the trap itself serves as a third pumping barrier. Three doublets of electrostatic Einzel-lenses focus the beam through the 8 mm diaphragms. The rms radius for the injection is given by ion optical simulations to be about 0.7 mm. In the magnetic field of the trap this radius will be frozen. The same simulations show an ion optical transmission of more than 90%. The potential distribution used for the simulations is shown on fig. 2.18.

In the LEBT the vacuum should range from 10^{-9} mbar on the RFQ side to

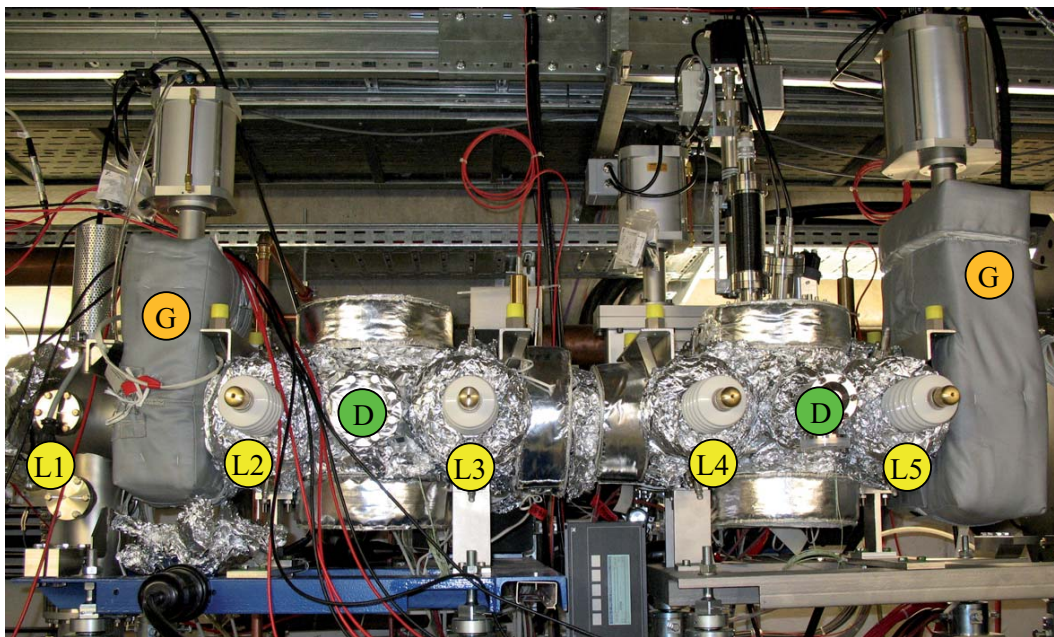


Figure 2.19: The LEBT installed in the reinjection channel. Lens positions (L1÷L5; L6 is not visible), diaphragms (D) and gate valves (G) are indicated in this photograph. The ion getter pumps are on the backside at positions L2 and L4.



Figure 2.20: LEBT Einzel-lens. The LEBT Einzel-lenses are build as grids to allow for better pumping.

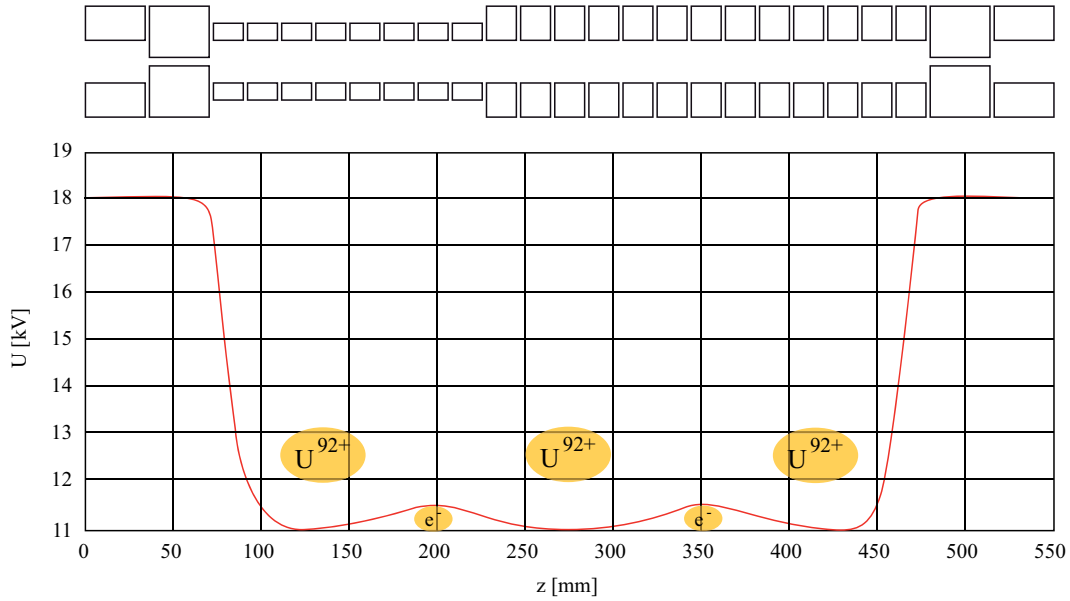


Figure 2.21: Nested trap configuration of the Cooler Trap.

The upper part shows a schematic cut through the Cooler Trap electrodes. The diagram underneath indicates the electric potential, which allows for simultaneous trapping of positive and negative charges in the hills and wells, respectively.

10^{-11} mbar at the trap side. This is achieved by two turbopumps at the flanges housing the first and the last Einzel-lens. Each pump has a capacity of 300 l/s. Supporting pumping power comes from two ion getter pumps at the positions of the second and the fourth Einzel-lens (see fig. 2.19). The electrodes of the Einzel-lenses are built as grids (see fig. 2.20), to enable efficient pumping.

To measure the beam position and quality at the diaphragms, two diagnostic arrays consisting of a Faraday cup, a micro-channel plate and a digital camera are housed in between lenses 2 and 3 and between lenses 4 and 5, respectively. Lenses 2 and 5 each have a fourfold split exit electrode to enable beam steering. The whole LEBT is bakeable at 200°C . All elements have passed baking tests and the LEBT has been set up in the reinjection channel.

2.4.5 The Cooler Trap

The Cooler Trap is a cylindrical Penning trap which allows for trapping and cooling of an ion cloud of 10^5 highly charged ions. The large number of particles as well as the possibility of electron cooling within the trap set challenging requirements for the trap design.

In our case a cylindrical Penning trap was chosen, since an ideal hyperbolic trap would not allow for an efficient in-flight capture of the beam. This is possible for the cylindrical, axially elongated trap. Here the entrance electrode

can be switched to a trapping potential before the ion bunch, which is reflected by the exit electrode, can escape. The minimal trap length is defined by the injection energy and the ion bunch length, whereas the costs for the solenoid delimit the trap length. For an one microsecond long bunch with an energy of 2 keV/u, efficient trapping is achieved with an effective trapping length of 400 mm [Her06a]. The Cooler Trap consists of 23 electrodes, which are brought into the center of a solenoid with a field strength of 6 T. This allows also for a so-called nested trap configuration (see fig. 2.21), which allows for simultaneous trapping of positive and negative charged particles, so that electron cooling can be applied. This technique has already been exploited in other trap facilities like the antiproton and positron confinement set-ups at CERN (ASACUSA [Ich01], ATHENA [Amo04], ATRAP [Gab99a]). The electrons come from a dedicated electron source at the backside of the trap.

Since recombination between ions and electrons, destroying the charge state of the HCI, becomes more efficient at low relative energies, electron cooling is stopped at an ion energy of about 10 eV by ejecting the electrons from the trap. Further cooling is achieved by resistive cooling. This can be conducted unto the thermal equilibrium of the ions and the resonant cooling circuit. Therefore the complete trap set-up including the resonant circuit will be at 4 K. Further discussion of the cooling mechanisms and the circuit can be found in chapter 3.2.2. Another reason for the cryogenic trap environment is the benefit for the vacuum conditions - which should be, as mentioned before, in the range of 10^{-13} mbar - since most background gas components will freeze out.

2.4.6 The Vertical Beamline and EBIT

The different experiments presented in the next section will require different beams. The trap-based experiments like mass and g -factor measurements as well as laser spectroscopy will need short bunches for in-flight capture, whereas collision experiments rather need quasi-continuous beams. Therefore two different extraction modes from the Cooler Trap are foreseen: pulsed mode - i.e. fast switching of the trapping voltages - and quasi-continuous mode - i.e. slow lowering of the electric potential resulting in the ions leaking from the trap.

As the experiments are on top of the reinjection channel, the extracted ions have to cover a height of 4.85 m by crossing the concrete shielding. An existing 90° dipole bender magnet with double focusing is employed to bend the beam upwards and clean the recombined ions from the sample. On top of the channel a spherical bender directs the beam to the experiments. This bender guarantees a transverse focusing in horizontal and vertical direction which keeps a symmetric beam. The other optical elements are electrostatic and the beam diagnostics used are the same as in the LEBT. The vacuum considerations done for the Cooler Trap based on the charge exchange model by Schlachter also hold for the Vertical Beamline. As shown in figure 2.17, a

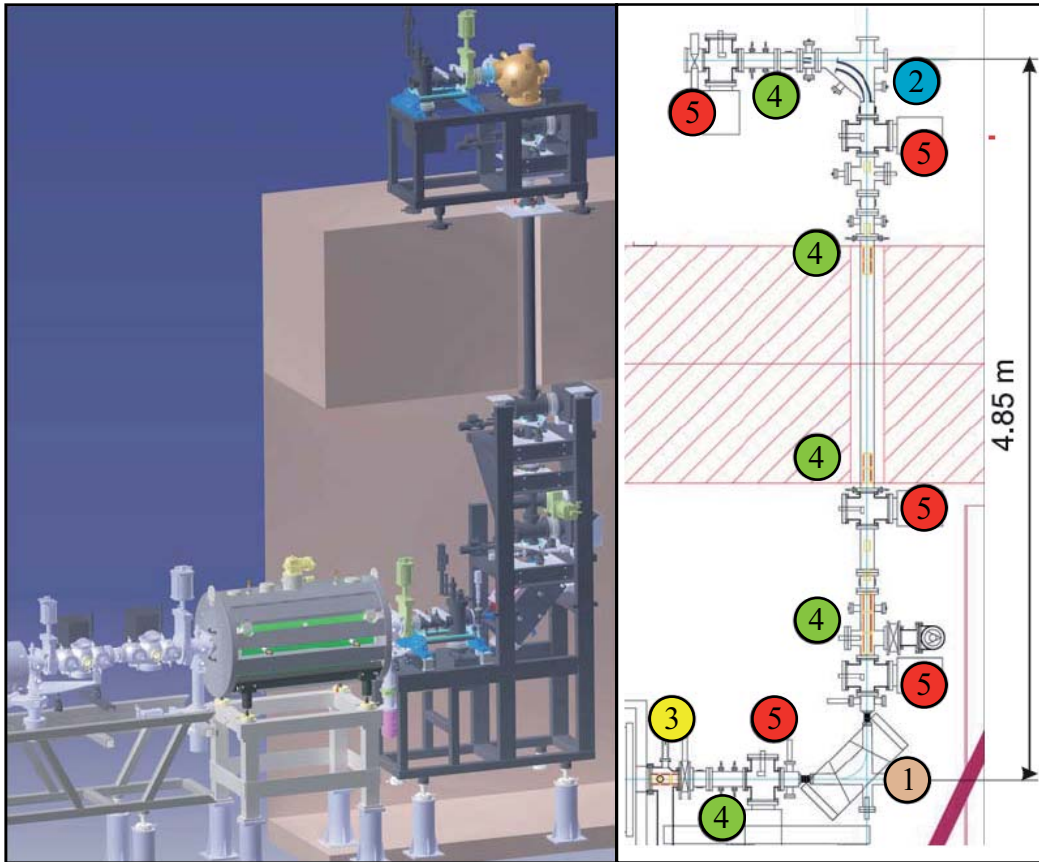


Figure 2.22: The Vertical Beam Transport beamline.

Coming from the Cooler Trap, the beam is deflected upwards by a 90° magnet (1), which also acts as charge state selector. After crossing the concrete shielding it is bent back horizontally by an electrostatic kicker-bender (2) to be sent to the experiments. The Einzel-lenses (3) and quadrupoles (4) are electrostatically focusing elements. Diagnostic and pumping stations are indicated (5).

vacuum of 10^{-10} mbar is needed to keep the losses in the order of 10^{-4} at a length of 10 m. To reach this, baking and ion getter pumps will be employed along the beamline. This is not possible for the 1.6 m of beamline which will be inside of the concrete shielding. Here the tube will be coated with non-evaporable getter (NEG) material to reduce the outgasing surface [Her05].

Since beamtime at the ESR is limited, it is reasonable to have an offline ion source on site. Therefore, a commercial room-temperature Electron Beam Ion Trap (EBIT) has been bought. This is at the moment being installed on top of the reinjection channel perpendicular to the beamline guiding the ions to the experiments and next to the spherical bender. It can provide highly charged ions up to Ar^{18+} or Xe^{46+} in pulsed or in DC mode [DRE08]. The EBIT can be used as a highly charged ion source to perform tests of the experimental set-ups and the Cooler Trap as well as for measurements with medium-heavy HCI. An electrostatic kicker combined with the bender will inject the beam

extracted from the EBIT to the Vertical Beamline, which allows the transport back to the Cooler Trap, where the sample is prepared for the experiments.

2.4.7 HITRAP experiments

A large variety of physics questions can be addressed with the cold ions delivered by HITRAP. The experiments to address these questions were developed between 2001 and 2006 in the EU RTD network HITRAP. The experiments range from high-accuracy mass measurements, measurements of the bound-electron g -factor and laser spectroscopy to collision studies with surfaces and gas jets. The experiments will be briefly explained.

Mass measurements

The mass of a nuclide is of great interest, since its knowledge provides insights into the nuclear structure and the nucleosynthesis processes [Arn99, Sch06a]. From the comparison of different species binding energies and Q -values can be extracted. QED tests as well as new inputs to crucial points in the Standard Model - the Conserved Vector Current (CVC) as well as the unitarity of the Cabibbo-Kobayashi-Maskawa (CKM) matrix - are possible by high-accuracy mass measurements [Har01].

Due to the very long storage time, dedicated Penning traps are excellent mass spectrometers. Masses can be derived from the eigenmotions of the ions in the trap, yielding the true cyclotron frequency $\omega_c = qB/m$ by the relation $\omega_c = \omega_+ + \omega_-$ or $\omega_c^2 = \omega_z^2 + \omega_+^2 + \omega_-^2$ (invariance theorem [Bro86]). Measuring the cyclotron frequency of a well known reference mass m_{ref} yields an accurate value for the magnetic field strength B . Using formula 2.11 the mass of the species of interest can be easily obtained.

$$\frac{m_i}{m_{ref}} = \frac{\omega_{ref}}{\omega_i}. \quad (2.11)$$

The cyclotron frequency can either be obtained in a destructive way like the time-of-flight (TOF) method currently applied at SHIPTRAP (see section 2.3.4), or by a non-destructive detection of the image current induced by a single ion in the trap [Bla06]. Accuracies in the order of 10^{-11} have been achieved on singly charged ions using the latter method [Bra99]. The mass resolving power is given by

$$R = \frac{m}{\Delta m} = \frac{\omega_c}{\Delta \omega_c}, \quad (2.12)$$

which shows clearly that the precision of the mass measurement can be significantly improved by the use of heavy, highly charged ions. Due to the ion preparation scheme of HITRAP the experiments are here limited to stable nuclei or species with a half life of at least 20 s. A dedicated mass measurement Penning trap is being built in Heidelberg in close collaboration with GSI [Her06], aiming at an uncertainty of $\delta m/m < 10^{-11}$.

g-factor measurements

A second dedicated Penning trap experiment for HITRAP is the *g*-factor trap developed by the Mainz-GSI-collaboration [Alo07]. The measurement of the *g*-factor of a bound electron in a hydrogen-like ion is a sensitive QED test [Bei00]. g_{bound} can be written as

$$g_{\text{bound}} = 2 \frac{q}{e} \frac{m_e}{M_i} \frac{\omega_L}{\omega_c}, \quad (2.13)$$

where m_e , M_i are the masses of the electron and the ion, respectively, and e , q their charges. ω_L is the Larmor spin precession frequency and ω_c the cyclotron frequency.

To measure the *g*-factor an innovative trap set-up has been conceived using the continuous Stern-Gerlach effect. The experiment consists of two traps: one so-called precision trap with a highly homogeneous magnetic field and an analysis trap with a quadratic inhomogeneous field of the type $B_2 z^2$. The inhomogeneous region is realized by a nickel ring as a trap electrode [Häf03]. ω_c is determined using the image current method, while ω_L is determined via the continuous Stern-Gerlach effect, since the magnetic potential in the analysis trap seen by the particle has a different sign depending on the spin position. This results in a different force on the particle proportional to $\mu \partial B / \partial z$ (μ being the magnetic moment of the particle) and therefore in a different axial frequency. Spin flips on the single ions can be resonantly induced in the precision trap and then detected in the analysis trap. The excitation frequency yielding most spin flip events equals ω_L . Up to now experiments have obtained *g*-factors of $^{12}\text{C}^{5+}$ [Häf03] and $^{16}\text{O}^{7+}$ [Ver04] with a relative accuracy of 10^{-9} . Those showed a perfect agreement with theory. From these experiments the mass of the electron can be determined using the theoretical value of *g* and inverting formula 2.13 [Bei03a]. The uncertainty of the electron mass given by the CODATA group is now with $\delta m/m \sim 4 \cdot 10^{-10}$ about five times better than the previously accepted value [Moh08]. For the upcoming experiments on uranium at HITRAP the same accuracy is expected. This is a sensitive test of bound-state QED in extreme fields and might yield a new value for the fine structure constant α [Sha06] with a higher accuracy than the value obtained from the *g*-2 measurement of the free electron by the Seattle group [Dyc87]. Very recently the uncertainty in α was improved to 0.37 ppb by the Harvard group [Han08]. But although the *g*-factor measurements of the bound electrons cannot reach the present accuracy in α from free electron experiments, it would yield a completely independent value for this fundamental constant.

Laser spectroscopy

For heavy highly charged ions with $Z \geq 60$, the energy of the ground-state hyperfine splitting (which scales with Z^3) can be excited with visible laser light. The fluorescence rate from magnetic dipole (M1) transitions is enhanced for heavy HCl, since the lifetime of the excited state scales with Z^{-9} . One can now rule out to first-order nuclear effects by measuring the M1 transition in

hydrogen-like and lithium-like ions of the same nuclide. This allows the precise determination of bound-state QED effects on the atomic level structure. The experiments performed until now in storage rings [See98] are strongly limited in accuracy by the Doppler effect. Experiments in an EBIT [Bei00] are in addition limited by a poor signal-to-noise ratio.

To overcome these limitations a dedicated laser spectroscopy trap (SPECTRAP - SPECTroscopy TRAP) is being set up at GSI. It employs a Penning trap, which has an optically transparent mesh as central electrode. The measurement will employ the rotating wall compression [Gre00] to gain from a high particle density. Due to the low energy of the particles in the trap, the Doppler effect is small. The accuracy expected to be reached is three orders of magnitude better than in the measurements before [Vog05].

Collision studies

One of the experimental set-ups under preparation addresses the interactions of slow HCI impinging on a surface [Lem05]. The electron emission in dependence on the ions charge state and energy as well as the type of surface is to be measured [Khe98]. An experimental evidence for the predicted trampoline effect - the repulsion of the still positively charged impinging ion by the locally ionized surface [Bri96] - is also looked for in this experiment. New information on the level schemes in highly charged ions are gained with X-ray spectroscopy of the formation and decay of hollow atoms.

Another type of collision studies to be conducted at HITRAP are the interactions of slow HCI with gas jets. In these reactions charge exchange processes dominate [Dör00]. The experiments with complete kinematics are done with the reaction microscope and the COLTRIMS (COLd Target Recoil Ion Momentum Spectroscopy) technique [Ull03]. In combination with this set-up, x-ray spectroscopy is possible with additional solid-state detectors.

Chapter 3

The HITRAP Cooler Trap

In this chapter an overview on the HITRAP Cooler Trap and the relevant electronic parts is given. After describing the design of the trap, the fourier-transform ion-cyclotron resonance (FT-ICR) detection method in its relevance for the axial and cyclotron ion motion detection and cooling at HITRAP will be discussed. The demands on the detection electronics as well as the design of the LC circuits and amplifiers for HITRAP will be explained in more detail.

3.1 The design of the HITRAP Cooler Trap

The HITRAP Cooler Trap should allow for efficient trapping and cooling of an ion cloud of 10^5 highly charged ions. The ion bunch coming from the decelerator has a length of $1.2 \mu\text{s}$ and an energy of 6 keV/u . To cool the trapped ions electron cooling and resistive cooling should be employed. The ion motions should simultaneously be monitored to follow the cooling process. After the final temperature of 4 K is reached, the ions should be extracted to the experiments either as a bunch or in quasi-continuous mode. These are challenging requirements for the trap design.

The HITRAP Cooler Trap has been designed as part of the PhD thesis of G. Maero [Mae08]. To allow for **efficient trapping** of the incoming ion bunch, an elongated cylindrical Penning trap was foreseen already in the Technical Design Report [TDR03] presenting the technical guidelines of the HITRAP project. But still most of the bunch would be reflected at the exit endcap and leave the trap, before the entrance electrode could be switched to trapping potential (about $15\text{-}18 \text{ kV}$, due to the beam energy of 6 keV/u for U^{92+} with a mass-over-charge ratio of 2.6). Keeping the trap at a base voltage of 11 kV decelerates the beam to about 2 keV/u before trapping. This results in a trapping length of 400 mm , which gives a time window of 400 ns to switch the entrance electrode to trapping potential [Her06a]. This task is to be done by a fast Behlke switch with a maximum DC voltage of 16 kV and rise time of $\leq 60 \text{ ns}$ (HTS 161-06-GSM type MOSFET push-pull) [Beh09].

There are two confinement restrictions for a **large number of particles**

in a trap. First the radial confinement is limited by the particle density. A plasma in a quadrupolar trapping potential will take ellipsoidal shape and rotate rigidly along the z-axis [Dub99]. Radially the centrifugal force, the magnetic force and electrostatic repulsion balance out. From a certain density on - the so-called Brillouin-limit n_B - this balance is destroyed and radial confinement is lost. The second limit is the space-charge (also called self-field) of the trapped particles' charge distribution, which flattens the trapping potential. If enough ions are in the trap, the trapping potential will be flattened up to the endcap voltage and therefore additional particles do not see a trapping potential anymore.

The superconducting solenoid creating the magnetic field for the Cooler Trap has a maximum field strength of 6 T. In this case the Brillouin limit is $4 \cdot 10^8$ particles/cm³ for U⁹²⁺ and $1.75 \cdot 10^{14}$ particles/cm³ for electrons. For simultaneous trapping of both species - i.e. using the lower limit - and a conservative maximum density assumption of $0.2 \cdot n_B$ this yields trapping volumes of 1.25 mm³ for 10^5 bare uranium ions and 125 cm³ for 10^{10} electrons [Mae08]. The latter number is the volume of a 400 mm long trap with an inner diameter of 10 mm. To reduce losses on the trap electrodes a larger diameter is desirable. The diameter is restricted by the magnet's bore inner diameter of 150 mm and the fact that the cryogenic electronics have to fit into the bore as well. The electronics have to surround the trap since we want to eject the ions on the far side of the injection. Thus an inner radius of 17.5 mm for the trap electrodes was chosen.

The Cooler Trap should enable the simultaneous trapping of electrons and ions for **electron cooling**. This is possible in a nested trap configuration, where potential wells and hills are created within the trap to confine ions and electrons, respectively. This kind of trap operation has been used to produce antihydrogen in the ATRAP [Gab99a] and the ATHENA [Amo04] experiment at CERN. A central potential well for HCI is useful to monitor their dynamics over the complete trapping time. We decided for a nested trap with five potential wells and hills, three for ions and two for electrons, respectively (see fig. 2.21). Electrons injected into the trap cool fast via emission of synchrotron radiation. The subsequently injected hot HCI transfer energy by Coulomb collision to the electrons (which dissipate this energy again by synchrotron radiation emission) and cool into the wells. To prevent recombination, the interaction of the HCI and the electrons can be interrupted either by increasing the potentials of the nested trap configuration, or by sweeping the electrons from the trap. In the latter case, a reheating of the ions due to the electronic pulse has to be prevented by keeping the pulse length short - in the order of a 200 ns. Then the ions are gathered in the center well, where resistive cooling is applied.

The initial technical design [TDR03] foresaw an orthogonal trap configuration for each nested trap. This configuration is widely used in precision spec-

troscopy traps for single ion measurement - as in SHIPTRAP - and uses the *orthogonal anharmonicity compensation* [Gab84, Bro86]. Since in the Cooler Trap a large number of ions will be stored and no single ion precision measurements shall be employed, the advantages and disadvantages of such a trap configuration have been investigated [Mae08]. The advantage of a high harmonicity restricts the effective trapping length and can only be exploited if geometrical and potential centers coincide. Both are disadvantageous for the trapping of a large ion bunch. If we move the potential center, we degrade the harmonicity severely. Furthermore the high space-charge of 10^5 U^{92+} most probably limits the harmonicity anyway.

Multi-ring traps (MRT), on the other hand, have limited harmonicity. A MRT consists of an arbitrary number of geometrically identical electrodes. This gives the advantage of shaping the potential in the same accuracy everywhere in the trap. An MRT trap has already been used successfully at other trap experiments, like MUSASHI-ASACUSA [Ich01, Kur05]. A look at the harmonicity shows, that the MRT gives a good harmonic approximation over a greater length than the orthogonal trap due to the larger distance between the endcaps. With the proper potential shaping, the higher order terms are not much worse than in an orthogonal trap [Mae08].

Taking all this into account, the final design of the Cooler Trap was chosen as a 21 electrode multi-ring trap. The electrodes have an inner radius of 17.5 mm, a length of 17 mm and the spacing between them is 2 mm. The two endcaps are longer (34.75 mm) and have a smaller inner radius (5 mm), since they also act as pumping barriers. This design of the endcaps also reinforces the trapping potential in the trap. Two electrodes are added outside the endcaps to stabilize the field outside the trapping region. The effects of construction and alignment imperfections have also been investigated [Mae08]. A worst case analysis showed, that the possible distortions are practically negligible for our application due to the large inner trap radius.

3.1.1 Working cycle of the Cooler Trap

Figure 3.1 shows the main steps in the working cycle of the Cooler Trap. The complete cycle time should match or be lower than the ESR cycle time, which is between 17 and 46 s. One cycle consists of the following steps:

1. Injection of 10^{10} low energy electrons for the electron cooling. The electrons are produced by a photoionisation electron source between Cooler Trap and Vertical Beam Transport.
2. After injection the trap is closed for the electrons, which cool by synchrotron radiation and are trapped in their respective trapping potentials.
3. The entrance electrode is opened and the exit electrode is set to the trapping potential for the ions (7 kV).

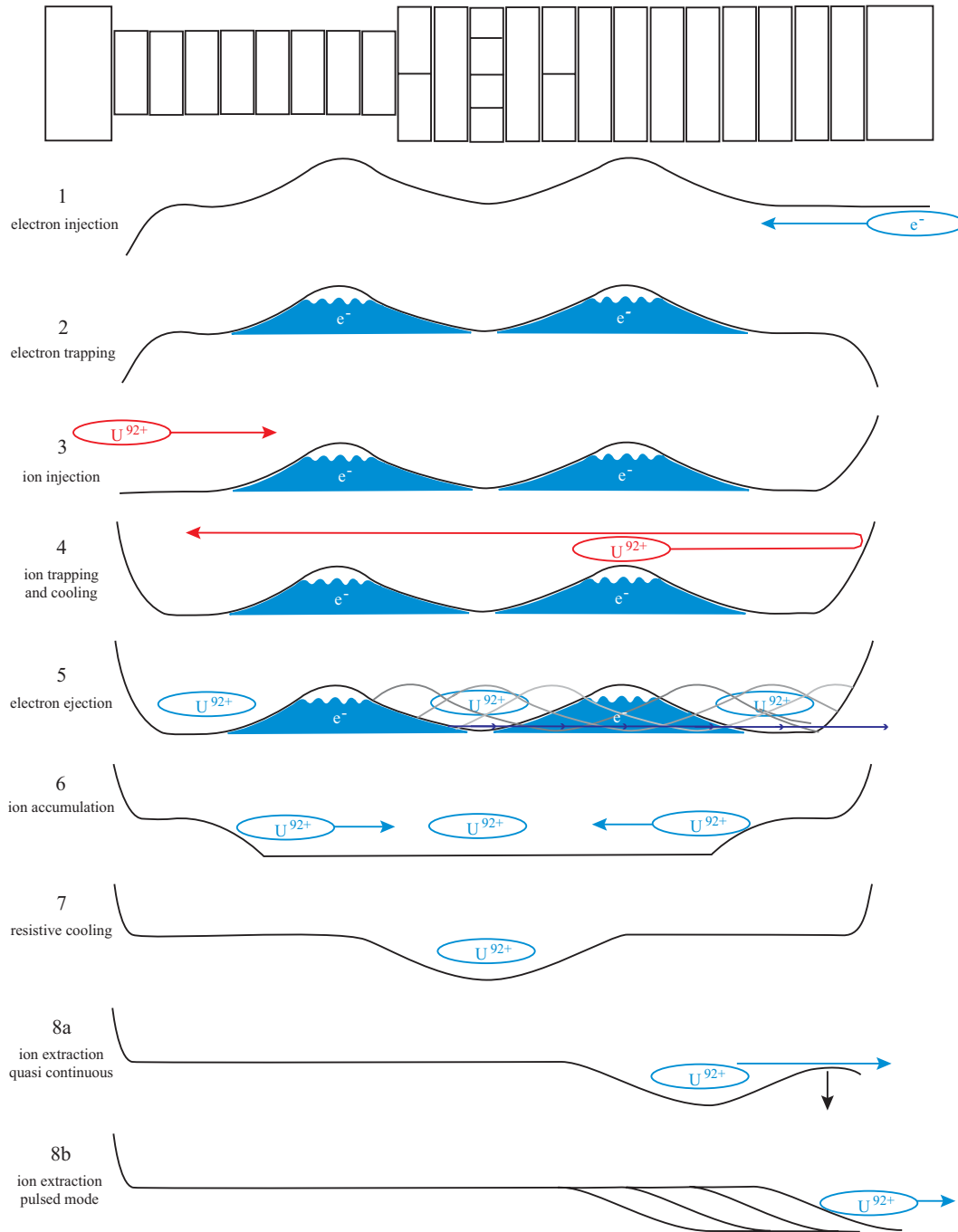


Figure 3.1: Working cycle of the Cooler Trap. At the top a sketch of the Cooler Trap electrode stack is shown. Underneath the most important steps for the timing sequence are schematically drawn. (1) is the loading of the electrons from the traps rear side, in (2) the nested trap is closed and the electrons cool into the according potentials. Then (3) the entrance electrode is lowered and the ions are injected. The entrance electrode has to be switched back to close within 400 ns (4). After the electron cooling has been applied, the electrons are swept from the trap (5). In (6) all ions are shifted to the central trap, which is finished in (7). After resistive cooling, the ions can be extracted in quasi-continuous mode (8a) or bunched mode (8b). The endcap potentials are not shown to their full extent.

4. The ions are injected. To trap the ions, the entrance electrode has to be switched to trapping potential within 400 ns. The trapped ions cool by Coulomb collisions with the electrons within 1.5 s down to about 10 eV.
5. To prevent ion loss by recombination electron cooling is stopped at 10 eV by sweeping the electrons from the trap. Therefore a very fast pulse in the order of 200 ns is needed, so that the ions do not heat up by the electrode switching.
6. The ions from the three nested traps are accumulated in the central trap.
7. Here resistive cooling down to 4 K is employed (a detailed description of both cooling techniques is found in the next section). The center-of-mass motion is cooled within 100 ms. Other degrees of freedom cool much slower (with a time constant of 3.7 s).
8. The ions are extracted either
 - a) as a bunch. Then the exit electrode is switched fast, so that all ions can escape together.
 - b) in quasi-continuous mode. Here the exit electrode is switched slowly, so that always just the 'hottest' ions can escape.

After the ion extraction, the cycle starts anew. Summing all time steps needed in the working cycle, we see, that efficient trapping, cooling and ejection of the ions is possible within one ESR cycle of 17 s. If the ESR cycle is longer, the time for resistive cooling can be prolonged, leading to a better cooled ion sample.

3.2 Ion detection and manipulation at HITRAP

At HITRAP we will monitor the ions in the trap using an image current detection technique. We monitor both the cyclotron as well as the axial motion of the ion ensemble. The technique used for the cyclotron motion is called Fourier-transform Ion-Cyclotron-Resonance (FT-ICR). For the axial motion detection the same principles apply. The resonant circuit used serves simultaneously both purposes: the detection and cooling of the ion motion. Here the technique as well as the required electronics will be discussed in detail. An FT-ICR detection system for SHIPTRAP is foreseen and has been developed [Ket06], but is not installed yet.

3.2.1 FT-ICR

The ions in the trap induce an alternating current in the trap electrodes with the frequency of their motion. This can be measured with broadband electronics or - as in the case of HITRAP - in a narrowband set-up using a resonant circuit tuned to the frequency of interest, which acts as a band filter. The basic

idea of induced currents is, that the potential at a conducting surface should be the same in all points on the surface. If now a charge A is brought close to the surface, it induces an image charge Q_A in the surface, which cancels the potential from charge A . If charge A moves periodically to and fro, the image charge Q_A will also oscillate. The induced current depends on the velocity of the image charge \vec{v} and its distance \vec{d} to the surface

$$i = \frac{q\vec{v}}{d} \quad (3.1)$$

If one connects the surface to a circuit with an ohmic resistor it is possible to dissipate energy from the system [Deh68]. But for effective detection and cooling an ohmic resistor is not suitable. The most common solution is the use of a parallel RLC circuit, which combines a highly effective resistance with easy signal outcoupling, which is realized with an inductively coupled secondary coil. The circuit consists of two electrodes, which are connected via an inductive coil. The capacitance in the RLC circuit is realised by the parasitic capacitances of the wires and electrodes, while the resistance is the real part of the coils impedance. The parallel RLC is a band filter with a peak at the frequency determined by $\omega_{RLC} = 1/(LC)^{1/2}$.

The cyclotron motion at HITRAP is monitored using two segments of the radially eightfold split central electrode. This geometry can be approximated by two parallel plates [Sch91]. The non-flat shape of the electrodes introduces a geometrical factor [Sta98], which alters the distance \vec{d} , giving an effective electrode distance D_{eff} instead. The image current is converted into a voltage by the resonant tuned circuit. For cooling and detection purposes the tuned circuit has to match the frequency of the ion motion, since the resistance has a sharp peak here. This means, that a maximum of energy is dissipated and the detection signal is highest. For 10^5 bare uranium ions we expect a current of some nano-Ampere for the cyclotron motion and some tens of micro-Ampere for the axial motion. The effective image current is given by

$$I_{eff} = \frac{\sqrt{2}\pi q \nu_{ion} r_{ion}}{D_{eff}} \quad (3.2)$$

with ν_{ion} being the ions frequency and r_{ion} the ion motions amplitude. According to the ohmic law, this current generates a voltage drop. The peak resistance of a resonant circuit is given by

$$R = \frac{Q}{\omega_{RLC}C} \quad (3.3)$$

Q - the so-called quality factor - is a measure for the sharpness of the resonance peak. It is defined as the ratio of the resonant frequency ω_{RLC} over the 3 dB (i.e. $0.707 V_{max}$) line width $\Delta\omega$

$$Q = \frac{\omega_{RLC}}{\Delta\omega} \quad (3.4)$$

The voltage signal from the resonant circuit is given as

$$U_{eff} = R \cdot I_{eff} = \frac{1}{\sqrt{2}} \frac{r_{ion}}{D} q \frac{Q}{C} \quad (3.5)$$

The voltage signal in the time domain is coupled out inductively and then transformed to the frequency domain via a Fast Fourier Transformation (FFT) (see appendix A).

3.2.2 Cooling of the ion motion

At HITRAP two cooling techniques are employed, electron and resistive cooling. The basic idea of **electron cooling** is that the hot ions loose energy via Coulomb collisions with a cold electron sample. The electrons stay cool, since they loose their energy fast by synchrotron radiation. This mechanism works fast enough to allow for a cooling cycle under 20 s, as is intended for HITRAP. The major disadvantage is the ion loss by recombination, which enhances with lower relative energies.

On the electron cooling process in a Penning trap extensive simulation studies were done, as presented in [Zwi05], [Zwi06] and [Ner07]. The HITRAP related studies using a sample of 10^5 ions at an energy of about 1.5 keV show the following picture (see figure 3.2): as soon as the ions are introduced, the electron temperature rises fast (in less than 0.5 s) about four orders of magnitude from 4 K (≈ 0.35 meV), while the ion energy decreases continuously. As soon as the ion energy gets low enough, the energy exchange decreases, leaving the synchrotron radiation of the electrons being the dominant process. After some time the ion temperature would equilibrate with the electron temperature and subsequently cool down to 4 K. But at small relative energies the ion loss through recombination processes gets high (therefore the loss of ion survival probability $\langle P_{RR} \rangle$ in figure 3.2, on the right), which means that the electrons and ions have to be separated. This separation will be accomplished by sweeping the electrons fast - sweep puls of about 200 nanoseconds - from the trap. A fast electrode switching ensures the removal of the light electrons, while the heavier ions will not be affected. These studies yield an optimal value for the electron density of 10^7 cm^{-3} and for the electron number of 10^9 . If we stop the cooling process at 10 eV ion energy, $\langle P_{RR} \rangle$ is still about 90%. Taking all this into account, we expect efficient cooling of the ions in about 1.5 s.

After the electron cooling has been stopped, **resistive cooling** will take over. The principle of resistive cooling ties in with the principle of image currents we used for the ion motion detection (section 3.2.1). The resistance in equation 3.5 corresponds to an energy dissipation from the system by the ohmic resistance, which leads to a damping of the ion motion, i.e. the ion motion is cooled. The cooling stops when the image current signal gets in the order of the Johnson noise - the thermal noise of the electronics, depending

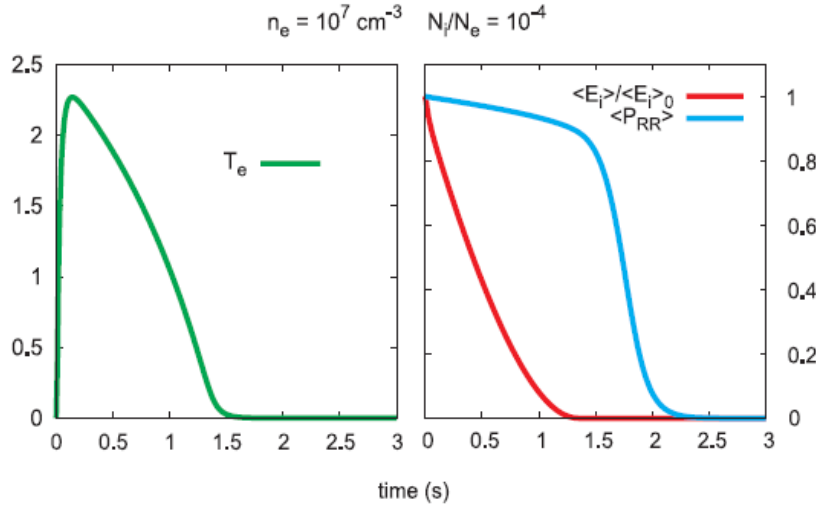


Figure 3.2: Electron cooling of 10^5 U^{92+} ions. The diagram left shows the electron temperature versus time. t_0 indicates the time of ion injection. The right side shows the mean ion energy $\langle E_i \rangle$ normalised to the initial mean energy $\langle E_i \rangle_0$ in red, while blue is the mean survival probability $\langle P_{RR} \rangle$ to electron-ion recombination. n_e is the electron density, N_i and N_e the numbers of ions and electrons, respectively. This is the diagram for optimal settings [Zwi05].

on the ambient temperature. This means, that the final ion temperature is defined by the ambient temperature of the electronics. Therefore the trap and the detection/cooling electronics are immersed in a 4 K environment.

Equation 3.3 shows, that the peak resistance depends on the Q-factor. A high Q-factor leads to efficient energy dissipation in the coil, which corresponds to a strong cooling rate. On the other hand a high Q-factor means a small bandwidth. This again limits the number of cooled ions, since those with an oscillating frequency too far off from the peak frequency will experience a much smaller resistance. Simulations have shown, that a lower Q and therefore a broader bandwidth matching the frequency distribution of the trapped ions might be preferable [Mae08].

To calculate the cooling rate, we resume equation 3.1. Using the ohmic dissipation $P = RI_{eff}^2$ and $v^2 = 2E/m$ we find the energy loss being

$$P = \frac{dE}{dt} = \frac{Rq^2}{mD^2}E \quad (3.6)$$

This yields an exponential decay with a time constant

$$\tau = \frac{mD^2}{Rq^2} \quad (3.7)$$

Resistive cooling can be applied for the axial as well as for the cyclotron motion. In case of the axial motion the electrodes used are on each side of the

central electrode; in case of the cyclotron motion we use two segments of the eightfold split electrode. The dominant cooling at HITRAP will take place via the axial motion.

In case of the axial motion and for an ensemble of N ions with the same mass and charge state, the current induced depends on the center-of-mass motion (v_{CM}), rather than on the individual motions of the ions. This alters equation 3.1 to

$$i = N \frac{q}{D} v_{CM} \quad (3.8)$$

However, the dissipated energy does not scale as N^2 and the cooling is not N times faster than the cooling of a single particle. The power dissipation is still $\propto N$, when averaged over the ensemble, due to the phase difference between the individual particles (see [Maj04]). Important is the fact, that only the center-of-mass motion is effectively cooled, while all other degrees of freedom are untouched. Since the energy content of these internal degrees of freedom rises with the number of particles in the ensemble, that would mean we cannot dissipate the majority of the energy.

But those other degrees of freedom are addressed by non-linearity effects in a real trap. Here the linear approximation of equation 3.1 does not hold absolutely, due to slight misalignment or production imprecisions and contaminations of other charge states. Some higher order terms playing a role for large oscillation amplitudes come into play, which lead to a cooling beyond the pure center-of-mass (CM) motion. Anharmonicities experienced by the particles and partially recombined ions add to this effect. This contribution is small and leads to a long cooling tail - with $\tau \approx 3.7$ s after the fast (0.1 s) initial cooling of the center-of-mass motion [Mae08].

Another way to cool beyond the center-of-mass motion is asymmetric coupling of the RLC circuit. In this case we couple only to one side of the trap. By this we get sensitive to odd and even higher harmonics of the ion motion and even to breathing motions [Mae08].

3.3 Cryogenic electronics

As already mentioned, the crucial part of the detection and cooling electronics has to be at 4 K, since the minimum energy reachable is defined by the environmental temperature. The electronics should furthermore be close to the trap to keep parasitic capacitances of the connecting wires low. The signal from the RLC circuit is coupled out via a secondary coil to a preamplifier at 4 K. We wanted to use standard plastic printed boards without degrading the trap vacuum of 10^{-13} mbar, therefore we decided to put all electronics in a vacuum tight box. DC-noise filters for the power supply lines of the electrodes were designed and tested.

3.3.1 The electronics box

An electronics box, which houses all electronics next to the trap, was designed to not degrade vacuum conditions or contaminate the trap with outgassed and subsequently frozen organic components. The box was designed to fit around the first eight electrodes, which have an outer diameter of 40 mm. The magnet's bore has an inner diameter of 150 mm. To keep a safety margin to the electrodes and the magnet, the box was designed to be U-shaped with an inner diameter of 45 mm and an outer diameter of 140 mm. The greater margin on the outer side was chosen, since the box is on a potential of 11 kV with respect to the magnet. The length of the box was limited to the length of the 8 electrodes, 150 mm. The following electrodes have a bigger outer diameter. For changes and upgrades of the electronics, the inner part of the box is accessible via a lid on a flange, which is sealed with indium. The walls of the box are made out of oxygen free high conductivity (OFHC) copper, whereas the flange and lid are made out of the mechanically harder copper alloy Elmedur X. OFHC copper was chosen for its high thermal conductivity assuring fast cooling and its better purity in terms of magnetic contaminations with respect to standard copper. Elmedur X is a copper alloy with 0.8% zirconium and 0.8% chromium [Thy09], with almost the same thermal conductivity as copper and without ferromagnetic alloys. It was chosen for all parts that hold threads, since the threads in Elmedur will not wear out so easily as in OFHC copper. All copper parts of the box are hard-soldered or welded.

The inside of the box will be pumped down to about 10^{-6} mbar through a 3/8 inch tube soft-soldered into the backside, to reduce air freezing out on the electronics. After pumping, the tube will be sealed by cold welding with the so-called pinch-off technique. Here the end of the tube is pinched off using special tongs, which exert a high pressure on a small surface area. This pressure presses the opposite walls of the tube together, so that the outermost parts of the metal layers interweave and by this are welded together. This process is feasible for all soft, ductile metals. Due to the length of the tube, multiple reopening and pumping of the box without exchanging the tube is possible by cutting off the closed edge. The wall thickness of the box is 2.5 mm, to ensure stability in the pumping process.

The top of the U-shaped housing features four 25 pin sub-D feedthroughs from Ceramaseal to lead the electric signals from and to the trap through the box. The feedthroughs are UHV-tight and have gold-plated stainless steel pins in a glassceramic insulator. The insulator is housed in a stainless steel body, which is weldable. Since it is not possible to weld stainless steel and copper, the stainless steel body of the feedthroughs was copper-plated and then soft-soldered into the box. Hard-soldering was not possible since the feedthroughs would break from thermal stress at the temperatures involved.

The flange has two round notches to leave space for the resonators of the

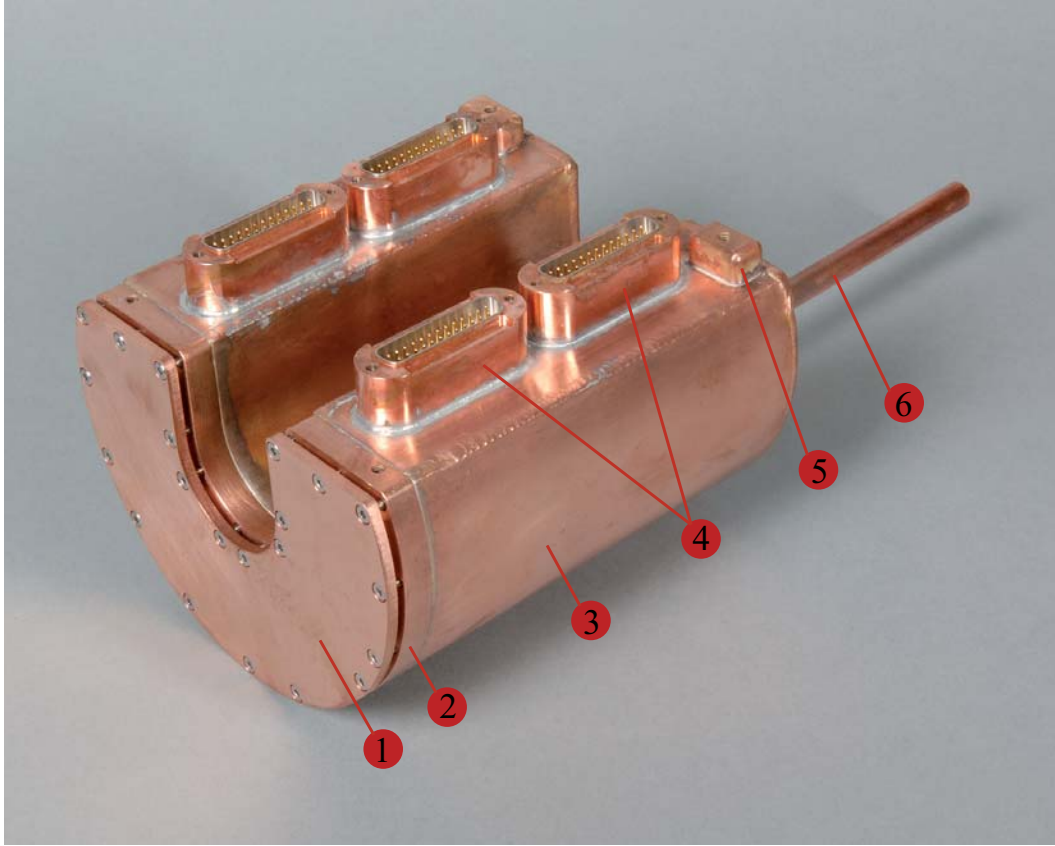


Figure 3.3: The electronics box. The box houses the RLC circuits, preamplifiers and filters next to the trap. It consists of a removable lid (1), a flange (2), the housing (3) and feedthroughs (4). The tube at the back (6) is for pumping the box, while the threads (5) are for the connection to the trap rail system.

axial and cyclotron detection coils. These are screwed to printed circuit boards, which also feature the cryogenic preamplifier (see figure 3.8). Due to the cryogenic environment there should not be any degradation of the trap vacuum by outgassing from the few parts that were soft-soldered. A first vacuum test with a rubber sealing in the flange showed, that all welded and soldered connections are tight up to 10^{-6} mbar.

3.3.2 The coils

The inductivity of a cylindrical coil is given approximately by:

$$L = N^2 \cdot \frac{\mu_0 \mu_r A}{l} \quad (3.9)$$

with N being the number of windings, A the cross sectional area, l the length of the coil, μ_0 the magnetic field constant and μ_r the magnetic permeability of the core material.

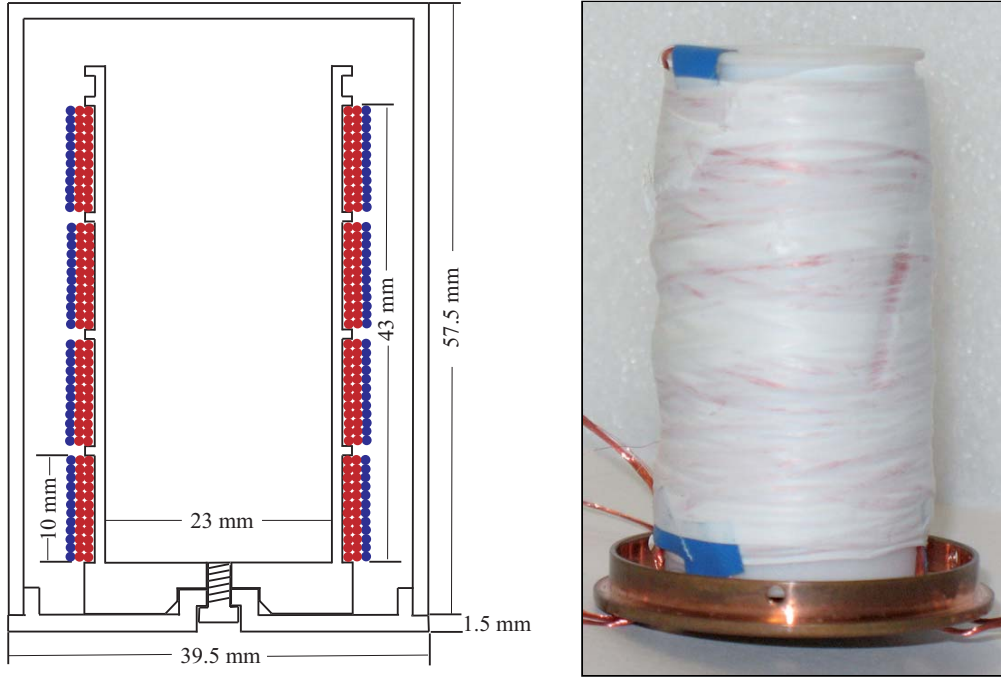


Figure 3.4: The axial frequency coil. On the left a drawing of the coil and the resonator is shown. Red is the primary coil, blue is the secondary coil. The right side shows a photograph of the coil.

The quality factor of a resonant circuit is given as in equation 3.4, but can also be given depending on the inductivity L and the capacitance C :

$$Q = 2\pi f_0 \frac{L}{R_s} = \frac{1}{R_s} \sqrt{\frac{L}{C}} \quad (3.10)$$

with R_s being the ohmic resistance of the coils wire and the dielectric losses in the capacitor and the core medium. To get a high Q -factor a large L and a small C and R are advantageous. This means, that the parasitic capacitances between the coil's windings and between coil and resonator should be held as low as possible. As mentioned in section 3.2.2, the real part of the coil's impedance, which causes the resistive cooling of the trapped ions, depends linearly on the Q -factor.

The standard way to build a high- Q coil is to use a helical resonator. This is a single-layer coil in a conducting shield called resonator, which concentrates the electromagnetic field of the coil inside a defined volume. The optimal design - in terms of Q -factor - of a helical resonator can be found in [Mac59]. It is only valid for single-layer coils with a copper conductor. In our case, the resonator has a second advantage: It shields the coil from picking up noise or its own amplified signal from the connections inside the box.

For each detection RLC circuit a dedicated coil was wound. The notch in the flange for the **axial frequency coil** resonator is 40 mm in diameter. The

resonator is made from OFHC copper with an outer diameter of 39.5 mm and a wall thickness of 1.5 mm at an overall length of 59 mm. The resonator is evacuated through the holes, which lead the signal wires out. The optimal coil would have a diameter of about 20 mm and a length of about 40 mm. We made the coil body from Teflon (PTFE), which has a relative permeability μ_r of 0.953. To reach a resonance frequency of about 420 kHz 560 windings would be necessary, requiring a wire with a diameter of 35 μm . This is not easily possible to wind. Therefore a multilayer coil was designed in different approaches with wire thicknesses of 0.25 and 0.1 mm. Different body structures were used on which the coils were wound, one with a single 40 mm long chamber and another with four separated 10 mm long chambers. Both were tested with chaotic winding as well as regular winding. The four chambers and the chaotic winding reduce the parasitic capacitances. However, no unloaded room temperature Q-factors larger than 100 could be reached with the 20 mm diameter coils (560 windings). Therefore the number of windings was reduced by enlarging the diameter. A test with the almost maximum possible coil diameter of 32 mm showed a strong degradation of the Q-factor due to the parasitic capacitance introduced by the resonator. Finally, a diameter of 23 mm was chosen. Here the quality degradation is comparably small, but still the shielding introduces a shift of the resonant frequency in the order of 20%. A final version was built with the parameters seen in figure 3.4. This coil was wound with a 50×0.04 mm diameter stranded wire, which gave - in terms of wire type - the best results concerning Q-factor.

Within the optimizing process of the design of the 440 kHz coil, the quality factor of the coil alone and with the resonator was determined by a simple transmission-type measurement. In this case the secondary coil was used as incoupling loop and the signal on the primary coil was measured across the capacitor with an oscilloscope. The final axial frequency coil was made as a result of those empirical tests. The coil has now 400 primary windings and directly on top 80 secondary windings. Parasitic capacitances lead to a frequency shift, that causes a big deviation from the nominal value of required windings.

The winding of the **cyclotron frequency coil** (35 MHz) was straightforward. The only parameter changed under the tests was the kind of wire used. Best results were found with a silver-plated copper wire with a diameter of 1 mm. The silver plating reduces the skin effect. The Teflon core is 35 mm long with an outer diameter of 14 mm. A 1 mm deep and 1 mm wide thread with a pitch of 2 mm was cut into the teflon core. This thread holds the wire. The 35 MHz coil has 6 primary and 3 secondary windings. The resonator is 41.5 mm long with an outer diameter of 27.5 mm and 1.5 mm wall thickness (see figure 3.5).

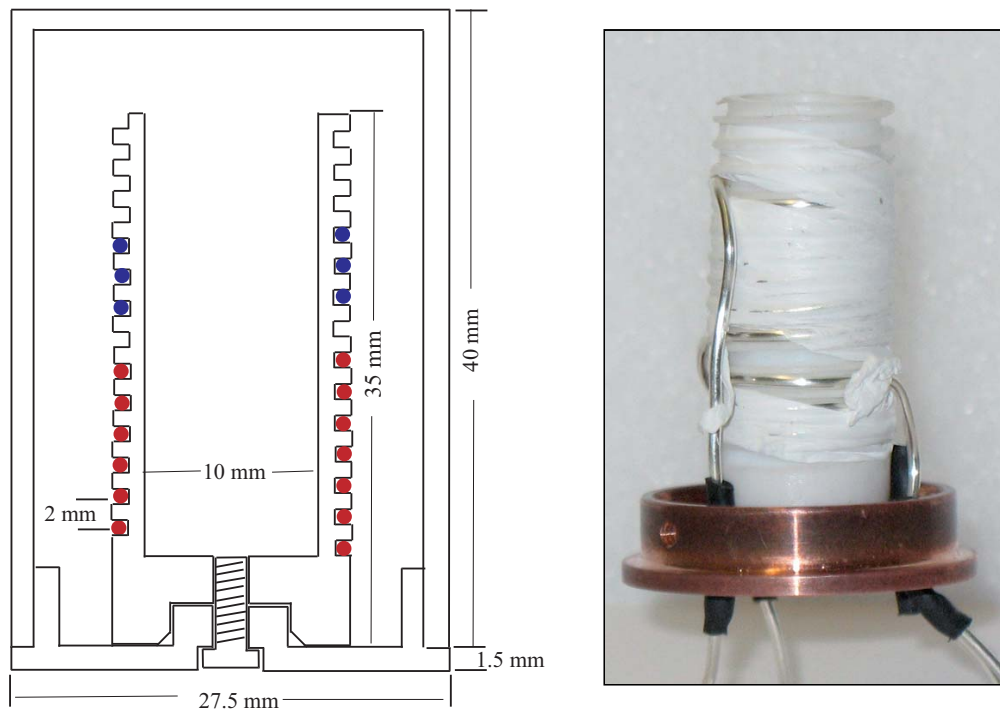


Figure 3.5: The cyclotron frequency coil. On the left a drawing of the coil and the resonator is shown. Red is the primary coil, blue is the secondary coil. The right side shows a photograph of the coil.

Q-measurement procedure

Two sets of Q-factor measurements were done for both coils: The coil without and with resonator, both at room temperature and at 77 K, in a liquid nitrogen (LN_2) bath. Stable temperature conditions were reached when the liquid nitrogen had filled the resonator completely. For both coils the parasitic capacitances of the trap electrodes and the connecting wires were simulated using a 47 pF foil capacitor (the low Q-factor of a ceramic one would destroy the measurement). Since the techniques used were different for the axial frequency and the cyclotron frequency coil, the measurements are described separately. Both set-ups are shown in figure 3.6.

The axial frequency coil:

After deciding for the design shown in figure 3.4, the transmission-type measurement set-up shown in figure 3.6 on the top was used. The important figure for HITRAP is the quality factor with the coil connected to the cryogenic amplifier (see section 3.3.3), thus the complete set-up was tested. A comparison between the Q-factor with and without amplifier at room temperature showed, that the unloaded Q-factor was a factor 1.4 lower than the loaded. This is due to the power dissipated in the amplifier, which introduces a parallel ohmic resistance to the system.

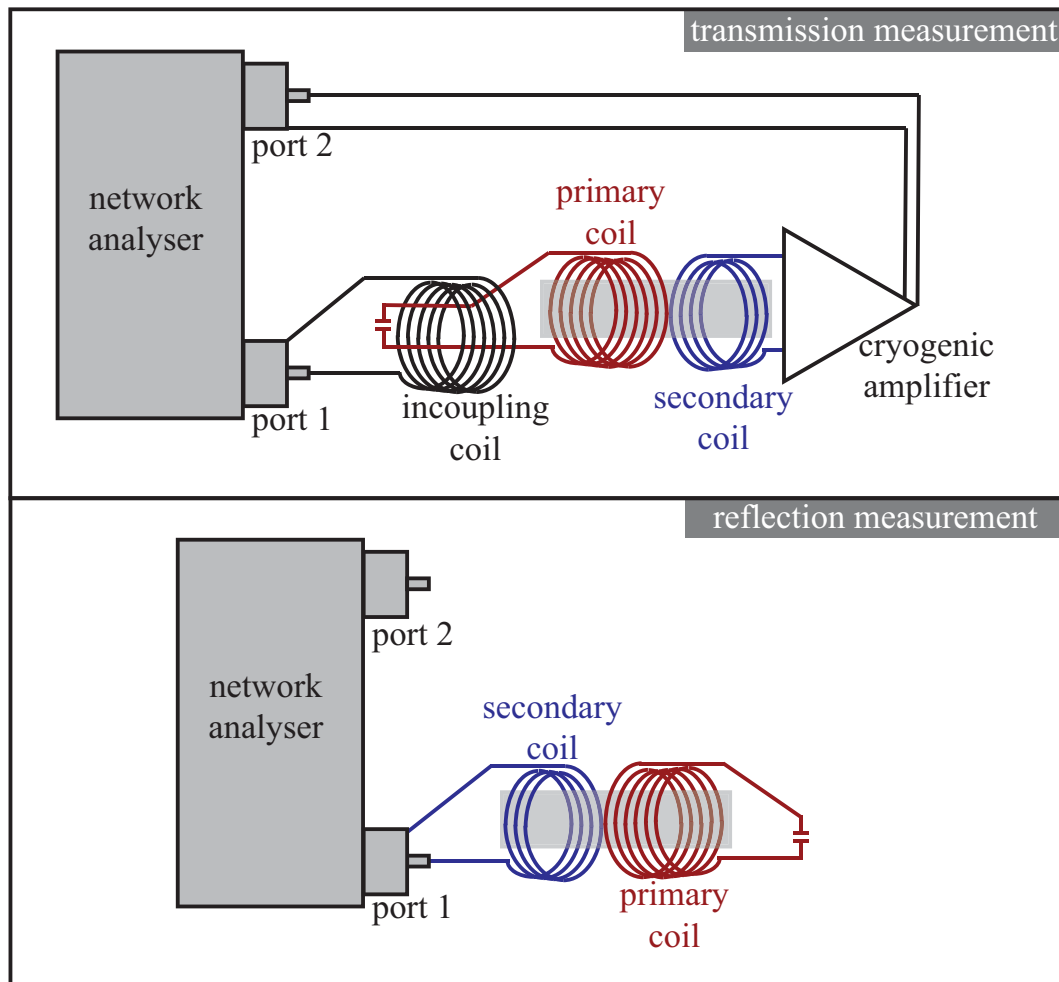


Figure 3.6: Q-measurement set-up.

Top: the transmission-type measurement for the axial frequency coil is shown. The signal from the network analyser output (port 1) is coupled inductively to the primary coil of the resonant circuit. The trap is simulated by the capacitor (47 pF). The secondary winding is connected to the amplifier and the output of the signal is measured by the network analyser (port 2). Below the reflection-type measurement is shown. Here the secondary coil is directly coupled to the output (the resonant circuit is connected in series). The reflection coefficient is measured. The shaded area represents the coil body.

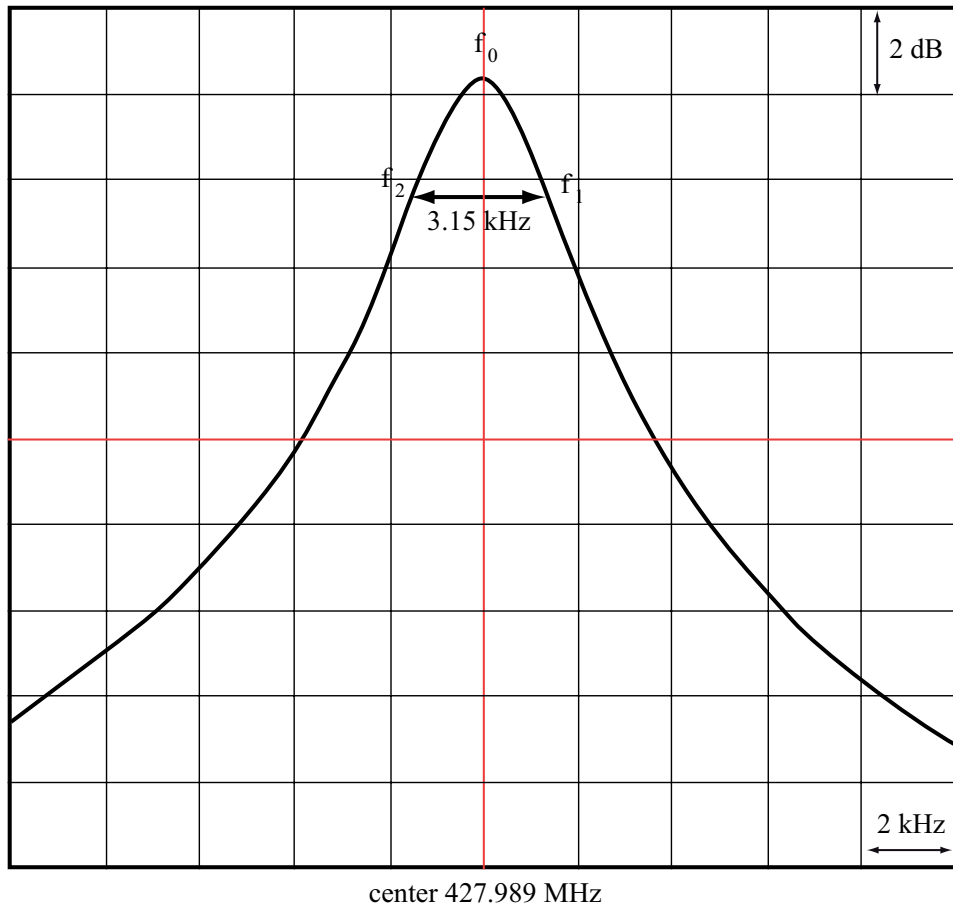


Figure 3.7: Example for a resonance for the transmission-type Q-measurement. The points used for the Q-measurement are shown.

For the measurement of the complete set-up we used an incoupling coil around the wire connecting the capacitor with the primary coil. This ensures a weak inductive coupling, which represents the ions in the trap quite well. The weak coupling also renders the influence of the network analyser negligible (for this influence and the coupling coefficient κ , see the explanation of the reflection-type measurement). As in the real set-up the signal (from the ions) is coupled to the primary coil. The secondary coil couples inductively to this and gives the signal to the cryogenic preamplifier. The amplified signal is read and processed by the network analyser, in our case an Agilent E8753. The Q-factor is determined by the width of the resonance at 3 dB (see equation 3.4 and figure 3.7). The final results are shown in table 3.1.

The mounting of the resonator has two effects: First, the field is concentrated within the resonator, leading to an upward shift of the resonance frequency - in this case nearly 100 kHz - and a higher Q-factor. Second, the parasitic capacitances between resonator and coil degrade the quality factor,

Table 3.1: Q-factors from the measurement of the 440 kHz coil. Shown are the resonance frequencies, the peak widths at 3 dB and the resulting Q-factors for the measurement with and without resonator at 300 K and 77 K. All measurements were taken with the coil connected to the powered cryogenic amplifier board.

	300 K		77 K	
	w/o resonator	w/ resonator	w/o resonator	w/ resonator
f_{res} [kHz]	366.4 ± 0.1	462.8 ± 0.1	344.4 ± 0.1	427.8 ± 0.1
Δf_{3dB} [kHz]	2.80 ± 0.04	6.60 ± 0.04	1.83 ± 0.04	3.15 ± 0.04
Q-factor	130.6 ± 1.9	86.7 ± 0.5	188.6 ± 4.2	135.8 ± 1.9

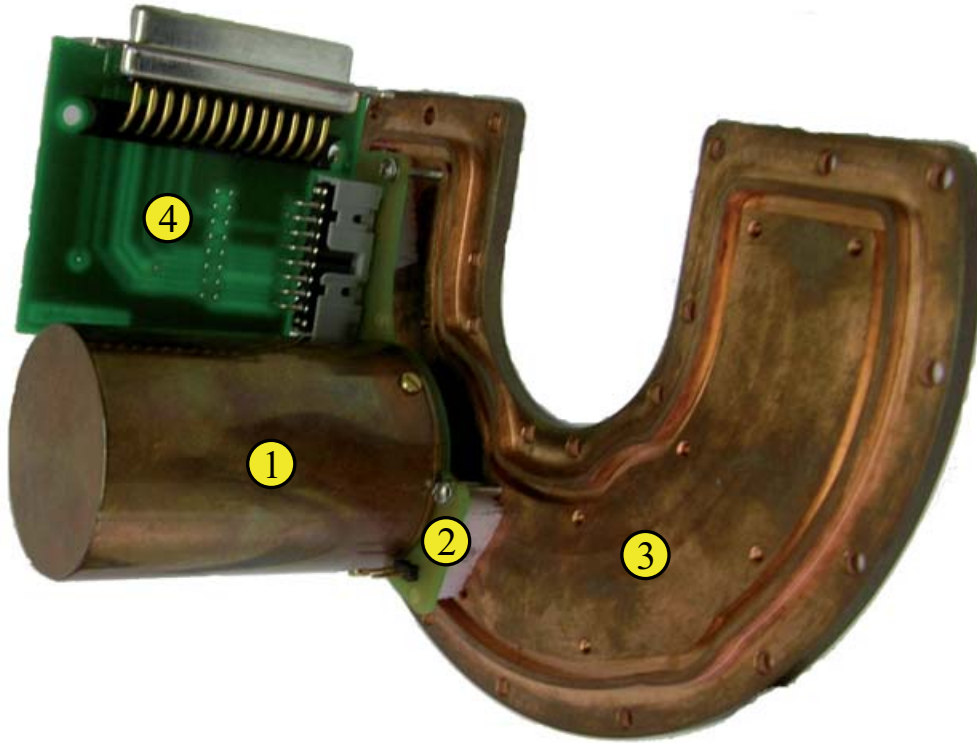


Figure 3.8: Mechanical set-up of the 440 kHz coil inside of the electronics box. The coil inside of the resonator (1) is mounted to the amplifier (2), which is mounted to the lid of the electronics box (3). The connection to the feedthroughs is done via a special printed circuit board (4).

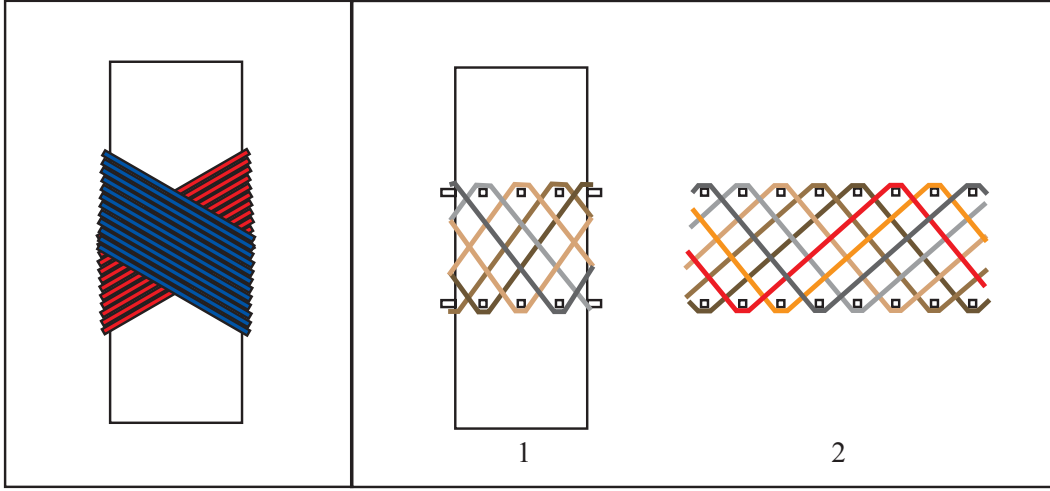


Figure 3.9: Cross- and basket-winding technique for coils.

Left: the cross-winding technique. The different layers (shown in red and blue) have only a small area where they actually overlap. This reduces the parasitic capacitances between them. Right: the basket-winding technique in view on the coil (1) and in flat projection (2). Just one layer is shown. The colours indicate the different windings. Other layers would be on top of this layer. The parasitic capacitances are reduced due to the spacing between the single wires.

which leads in our case to a net loss in Q -factor of about $1/3$. It is questionable if the resonator is really necessary, but a pickup of the amplified signal within the electronics box is quite possible. The resonator would shield against this effect. This should be investigated in situ.

For the system at 77 K we expected a slight increase in resonance frequency compared to 300 K, since the coils geometry shrinks. We observed a decrease by a factor of 0.93. This is caused by the LN_2 , which has a dielectric constant ϵ_r of 1.4 and introduces therefore a capacitive load to the system. Furthermore, we expected the quality factor to improve with cooling since the resistance of the copper is reduced. This reduction is due to the reduction of RF-losses, which contribute most to the Q -factors degradation. The RF-losses decrease with the square root of the conductivity, which rises by a factor of 100 going from room temperature to 4 K [Ulm09]. For an unloaded resonant circuit at 77 K we would expect a 7 times higher Q -factor compared to the room temperature value. This does not hold for the measured set-up, where the resonance circuit is loaded by the input impedance of the amplifier. We obtain an increase of the Q -factor of about 1.5 for both cases, with and without shielding.

For the realistic case, the cold set-up with resonator, we obtain a Q -factor of about 136. This is much lower than 800 as foreseen in the phase when HITRAP was designed. The low Q -factor is due to high parasitic capacitances within the coil and between coil and resonator. Still we expect a further rise of the Q -factor when cooling down to 4 K.

There are two possibilities to gain a higher Q-factor for the 440 kHz coil. Either the coil is made not from copper but from niobium-titanium, which is superconducting at 4 K. The other way would be to employ either cross- or basket-winding techniques. A sketch of both techniques is found in figure 3.9. A coil wound with one of the two techniques will be shorter but thicker and its inner diameter lower than that of the other coils. This might reduce the influence of the resonator. In a first test, a coil was produced with basket-windings in two chambers with 200 windings in the lower and 160 windings in the upper chamber. On top of the windings in the second chamber a secondary coil with 40 windings was wound. Its resonance frequency was at 563 kHz without and at 694 kHz with the resonator. The quality factors were 152 and 105, respectively. This first test showed no improvement concerning the influence of the resonator. Nevertheless, the Q-factor measured was significantly higher than the one of the standard coil design (without amplifier), which was 92 and 63 respectively. Since the resonance frequency of the basket winding coil is still too high, more windings have to be added. This might increase the parasitic capacitances and therefore degrade the Q-factor, so that the improvement in Q-factor by using this winding technique might be small.

The cyclotron frequency coil:

For the 35 MHz coil a reflection-type measurement commonly used in microwave technique was used as described in [Kaj99]. Here the secondary coil of the resonant circuit is directly connected to the network analyser (see figure 3.6) and the reflection coefficient of the primary coil is measured. Due to the input impedance of the network analyser, we measure the loaded Q (Q_L) in this set-up.

The unloaded Q (Q_0) was derived using the following equation

$$Q_0 = Q_L(1 + \kappa) \quad (3.11)$$

where κ is the coupling coefficient, which is the ratio of power dissipated in the external circuit (the network analyser and the secondary coil) to the power dissipated in the resonator. κ can be measured together with Q_L in one measurement, if the Smith-chart representation of the data is chosen (see figure 3.10). In this diagram the reflection coefficient describes a perfect circle as a function of the frequency. We identify three points on this circle: the center frequency f_0 , and the two geometrical 45° points (f_1 and f_2) in respect to the center frequency. These are the frequencies where the voltage drop is 0.707 of the maximum drop (see figure 3.10). The two 45° points are equal to the 3 dB points, so that Q_L becomes

$$Q_L = \frac{f_0}{f_1 - f_2} \quad (3.12)$$

The coupling coefficient κ is determined by first measuring the diameter d of

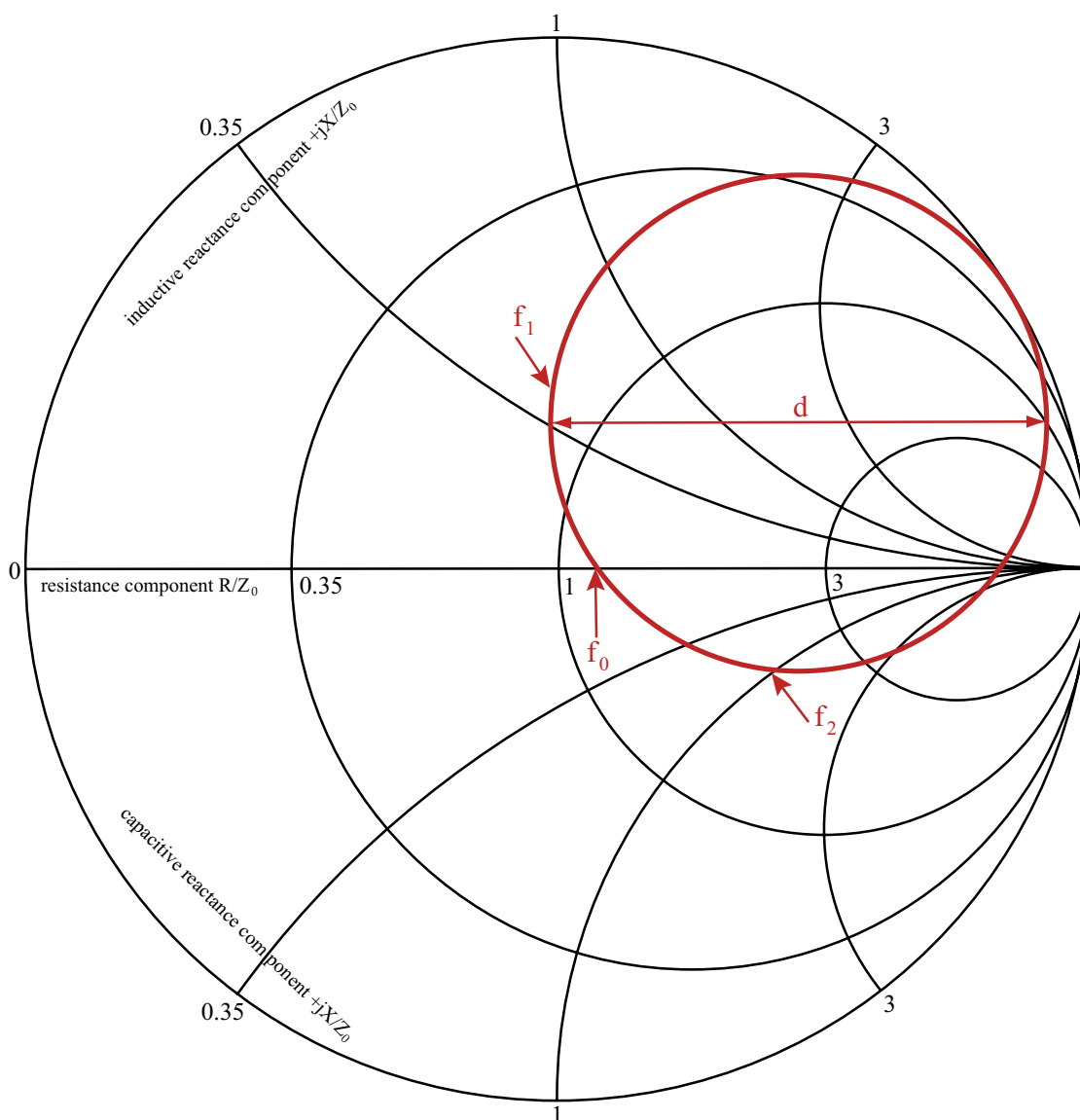


Figure 3.10: Reflection-type measurement in the Smith-chart.

The Smith-chart is a two-dimensional plot in the complex reflection coefficient plane, which is usually scaled in normalised impedance. The circumferential scaling is in wavelengths and degrees, where the degrees correspond to the angle of the voltage reflection coefficient at this point. For our measurement we identify three points on the reflection coefficient circle (in red) on the Smith-chart: f_0 , the resonance frequency and the two 45° points f_1 and f_2 , which correspond to the 3 dB points. The coupling coefficient κ is calculated from the diameter of the circle.

Table 3.2: Q-factors from the measurement of the 35 MHz coil. Shown are the resonant frequencies f_0 , the 45° widths $f_2 - f_1$, the loaded Q (Q_L), the diameter ratio d, the coupling coefficient κ and the unloaded Q (Q_0).

	300 K		77 K	
	w/o resonator	w/ resonator	w/o resonator	w/ resonator
f_0 [kHz]	38844±0.02	41147±0.02	36562±0.02	37094±0.02
$f_1 - f_2$ [kHz]	194.8±0.4	247.8±0.4	88.9±0.4	221.9±0.3
Q_L	199.4±0.4	247.8±0.6	411.4±1.9	167.2±0.3
d	1.32±0.02	0.94±0.01	1.35±0.02	1.65±0.02
κ	1.96±0.03	0.89±0.01	2.09±0.03	4.67±0.06
Q_0	590±9	469±7	1272±22	947±14

the reflection coefficient circle. If the circle has a diameter of 1, the coupling is critical. A smaller diameter means weaker coupling and a larger means overcritical coupling. κ is defined as:

$$\kappa = \frac{1}{\frac{2}{d} - 1} \quad (3.13)$$

The results of the measurement are summarized in table 3.2.

At room temperature we find for the 35 MHz coil unloaded Q-factors of 590 and 469 without and with resonator, respectively. The unloaded quality-factor rises to around 1272 without and 947 with resonator in liquid nitrogen, which is less than theoretically expected rise by a factor of 7. This is due to the capacitive load, which is introduced by the liquid nitrogen bath. The capacitive load also shifts the frequency to lower values; about 0.9 times with resonator and 0.94 times without resonator. The shift is stronger with resonator since the field concentration results in a higher capacitive load. Therefore the frequency shift in the opposite direction introduced by the resonator is much lower at 77 K as compared to 300 K.

At room temperature the coupling is reduced by the resonator. Cooling enhances the coupling due to the higher electric conductivity. This leads to an overall coupling enhancement introduced by the resonator at 77 K.

For both coils the final frequency tuning has to be done in situ. A first step would be a test with the complete trap and wiring, since the parasitic capacities introduced by the trap and the wiring might deviate from 47 pF. Then the frequency shift at 4 K must be determined, so that some windings can be taken off or added to reach the nominal value. In case of the axial frequency coil, this is not too critical, since the resonance frequency depends strongly on the trap potential and can therefore be tuned. It should nevertheless not

exceed 440 kHz. The cyclotron frequency coil must be tuned carefully to a final frequency of 35.6 MHz. Furthermore one has to mention, that a degrading of the Q-factor by the solenoid's magnetic field cannot be excluded [Ket06].

3.3.3 Cryogenic preamplifier

Standard amplifiers are not suitable for cryogenic environments. Therefore a special transistor amplifier was built, which is a slightly modified version of the design of the cryogenic preamplifier for the FT-ICR detection at SHIP-TRAP [Ket06]. We used the CF739 n-channel dual gate GaAs transistors from Infineon with a low input capacitance of 0.95 pF [Sie08]. The input capacitance also adds to the parasitic capacitances degrading the parallel resistance of the resonant circuit. The resistors are thin film resistors from Susumu and the capacitors are WIMA FKP2. Although none of these is marked as cryo-compatible, experience shows, that they work at 4 K and survive repeated cooling cycles [Sta08].

By designing the amplifier, we also have to consider that electronic parts - like transistors - will heat up when in use. This heat load can be dissipated by a good thermal connection between the electronics or the parts themselves and the cold environment. Therefore the common ground of the amplifier is connected to the electronics box via the screws holding the printed circuit board in place. Nevertheless, the final ion temperature might be somewhat higher than 4 K.

A schematic of the amplifier for the axial frequency signal is shown in figure 3.11. One end of the coil is coupled capacitively to the amplification stage at TP1, the other is AC-wise grounded at TP2. The amplification stage consists of 3 parallel transistors whose amplification is thereby added. The amplification stage and the buffer stage are coupled by a 33 pF capacitor. The capacitive coupling is commonly used to block DC voltages from one stage, which might influence the operating point of the next stage. Nevertheless this capacitor restricts also the bandwidth of the amplifier, so that the same design cannot be used for the 35 MHz signal, although the transistors are designed for frequencies up to 2 GHz. At least this capacitor has to be exchanged and the complete layout of the printed board has to be reworked to meet the standards of MHz-frequency electronics. Since it is not yet clear, if a preamplifier for the cyclotron motion really is needed, this has not been done yet. All voltage supply lines are low-pass filtered.

The cryogenic preamplifier was tested at room temperature. The sine signal from a signal generator was coupled directly to the input (without the coil), and the input and output voltages were measured with an oscilloscope. First a measurement of the dependence of the amplification on both gate voltages was done. Then the amplification versus the frequency was measured. The results are shown in table 3.3 and figures 3.12 and 3.13.

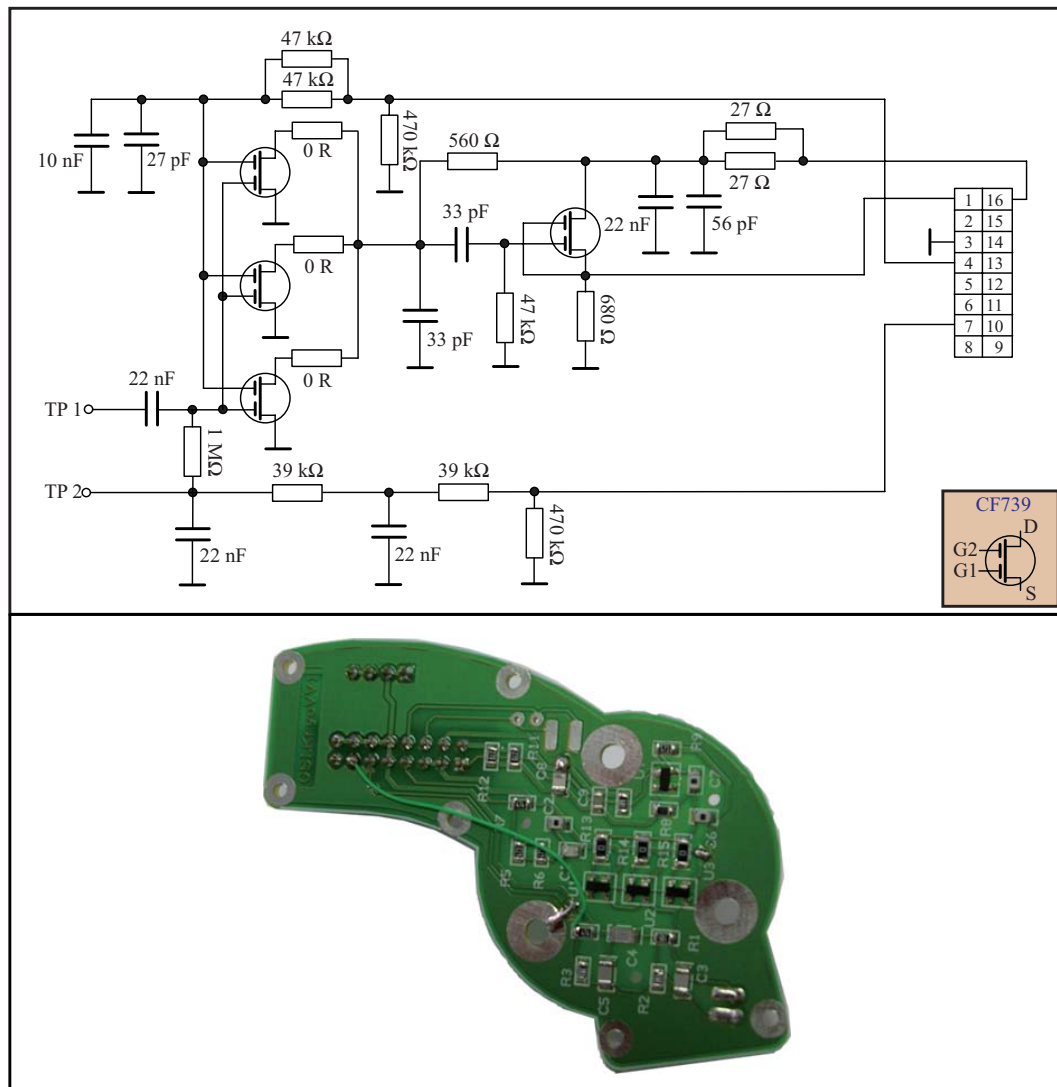


Figure 3.11: The cryogenic preamplifier.

On top a schematic of the amplifier is shown. The amplification stage is shown on the left side, consisting of 3 parallel n-channel dual gate transistors (Infineon C739). The coil is connected to TP1 and TP2. The buffer stage consisting of one CF739 transistor is on the right side. All voltage supply lines are low-pass filtered to reduce noise, the 470 kΩ resistors ground the system if no voltage is applied. Below: a photograph of the amplifier.

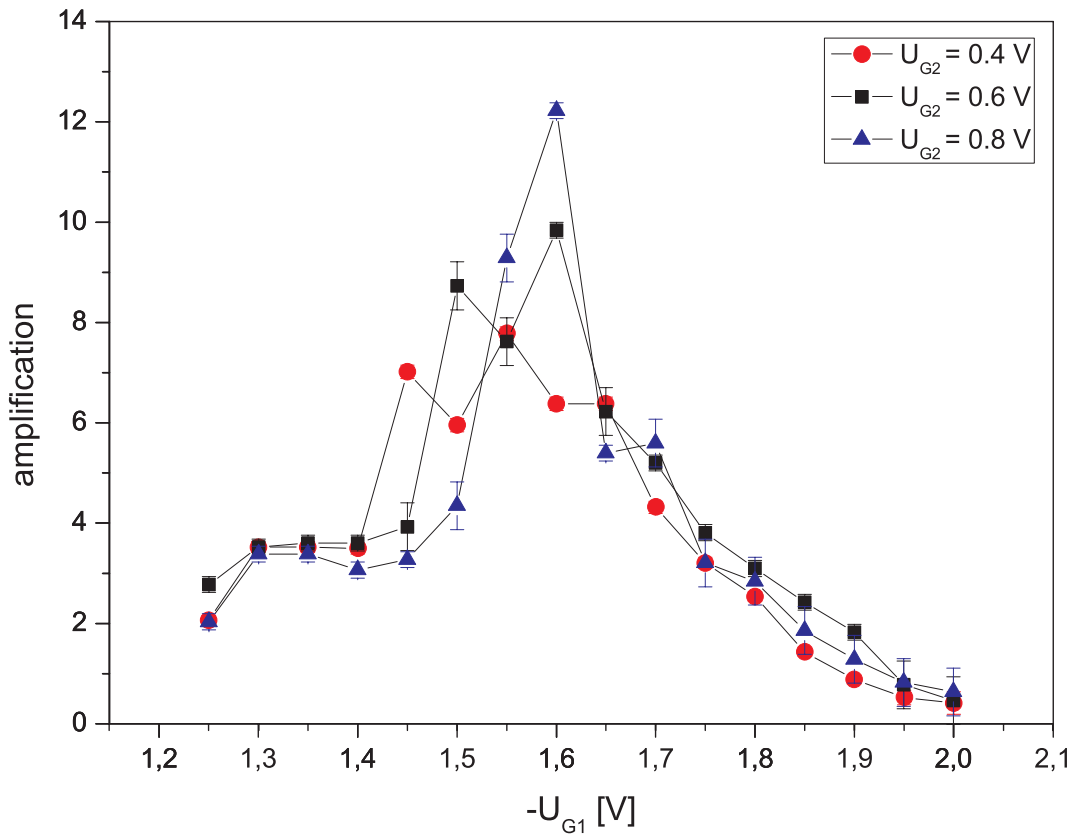


Figure 3.12: Amplification versus gate 1 voltage for different gate 2 voltages at 400 kHz. Drain voltage is 3.9 ± 0.05 V. The scattering at the maximum amplification comes from a quite noisy signal, which might be the result of overmodulation.

We find a good amplification for the following setting: drain voltage at 3.9 V, gate 1 at -1.65 V and gate 2 at 0.6 V. The signal at this setting shows low noise and an amplification factor of about 6. The scattering of the data around the amplification maximum can be explained by overmodulation. The amplifier acts as a band-pass filter with a lower cut-off frequency of about 90 kHz and an upper at about 8 MHz. The optimal bias voltage settings and the amplification factor might shift a bit by cooling the system down to 4 K, but this has to be studied in situ. A test at 77 K showed no shifts.

3.3.4 Filters

The DC power supply lines to the electrodes might also feed some AC noise to the electrodes. This noise can arise from the power supply itself or can be picked up by the DC supply lines - especially at the feedthroughs, where shielding of the detection signal coming from the trap is weak. Therefore a low-pass filter was designed, which still enables the fast switching (within 1 μ s) of the electrodes.

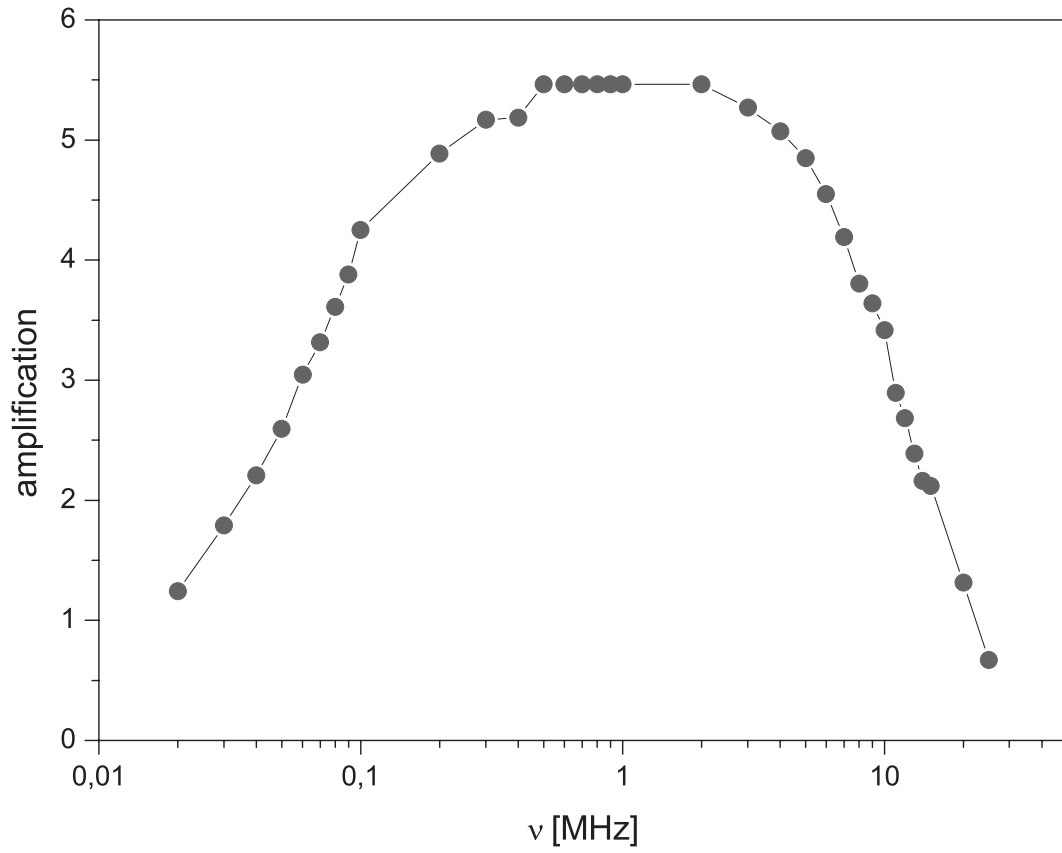


Figure 3.13: Amplification versus frequency. The bias voltages are 3.90 ± 0.05 V at drain, -1.65 ± 0.05 V at gate 1 and 0.60 ± 0.01 V at gate 2. The amplifier is a band-pass filter with a lower cut-off frequency of about 90 kHz and an upper cut-off at about 8 MHz. The plateau region shows an amplification of 5.24 ± 0.15 .

Table 3.3: Amplification of the cryogenic amplifier with respect to the gate bias voltages. All data were taken at room temperature and at an input signal frequency of 400 kHz. The drain voltage was fixed to 3.90 ± 0.05 V. The uncertainties for the gate voltages are 0.05 V for gate 1 and 0.01 V for gate 2. The last data set is the chosen setting for the frequency measurement.

$-U_{G1}$ [V]	U_{G2} [V]	amplification
1.95	0.60	0.78 ± 0.14
1.55	0.40	7.77 ± 0.14
1.60	0.60	9.84 ± 0.13
1.40	0.80	3.06 ± 0.11
1.80	0.50	3.06 ± 0.09
1.65	0.60	6.22 ± 0.13

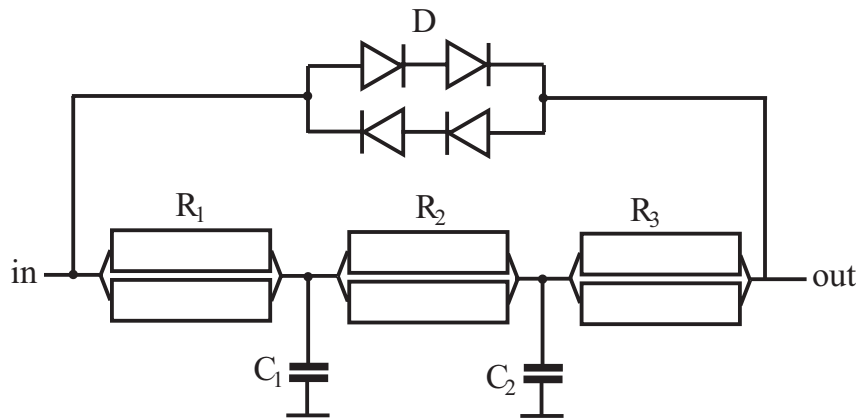


Figure 3.14: Schematic of the noise filter for the electrodes.

The filter consists of a passive second-order RC low-pass (bottom). The diodes (top) bridge the filter, so that fast switched DC signals get through without switching time distortion. Low-voltage noise signals do not pass the diodes. Double parts are a safety measure against breaking of one part.

For a passive low-pass first order RC filter with good filtering at 440 kHz, the time constant is too high to enable DC switching within 1 μ s. An active filter using operational amplifiers was impractical since the number of feedthroughs to the trap is restricted, and all lines to the electrodes should be filtered.

We decided to use a second-order passive RC filter, which is bridged by diodes [Sta07], as shown in figure 3.14. The second-order RC low-pass can be designed with a low cut-off frequency. As long as a noise signal is lower than the forward voltage of the diodes, it is blocked. A high-level, fast switched DC signal, will pass the diode bridge immediately. The rise/fall time distortion caused by the loading characteristics of the capacitances is therefore overcome.

The filter was simulated with the software PSpice and then built with the following characteristics: R_1 and $R_2 = 820 \Omega$; $R_3 = 1 \Omega$; C_1 and $C_2 = 3.9 \text{ nF}$. The bridge was made of GaAs Schottky diodes from IXYS (DGS 13-025CS), which have a forward voltage of 1.4 V and can stand 250 V [Ixy05]. The simulation and the test were in good agreement. Both gave a cut-off frequency of 36 kHz, and a signal damping of about 33 dB (factor 50) at 440 kHz (see figure 3.15).

The rise time characteristics were tested with a square wave signal. The result is shown in figure 3.16. The diodes in the bridge do not lengthen the rise-time of a signal. This is relevant for the fast switching of the electrode potentials, where pulses of a few hundred nanoseconds are foreseen, which should not be lengthened.

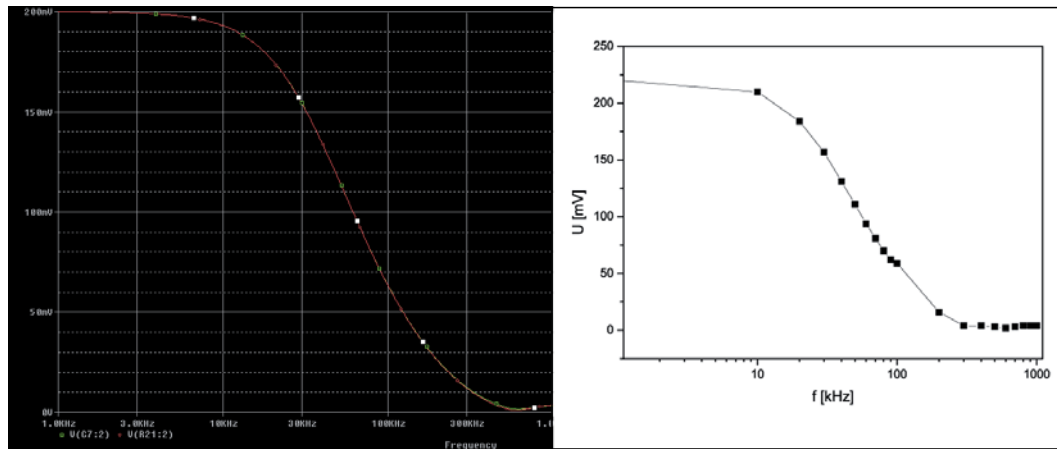


Figure 3.15: Transmission curve of the noise-filter: Comparison of simulation (left) and measurement (right). The simulation was done with P-Spice. Both are in good agreement.

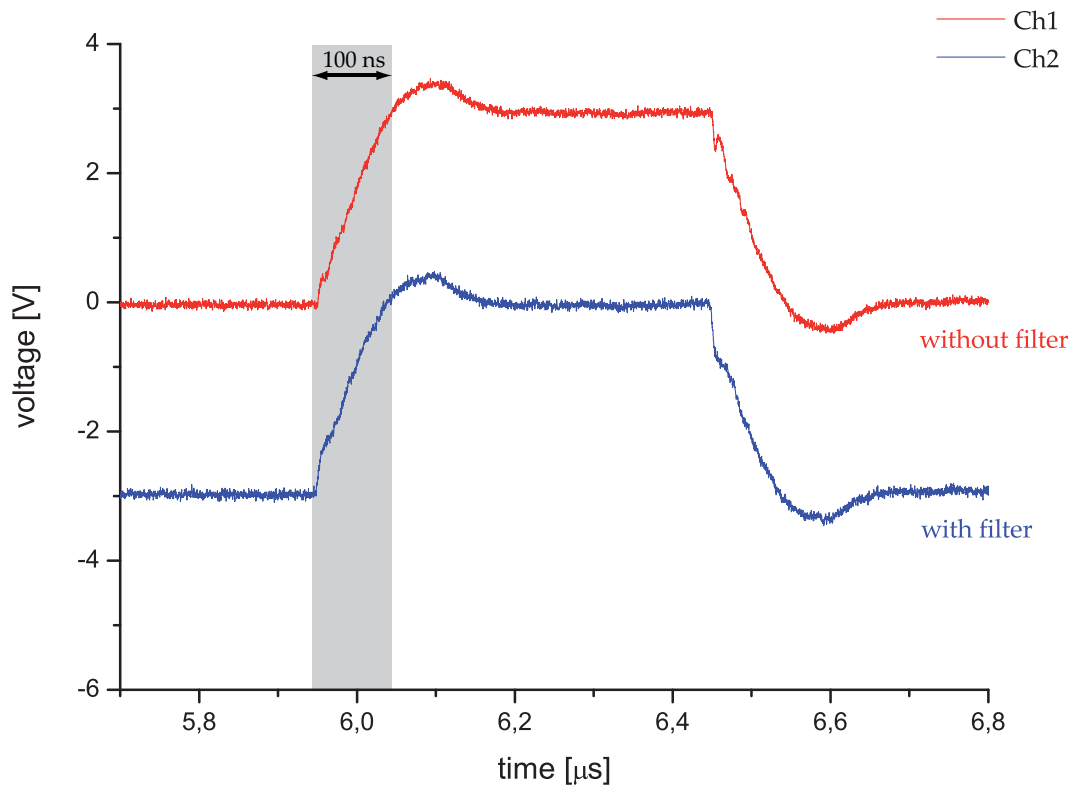


Figure 3.16: Rise time test of the noise-filter. The rise time for the signal without and with filter is identical.

3.4 Room temperature electronics

On the room temperature side, most Cooler Trap related electronics are situated in a high-voltage (HV) cage in the reinjection tunnel. The cage is on the same potential as the trap, i.e. 11 kV. The cage contains a PC, which controls the trapping potentials, the endcap switches and the readout electronics. Furthermore the power supplies for the detection preamplifiers are in the HV cage as well as the signal analyser and temperature sensor readout electronics. All parts are described in more detail in the following subsections.

3.4.1 Power supplies

There are three kinds of power supplies used for the Cooler Trap. First there are the GSI-HV-switches, which deliver the DC-voltage for the trap electrodes, by this shaping the trap potential. The switches are placed in 19 inch crates with six individual slide-in modules, each of which can give out a voltage in the range of ± 200 V. The potential is set and read out by a PC via a RS-485 interface. It is possible to have a ramping and a preprogrammed stepwise potential change. The switching time is $300 \text{ V}/\mu\text{s}$. The switches are triggered via a single-polar lemo input expecting a TTL-signal. This trigger signal is produced by the timing card (NI PCI-7811R FPGA - see chapter 4.4.2) situated in the trap control PC inside of the cage. Since this card is specified to give a TTL only until a maximum current of 10 mA, and we found the signal being distorted by overshooting for short pulse times (under 700 ns), a signal convertor with TTL output is introduced between the card and the power supplies. The card's output is connected to the SCB-68 connector box from National Instruments, which is connected to lemo outputs one for each channel.

The voltage supplies for the cryogenic preamplifier will also be in the cage. The linearly controlled supplies for a 19 inch rack have still to be ordered. The switches for the endcap-electrodes are not situated in the high-voltage cage. These are Behlke High voltage Transistor Switches (HTS 161-06-GSM). They are push-pull Mosfet switches with a rise time below 20 ns and a minimum pulse duration time of 200 ns. The HTS 161-06-GSM gives out a maximum voltage of 2×16 kV and a maximum current of 60 A [Beh09].

3.4.2 Detection electronics

The detection electronics will also be situated in the high-voltage cage. This is mainly the signal analyser from Stanford Research, model SR780, which carries out the Fast-Fourier-Transformation. It is remotely controlled by the *CS* control system (see chapter 4.2.2) via a GPIB interface. A class for the SR780 has been programmed but is not yet fully integrated into the *CS* control system. Since the analyzer has a bandwidth of only 102.4 kHz, a down-mixer and an additional signal generator will be necessary. These also have to be

ordered. Depending on the signal strength another amplifier (with power supplies) might be necessary.

Chapter 4

Cooler trap control system

This chapter gives an overview on the timing system for the HITRAP Cooler Trap and its role within the HITRAP control system. The solution uses a FPGA (Field Programmable Gate Array) card from National Instruments implemented in the existing *CS* control system, which was developed for other trap experiments like SHIPTRAP and ISOLTRAP. Since the existing timing solution could not match the requirements, a new timing module with improved performance was introduced. A new *CS*-module - a so-called class - for this card was programmed in LabVIEW 8.2 and the card is now running successfully at SHIPTRAP. More information can also be found in Appendix B.

4.1 Trap cycle

The main steps of the working cycle of the HITRAP Cooler trap are shown in Figure 3.1. As described in section 3.1.1, the timing device will control the following trapping steps. The time duration of each step is indicated in brackets.

1. Shape two nested traps, inject electrons, and close the entrance electrode (to the Low Energy Beam Transport) for them (about one millisecond). The exit electrode (to the Vertical Beam Transport) stays open.
2. Close the exit electrode for electrons (switching time 60 nanoseconds). Wait for the electrons to cool, at least a few 100 milliseconds. Await the extraction pulse from the ESR as trigger.
3. When triggered, switch the exit electrode to trapping potential for the ions and ground the entrance electrode (few microseconds).
4. Close the entrance electrode for ions (below 1 microsecond). Wait about 1.5 seconds for the electron cooling of the captured ions.
5. Pulse the trap electrodes to sweep the electrons from the trap (pulse duration at each electrode preferably 200 nanoseconds).

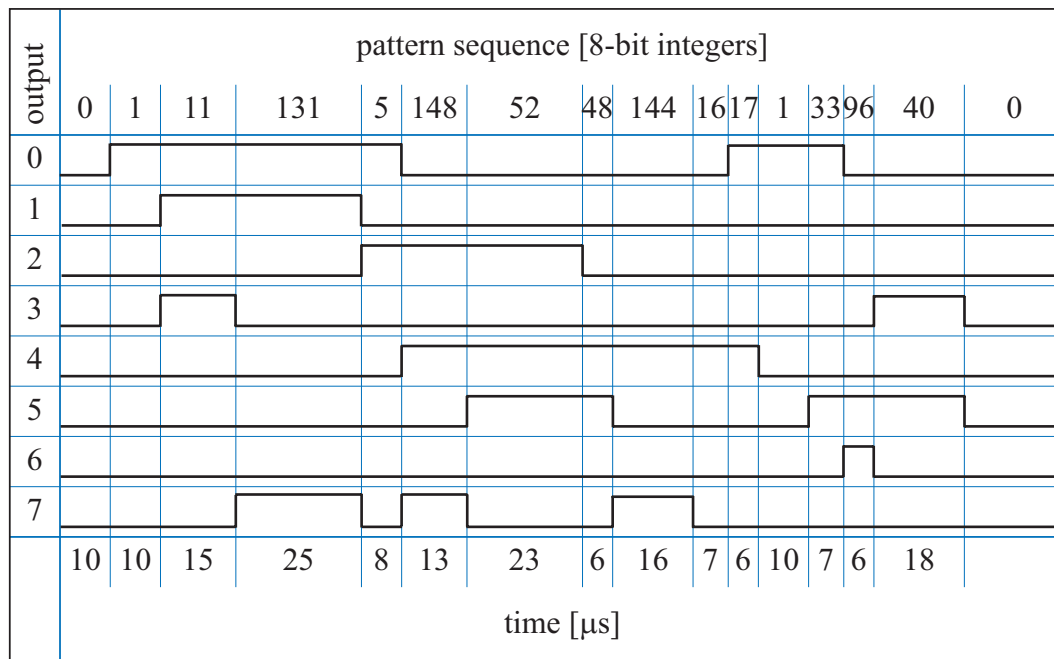


Figure 4.1: Example of a timing sequence. For each time step one output pattern, which is coded as an 8-bit integer number, is set. Each time at least one output changes its state, a new pattern is set.

6. Switch the outer electrodes such that the ions are accumulated in a central trap (few milliseconds).
7. Wait for the ions to resistively cool (some seconds to tens of seconds).
8. Shift the ions to the exit electrode (electrode switching time few milliseconds) and then
 - a) lower the exit electrode slowly (few milliseconds) or
 - b) lower the exit electrode fast and extract the ions from the trap (few microseconds).

The overall cycle time will be between 17 and 46 seconds, depending on the ESR cycle time. The ion trapping will be triggered by the ion ejection pulse from the ESR in step 3. Therefore the timing logic and the trapping logic are shifted.

One cycle is controlled by a so-called timing sequence. An example for such a timing sequence is shown in figure 4.1. The timing sequence consists of a sequence of time step informations and informations on the state of a number of outputs (the so-called pattern) for each time step. The number of state changes is equal to the number of times steps.

Most of the time steps in the working cycle have to be optimized - the efficiency of the ion trapping, for example, depends on the time when the entrance

electrode is closed. For this automatically controlled variation, the so-called scanning, of individual timing steps is required. In a scan the complete cycle runs a predefined number of times, while the parameter to be scanned is changed between each cycle by a predefined value.

4.2 Control system

4.2.1 Requirements on the control system

The HITRAP Cooler Trap control system should comply with the following requirements:

- It should be flexible against the exchange of single hardware components.
- The operation, maintenance and development should be fast to learn, since typically PhD students with a working period of 3 years will be responsible for these tasks.
- Timing and scanning must be possible.
- The system should be distributable on different PCs.
- It should fit in with the overall control system of the low energy part of HITRAP.

All these conditions are fulfilled by the existing control system *CS* described in the next section.

4.2.2 *CS*

The control system *CS* was originally developed to match the demands of medium-sized trap experiments as ISOLTRAP and SHIPTRAP [Bec04]. The control system is object-oriented, multi-threaded and event-driven. *CS* has a modular structure. Each instrument class (e.g. oscilloscopes from one manufacturer) is represented by a *CS* class. During run-time an instance (object) of a class is created for each individual instrument. Single hardware components can easily be exchanged by using an existing or creating a new class for the new component. The objects communicate via DIM (Distributed Information Management system. A network transparent inter-process communication layer for distributed and mixed systems [Gas00]) and one *CS*-system can be distributed on different PCs.

The individual *CS*-classes are programmed in LabVIEW 8.2, which is a graphical programming language by National Instruments. The code is contained in so-called virtual instruments (VIs) and the data flow is shown by wires. This allows for an easily readable coding. This and the modular structure give a new user an easy access to the program parts, so he or she can soon supervise and develop the *CS*-system of his/her experiment.

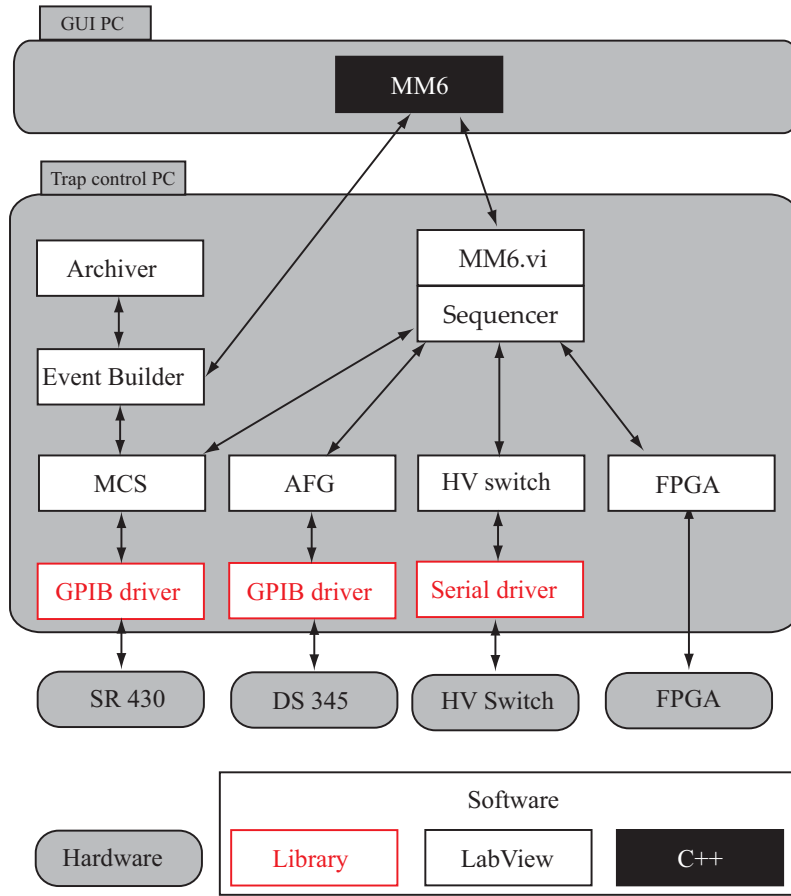


Figure 4.2: The trap control architecture. The MM6 user interface (GUI) runs on a dedicated PC. It talks to the corresponding CS object - MM6.vi - on the trap control PC. This object coordinates the communication to all hardware components, which again have their own objects. The event builder packs the data, which are then archived and displayed in the GUI.

4.2.3 Implementation of the *CS*-system

From the Low Energy Beam Transport on, the control of the HITRAP facility is taken over - from the GSI accelerator control system - by a dedicated HITRAP-*CS*. This is distributed on four PCs, with a subsystem dedicated to a special task running on each. On the *CS*-Core PC the data acquisition is controlled. A dedicated Hardware PC controls the power supplies for the ion optical elements as well as the steppermotors and the hardware related to the Cooler trap magnet (power supply, cryo compressor). A dedicated PC is set up for the user interaction (with graphical user interfaces - GUI's). Finally, one PC is dedicated to the trap control, which is situated in the high-voltage cage in the reinjection tunnel. This PC contains the timing card, the RS-485 card, which communicates with the GSI HV-switches providing the trapping voltages and a GPIB (General Purpose Interface Bus) card for the communication to the frequency generators and the signal analyzer taking the data.

The user controls the trap and the data acquisition via a graphical user interface programmed in C++, called MM6.cpp. This sends the settings and commands to a *CS*-object called MM6.vi, which distributes the values and commands to the objects of the single devices and initializes them, if necessary. The MM6.vi also reads back the status of the device objects and sequences the single scan steps, as well as publishes the status of the scan. The objects of the single devices contain the instrument driver and communicate with the hardware. They publish the data read from the instruments via DIM. The data are read by the so-called event builder, which packs them and publishes them again. The packed data are then archived and/or read by the GUI. The dependences are shown in figure 4.2.

4.3 The interface to the timing system

The MM6.vi sends two commands to the timing system, 'LoadData' and 'StartTG', and receives one, 'CycleFinished'. This is shown in figure 4.3 on the left side.

Together with the command 'LoadData', the MM6.vi sends all timing information data to the timing system. The timing information data consist of the building blocks for the timing pattern, the name of the timing system to be used as well as the scan parameters. When 'LoadData' was sent, the MM6.vi waits for the timing system to report the successful loading of the data.

'StartTG' causes the timing module to start a cycle.

When each cycle is finished, the timing system sends the MM6.vi the command 'CycleFinished'. Then the MM6.vi calls the data to be read and checks if all scan steps have been executed. If not, the next scan step is loaded and executed. When all scan steps are done, the MM6.vi awaits new user interaction.

4.4 The timing system

4.4.1 Requirements on the timing system

The set-up and the operation of the HITRAP Cooler Trap puts demanding constraints on the timing system.

- The complete cycle time of 17 to 46 seconds must be covered with a time resolution shorter than 100 nanoseconds.
- For the bunched ion ejection and the electron sweeping from the trap, the minimum pulse time is preferable around 200 ns, at least well below 500 ns (see also 3.2.2).

- The trap has 32 electrode elements (18 unsplit electrodes, two twofold and one eightfold radially split electrodes) that have to be time controlled. Additional channels are required for the endcaps and the detection electronics as well as the frequency generators. Thus the number of timing channels has to be at least about 40.
- Since the existing *CS*-system should be used to control the trap, the timing module has to be able to process the data coming from the MM6.vi. Preferable only the timing module class has to be exchanged within the *CS*.
- Since scanning should be possible, the pattern loading time should be fast.
- The termination of the pattern execution should be possible anytime, not only between scan steps.
- The timing system should have at least one trigger input.

4.4.2 The NI PCI-7811R FPGA card

The PCI-7811R FPGA card from National Instruments (NI) was introduced as a new timing module. We opted for the PCI (Peripheral Component Interconnect, a standard bus for the connection between periphery components and a processing unit) connector, to implement the card in the trap control PC and save therefore space in the high voltage cage.

A FPGA - Field Programmable Gate Array - is an integrated circuit, whose internal connections are not mechanically predefined, but can be accessed and modified programatically using a hardware description language. This gives the FPGA a wide variety of applications - from a simple counter to a highly complex microprocessor, or for instance a timing card. The hardware description language is VHDL (Very High Speed Integrated Circuit Hardware Description Language). The FPGA module in LabVIEW features a compiler, which translates the LabVIEW code to VHDL [NI09].

The 7811 R card has up to 160 digital channels distributed on 4 outputs (called connector) with 40 channels each. Each channel can be individually programmed as input or output. The card has an internal 40 MHz clock, which gives a timing resolution of 25 ns. The jitter on the FPGA clock is in the order of 100 ppm. The card has an 80kB internal memory and a FPGA with one million gates. The 7811R card is specified to give TTL signals with an amplitude of 3.3 V at 10 mA. At short pulse times - below 700 ns - we found the signal form to be distorted due to overshooting. To be independent from the actual load and to overcome the overshooting, we use a signal converter between the FPGA and the instrument to be triggered.

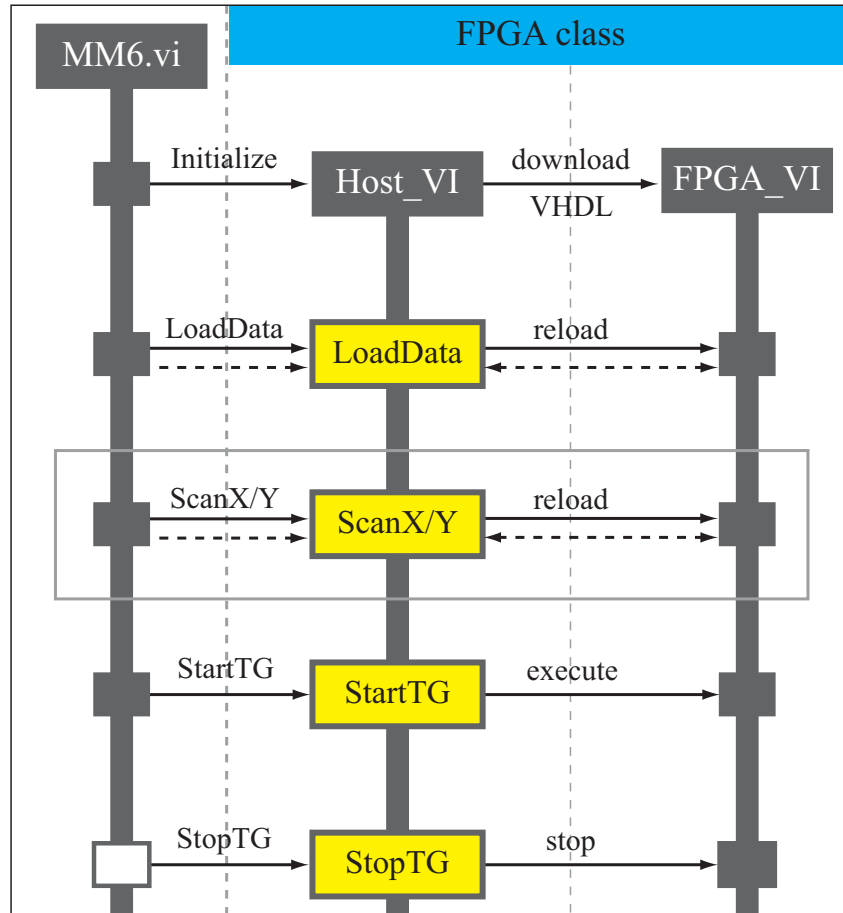


Figure 4.3: Sequence diagram of the FPGA_HI class. The commands (solid arrows) coming from the MM6.vi correspond to cases (lighter boxes) in the Host_VI, which send commands to the FPGA_VI. If necessary, data (dashed arrows) are also sent and received. Instead of the command 'LoadData' the command 'ScanX/Y' can be used at this position of the sequence (marked by a box). The empty rectangle in the MM6.vi line shows that the 'StopTG' command is not yet implemented.

4.4.3 Design of the timing system

The design of the timing system consists of two parts: The so-called Host_VI and the so-called FPGA_VI. The Host_VI is the communication layer between the MM6.vi and the FPGA_VI, which is the code being compiled to the FPGA target and therefore the implementation of the FPGA as timing device.

An overview on the sequence is shown in figure 4.3. When the Host_VI is called for the first time, the compiled code of the FPGA_VI is downloaded to the card. Then the Host_VI receives the information and commands provided by the MM6.vi and builds the final timing sequence, using the trigger and timing information. If a time step is to be scanned, the new scan value is implemented in the sequence at each step. The final timing sequence is in the right format to be handled by the FPGA_VI. The Host_VI loads the

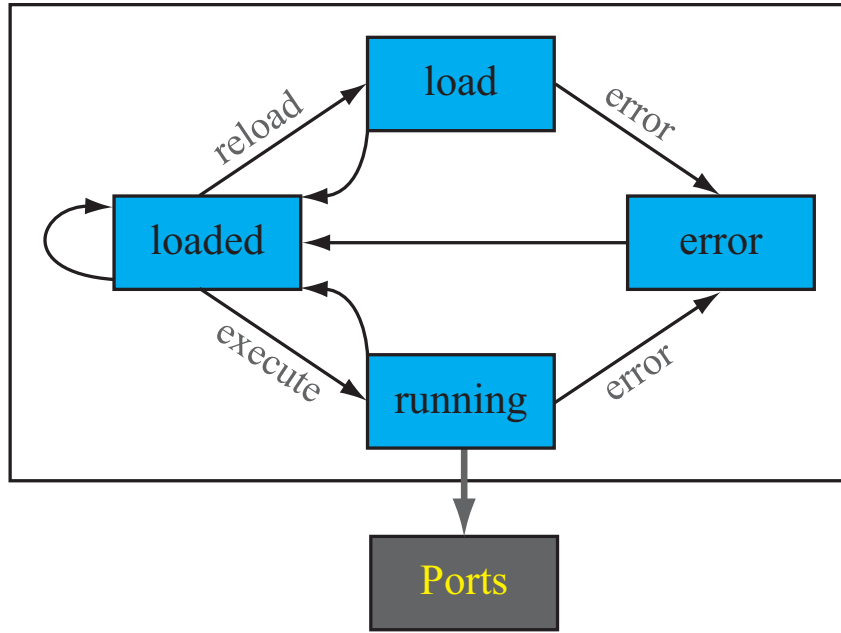


Figure 4.4: State diagram of the FPGA_VI state machine. The states and their end states are shown. When the state change is caused by a command or an error, this is explicitly stated. Otherwise the state change occurs, when the active state finishes its execution. Additionally shown are the output ports being set by the state *running*.

final sequence stepwise to the card, using a hand-shake mechanism. Furthermore the Host_VI sends the commands 'Execute' and 'Stop' to the FPGA_VI, causing the timing sequence to be executed and the execution to be stopped, respectively. When the execution of the sequence is stopped, the Host_VI sends the command 'CycleFinished' back to the MM6.vi. If an error occurs somewhere, this is also reported to the MM6.vi. The individual instances of this functionalities are implemented the FPGA class, which is the VI handling the commands coming from the MM6.vi.

The FPGA_VI is designed to consist of a state machine, based on an idea by Falk Ziegler of the University of Greifswald [Zie07]. A state diagram is shown in figure 4.4. It has four states: The state *loaded*, which is the default state, waits for a command from the Host_VI. The state *load*, which reads the timing pattern from the Host_VI to an internal memory and answers to the Host_VI, when finished. The state *running*, where the pattern execution takes place and finally the state *error*, which waits for the error message to be read by the Host_VI. The states *load* and *running* can only be reached from the state *loaded* and fall back to it, when they are finished. If an error occurs while loading or running the state machine automatically sets the state to *error*. From there it can only go back to the default state *loaded*.

4.4.4 Implementation and performance

Implementation of the Host_VI

The design for the Host_VI was implemented, as foreseen in the *CS* architecture, as cases in the ProcCases.vi of the FPGA class. Beside the default case, which only waits for a command, four cases were implemented. *LoadData*, *ScanX/Y*, *StartTG* and *StopTG*.

When *LoadData* is called, the timing and trigger information is sent. The number of triggers and the number of channels is checked and then the timing sequence is built accordingly (for more details on the actual sequence construction see Appendix B). The timing sequence consists of three arrays, one which holds the trigger information - i.e. number of triggers, trigger value, at which position within the sequence the execution should start -, the second contains the time step durations and the third is a two dimensional array of 32-bit integers, containing the channel states (pattern) for each time step. After the timing sequence is built, the Host_VI sends the FPGA_VI the command 'Load data'. As soon as the FPGA_VI is in the state *load*, the Host_VI sends the sequence by sending the first entries of the arrays, waiting for the FPGA_VI to process this data, before sending the next entries, until all elements are send or an error occurred.

In the case *ScanX/Y* the data entry for the value to be scanned is replaced by the data corresponding to the scan step, which is now to be executed. With this new timing information a timing sequence is built and then loaded to the FPGA_VI.

Once *StartTG* starts the execution by sending the command 'Execute' to the FPGA_VI, it is periodically checked if the FPGA_VI is still in the state *running*. As soon as the state *running* is finished, the command 'CycleFinished' is sent to the MM6.vi.

The case *StopTG* sends the command 'Stop' to the FPGA_VI and sets a global stop variable to true and sends 'CycleFinished' to the MM6.vi.

Implementation of the FPGA_VI

On the FPGA card memories and FIFOs are predefined to save the timing sequence information between loading and executing. The last timing sequence loaded stays in the memories until it is overwritten or the card is reinitialized. The channels are combined to ports, which hold 8 channels each and are controlled via an 8-bit integer, stating which channels are on. Each connector holds five ports. The fifth port at connector one is defined as trigger input, so that 255 different trigger states can be read (trigger state 0 means no trigger).

The state machine was implemented as a case structure, containing four cases, each representing a state. The state *loaded* is used as default state, since the first initialization is accompanied by the loading of the first timing sequence. If an error occurs while loading, the user is informed.

In the state *loaded* the state machine waits for a command. When the command is received, the according state is called.

If the state *load* is called, the elements of the timing sequence (pattern, time step and trigger information) received from the Host_VI are written to according internal memories. Since arrays consume too much space in terms of gates, a stepwise loading of the timing sequence, using a hand-shake mechanism was conceived. By this the length of the timing sequence is only limited by the bit depth of the memories. Every time one element has been processed, the FPGA_VI tells the Host_VI that the next data set can be sent. After the last element has been processed, the state machine falls back to *loaded* if no error occurred and to *error* otherwise.

The actual execution of the timing sequence takes place in the state *running*, which is called by the command 'Execute'. First the complete timing sequence is read from the memories to according FIFOs for faster execution. Then the trigger information is read out and the VI waits for the according trigger. Is the trigger received, the FIFOs are read out in a loop and the channels are set according to the pattern. The loop waits for the time defined in the time step, before executing again. After the execution of the timing sequence is finished, all channels are set back to zero and the state machine falls back to *loaded* if no error occurred and to *error* otherwise. Since the timing sequence is not erased from the memories, it can instantly be executed again, without reloading.

The state *error* is called if anywhere an error occurs. This state waits until the Host_VI has registered the error. A detailed description of the codes of the Host_VI and the FPGA_VI can be found in Appendix B.

Performance

Does the so implemented timing system comply with the constraints set in 4.4.1? There are no problems to be seen from the hardware side. The timing system was designed to fit into the CS, to communicate with the MM6.vi and to provide enough channels as well as a trigger input.

The timing pulses created by the system can have lengths between 350 ns and 107 s. The lower limit is given by the execution time of the pattern generating loop in the state *running* in the FPGA_VI. Pulse lengths shorter than 350 ns are not produced reliably. We are not in the preferable 200 ns regime,

but well enough below 500 ns. From 350 ns on, the time resolution is 25 ns. The upper limit is given by the 32-bit data format of the time information. This can be changed to 64-bit, if necessary, giving an upper time limit of about $5 \cdot 10^{11}$ s.

The loading time for a new pattern is well below one second, so that the scanning of individual channels is easily possible. The only constraints at the moment come from the MM6. A minor change has to be done at the LabVIEW side to enable the stopping of the pattern at any time within the execution. The number of channels is limited by the C++ GUI of the MM6, since there are only three different pattern inputs for 16 channels foreseen. The MM6 GUI will be restructured to match the grown needs of the experiments and the new timing system.

This timing solution using the 7811R card was tested and verified at SHIP-TRAP. It is now successfully used at SHIPTRAP and ISOLTRAP. At SHIP-TRAP the FPGA timing solution was used to test the timing of the newly installed Bradbury-Nielsen gate (see chapter 2.3.3) and to optimize the capture time for the purification and the measurement trap [Wer08]. The 7811R card is installed in the trap control PC and in the HITRAP Cooler trap *CS* and is ready for operation.

Chapter 5

On-line mass measurements at SHIPTRAP around $A = 96$

In March 2007 and in April 2008 two beamtimes were conducted at SHIPTRAP. Both were dedicated to the search for isomeric states in nuclides near the line of stability using quadrupolar excitation of the ions cyclotron motion. The octupolar excitation scheme, which should enhance the resolving power by an order of magnitude and the accuracy by a factor of two with respect to the quadrupolar excitation [Eli07a], was also studied in both beamtimes.

The quest for isomeric states has two motivations. On the one hand, they provide deep insight in the nuclear structure. On the other hand, to measure a ground state mass accurately, all isomeric states have to be resolved and correctly identified. Isomeric states are excited nuclear states with lifetimes between 1 ns and 10^{15} years (^{180m}Ta). This discriminates them from other excited nuclear states, whose lifetimes are well under 1 ns. Three kinds of isomeric configurations are known: the shape elongation, the spin-trap and the K-trap isomer (see figure 5.1).

Shape elongation isomers have a non-spherical nuclear shape at a local energy minimum. These isomeric states generally decay by fission, just in some cases a γ -decay to the ground state is also possible.

Spin trap isomers exist, when the decay path to the ground state is highly suppressed or forbidden by spin selection rules, i.e. a large nuclear spin change is required for the decay. For example, the isomeric state of ^{180}Ta has a nuclear spin $I = 9$, the ground state has $I = 1$, therefore the multipolarity λ of the decay photon has to be 8, which results in the long lifetime of this isomeric state. Spin trap isomers generally decay by γ emission or internal conversion. Only a few cases decay by α -particle or proton emission or β -decay. Spin trap isomers are generally found in the vicinity of nuclear shell closures.

K-trap isomers are axially symmetric, deformed nuclei. All known K-trap isomers are prolate. K-traps are usually found far from shell closures. Due

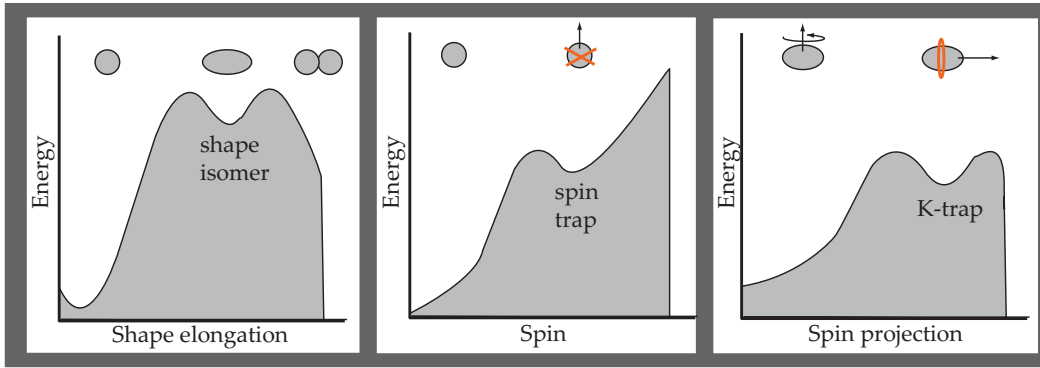


Figure 5.1: Isomeric state configurations as described in [Wal99].

The secondary energy minima are shown for the three isomeric configurations. Left the shape isomer, middle the spin trap and right the K-trap. The relevant nuclear shapes and the angular momentum vectors (arrows) are shown. The angular momentum for the spin trap and the K-trap comes from orbiting nucleons, indicated in red.

to the deformation the orientation of the spin vector with respect to the symmetry axis plays a role for the spin selection rules. The quantum number K describes the spin-projection on the symmetry axis with the selection rule $\lambda \geq \Delta K$. However, it is found that this selection rule is not strict [Wal99].

Spin traps and K-traps are described by superfluidity models (with nucleon pairing in analogy to the Cooper-pairs in superconductivity), where the pairing is partially quenched, for example by collective rotations. The mechanism is still not fully understood. These models predict isomeric states with uncertainties of about 200 keV [Wal99].

Isomers can gain extra stability by the suppression of fission or α -decay channels and can thereby have longer lifetimes than the ground state ($^{270}_{110}\text{Dy}$ for example). This is especially interesting at the borderlines of nuclear stability and the predicted island of stability in the regime of the superheavy elements. In hot stellar environments isomeric states can communicate with the ground states through thermal excitation, which can change the lifetimes of the nuclide, and therefore the paths of nuclear synthesis might be altered [Wal06].

Another benefit from measuring isomeric states far from stability is the insight into the structure of the so-called mirror nuclei (these are nuclei, where the neutron and proton numbers are interchanged) on the other side of the line of stability. So one can learn from the nuclear structure of proton-rich nuclei about the structure of the experimentally not or hardly accessible neutron-rich isotopes.

High-precision mass measurements of both, the ground and the isomeric state, can give an input to the models by providing excitation energies. Fur-

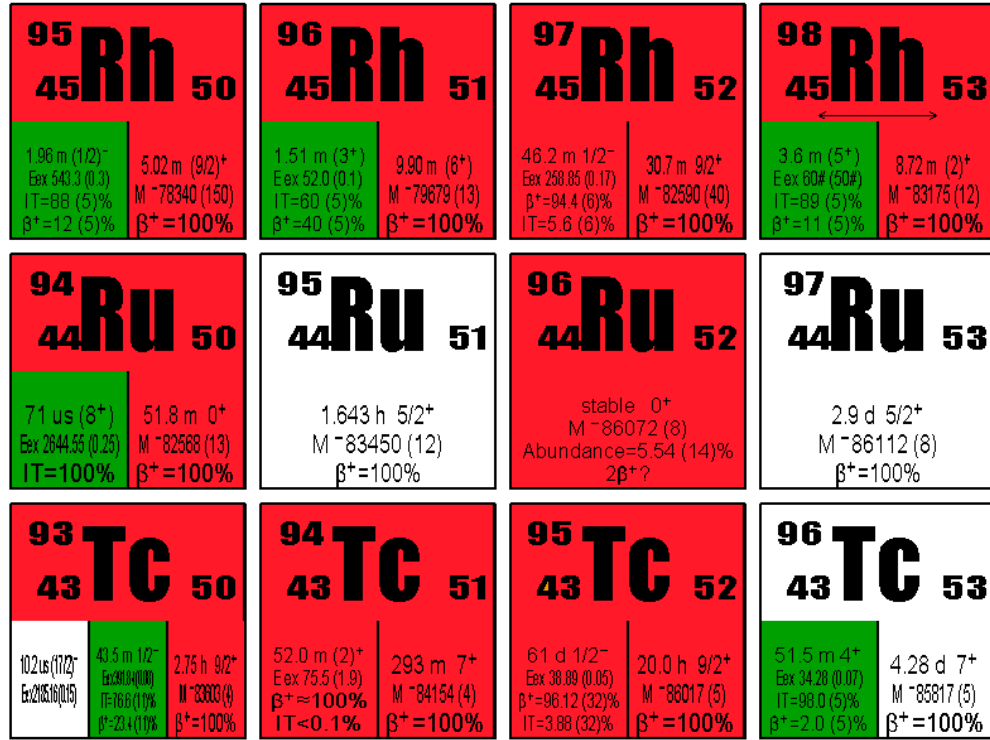


Figure 5.2: Nuclear chart displaying the nine measured isotopes.

thermore, to date just predicted, but not yet measured isomeric states near the proton drip-line might be found. Since the spin trap and K-trap isomers are produced mainly in fusion evaporation reactions [Wal06], SHIPTRAP might be suited to search for this kind of isomeric states. For example the isomeric states of ^{143}Dy and ^{147}Dy have already been investigated [Rau06].

In the following, the results of the beamtimes in March 2007 and April 2008 are discussed. The region of interest was close to the nuclear charge number $Z = 45$. It was tried to resolve the known isomeric states in this region to learn about their production in fusion evaporation reactions and to get an idea on the detectability of isomeric states farther away from stability. It was also the aim to learn more on the octupolar excitation in the Penning trap and to use it more routinely in investigations near the proton drip-line. The details of the mass measurements, the data analysis procedure and the data evaluation within the Atomic Mass Evaluation (AME) [Wap03] are presented. In the 2008 beamtime, the FPGA timing card (see chapter 4.4.2) was first used as timing generator in an online experiment, speeding up the parameter optimization. The multi-channel plate (with an efficiency of about 30%) was replaced by a channeltron detector with an efficiency close to 100%.

Table 5.1: Half-life $T_{1/2}$, spin and parity I^P of the measured nuclides as described in [Aud03a]. Uncertain spin and/or parity values are marked by brackets, the # indicates an excitation energy only estimated from systematic trends. E_{exc} is the excitation energy of the isomeric state. The shift in the cyclotron frequency in respect to the cyclotron frequency for the ground state mass is given in the last column.

Nuclide	$T_{1/2}$	I^P	E_{exc} [keV]	frequency shift [Hz]
^{93}Tc	2.75 h	$9/2^+$		
^{93m}Tc	43.5 m	$1/2^-$	391.84	-5.2
^{93n}Tc	10.2 μs	$(17/2)^-$	2185.16	-29.4
^{94}Tc	293 m	7^+		
^{94m}Tc	52 m	$(2)^+$	75.5	-1.0
^{95}Tc	20.0 h	$9/2^+$		
^{95m}Tc	61 d	$1/2^-$	38.89	-0.5
^{94}Ru	51.8 m	0^+		
^{94m}Ru	71 μs	(8^+)	2644.55	-34.6
^{96}Ru	stable	0^+		
^{95}Rh	5.02 m	$(9/2^+)$		
^{95m}Rh	1.96 m	$(1/2^-)$	543.3	-7.0
^{96}Rh	9.9 m	(6^+)		
^{96m}Rh	1.51 m	(3^+)	52.0	-0.7
^{97}Rh	30.7 m	$9/2^+$		
^{97m}Rh	46.2 m	$1/2^-$	258.85	-3.2
^{98}Rh	8.72 m	$(2)^+$		
^{98m}Rh	3.6 m	(5^+)	60#	-0.7

5.1 Experimental results

The beamtimes took place from March 12th to 20th 2007 and April, 11th to 14th 2008, respectively. In both beamtimes, the neutron-deficient isotopes around rhodium ^{97}Rh were produced by fusion evaporation reactions induced by a ^{12}C beam impinging on a 0.626 mg/cm² thick ^{92}Mo foil with an energy of 11.4 MeV/u. The molybdenum foil was enriched to 97.4% of ^{92}Mo . We measured nine isotopes near the valley of stability (see figure 5.2). Table 5.1 shows the relevant physical properties of the measured nuclides and their isomeric states as given in [Aud03a].

The radioactive ions coming from SHIP were stopped in the SHIPTRAP gas cell, accumulated in the buncher and then transferred to the purification trap. Here the first unambiguous identification of the nuclides is possible, since the devices in front of the trap at SHIPTRAP are not very mass-selective (see also chapter 2.3). Identification and separation was done by mass-selective buffer gas cooling with a resolution of $R = 50000$, sufficient to separate the

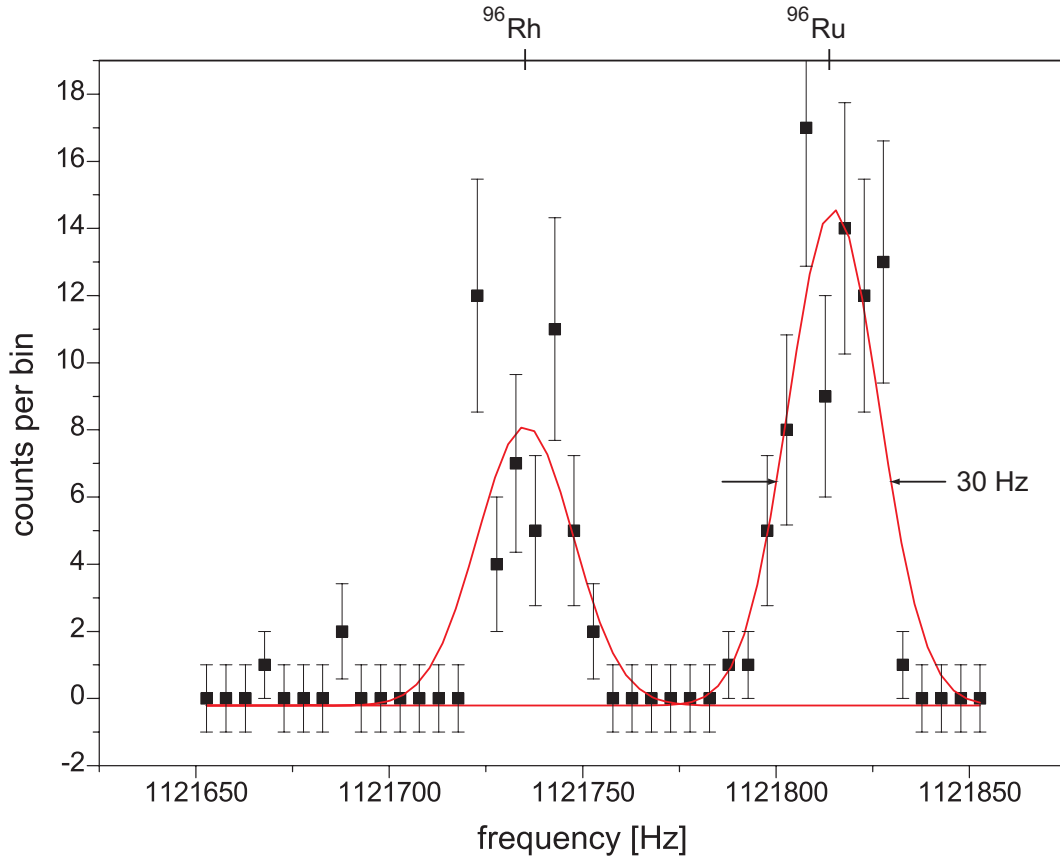


Figure 5.3: Cooling resonances in the purification trap for ions with mass $A = 96$. Ruthenium and rhodium are well separated at a resolution of 50000.

isobars at mass number 96 (see figure 5.3). The separation of ruthenium ^{96}Ru was especially important, since this is a stable isotope with a large production cross section.

The quadrupolar cyclotron excitation frequency was fixed to select, center and transfer only the nuclide of interest to the measurement trap. The cyclotron frequency of the ion is measured here using the TOF-ICR method (see chapter 2.3.4). In 2007 the maximum excitation time in the measurement trap was set to 900 ms, since the pressure was rather high with 10^{-6} mbar (measured at the drift-line), resulting in a strong damping. This led to a resolving power of about $6 \cdot 10^5$. In 2008 the pressure was lower, so that excitation times up to 2800 ms could be used, giving a factor three higher resolution. With this resolution the isomeric states of technetium ^{93}Tc , rhodium ^{95}Rh and ^{97}Rh should be clearly visible.

Table 5.2: Experimental results. The frequency ratio $r = \nu_{ref}/\nu_{ion}$ is given with its statistical and total uncertainty. Since no isomeric states could be resolved, the results, where an isomeric admixture could not be excluded are marked by index x. In all cases $^{85}\text{Rb}^+$ was used as reference. All measured ions were singly charged. The tables give the results obtained for the **2007** beamtime, the **2008** beamtime and for the evaluation using the data from both beamtimes as one data set (**All**). Here the x marks nuclides where at least in one beamtime the isomeric correction had to be done. In the 2008 data set the value for the octupolar excitation of ^{96}Rh is marked with index oct.

2007				
Nuclide	N_s	N_{ion}	Frequency ratio r (σ_{stat}) (σ_{tot})	(σ_{tot})/ r $\cdot 10^8$
^{93}Tc	3	2620	1.094197835(68)(84)	7.7
^{94x}Tc	4	3266	1.105967854(87)(100)	9.1
^{94}Ru	5	1722	1.105987956(369)(373)	33.7
^{96}Ru	4	1113	1.129497754(127)(137)	12.1
^{95}Rh	5	2276	1.117818602(387)(390)	34.9
^{96x}Rh	4	3367	1.129578441(282)(286)	25.3
^{97}Rh	9	7718	1.141319114(93)(106)	9.3
^{98x}Rh	2	891	1.153089051(69)(87)	7.5
2008				
Nuclide	N_s	N_{ion}	Frequency ratio r (σ_{stat}) (σ_{tot})	(σ_{tot})/ r $\cdot 10^8$
^{93}Tc	2	85	1.094197827(144)(153)	14.0
^{94}Tc	7	6497	1.105967849(76)(91)	8.2
^{95x}Tc	2	839	1.117721439(42)(66)	5.9
^{94}Ru	2	707	1.105987668(109)(120)	10.9
^{96}Ru	2	805	1.129497579(63)(81)	7.2
^{96x}Rh	20	9340	1.129578177(107)(119)	9.9
$^{96x}\text{Rh}_{oct}$	4	2278	1.129578014(187)(193)	17.1
^{97x}Rh	3	1138	1.141319261(136)(146)	12.7
^{98x}Rh	2	1440	1.153088803(33)(62)	5.4
All				
Nuclide	N_s	N_{ion}	Frequency ratio r (σ_{stat}) (σ_{tot})	(σ_{tot})/ r $\cdot 10^8$
^{93}Tc	5	2705	1.094197829(68)(84)	7.7
^{94x}Tc	11	9763	1.105967873(53)(73)	6.6
^{95x}Tc	2	839	1.117721439(42)(66)	5.9
^{94}Ru	7	2472	1.105987781(197)(203)	18.4
^{96}Ru	6	1918	1.129497600(45)(68)	6.0
^{95}Rh	5	2276	1.117818602(387)(390)	34.9
^{96x}Rh	29	15075	1.129578186(107)(119)	10.5
^{97x}Rh	12	8856	1.141319161(115)(126)	11.1
^{98x}Rh	4	2327	1.153088833(56)(76)	6.6

5.2 Data analysis procedure

The octupolar excitation scheme was used in 2007 only for the reference measurements with rubidium ^{85}Rb . It was found, that choosing the right amplitude for the octupolar excitation was impossible. This was partly due to electrical connection problems in the set-up, which also affected the standard quadrupolar excitation, but in much lesser effect. The full width half maximum (FWHM) of the resonances obtained with octupolar excitation were bigger than the ones with quadrupolar excitation. In the beamtime 2008 the octupolar excitation was tested with rhodium ^{96}Rh . Again it was not possible to find the right amplitude and get a better resolution from this excitation scheme. The FWHM was here about a factor two to three larger than with the quadrupolar excitation scheme. All other results in the 2008 beamtime were obtained using the quadrupolar excitation. It is not yet fully understood, why the octupolar excitation failed also in the 2008 beamtime. One possibility is, that not all internal connection problems were found and solved in between the beamtimes. That is further investigated now.

The analysis of the experimentally obtained frequency ratios follows the method used at ISOLTRAP [Kel03].

- First the theoretically expected line shape is fitted to the measured resonance. The cyclotron frequency, which is the center of the resonance, is one of the free parameters. This fit yields the cyclotron frequency and the statistical uncertainty σ_s . In case of the octupolar excitation a Gaussian curve was fitted.
- The cyclotron frequency can be shifted by contaminant ions present in the measurement trap simultaneously with the ion of interest (for example from isomers of the investigated nucleus). Whenever possible, a count rate class analysis was performed [Kel03]. This analysis usually shifts the frequency of the individual resonances slightly and increases the uncertainty by a factor of 2 to 3. When the count rate class analysis was not possible - for example because of low statistics - the uncertainty was increased manually. Usually an averaged factor, determined from the cases in which the analysis was successful, is used. This procedure worked well for the data from the 2007 beamtime. In the data from the 2008 beamtime yet, the averaged uncertainty increase was much lower than 2 for all nuclides where a count rate class analysis for some spectra (maximum 50% of the spectra of an individual nuclide) was possible. In the case of four nuclides (^{93}Tc , ^{95}Tc , ^{96}Ru and $^{96}\text{Rh}_{oct}$) no count rate class analysis was possible at all. We decided to increase the uncertainty in all spectra, where a count rate analysis was not possible, manually by a factor of 2.
- The cyclotron frequency of the reference ion rubidium ^{85}Rb was measured alternating to the measurement of the ion of interest. The reference frequency at the time of the measurement of the species of interest

was determined by a linear interpolation between the two adjacent values of the reference ions. The time interval between the reference ion measurements reaches from about 20 minutes to 5 hours.

- The frequency ratios ν_{ref}/ν_{ion} were calculated. An uncertainty arising from magnetic field drifts of $\sigma_B = 3 \cdot 10^{-9}/h$ [Rau06] was added quadratically to the uncertainty of the individual frequency ratios.
- All frequency ratios obtained for one nuclide were averaged. The internal uncertainty

$$\sigma_{in} = 1/\sqrt{\sum_i 1/\sigma_i^2} \quad (5.1)$$

and the outer uncertainty

$$\sigma_{out} = \sqrt{\frac{\sum_i ((r_i - \langle r \rangle)^2 / \sigma_i^2)}{(N-1) \sum_i 1/\sigma_i^2}} \quad (5.2)$$

were calculated and compared. Since in our cases the ratio of outer and inner uncertainty deviated strongly from 1, the larger of both uncertainties was taken.

- A relative, mass-dependent shift of $\epsilon_m = (1.1 \pm 1.7) \cdot 10^{-10}/u \cdot \Delta(m/q)$ was determined from cross-reference mass measurements with carbon clusters [Cha07]. $\Delta(m/q)$ is the mass-to-charge ratio difference between reference ion and the ion of interest. The averaged frequency ratio was corrected with ϵ_m and the uncertainty of ϵ_m was added quadratically to the total uncertainty of the frequency ratio.
- A relative residual systematic uncertainty of $4.5 \cdot 10^{-8}$ also gained from the cross-reference measurements [Cha07] was quadratically added to the total uncertainty of the frequency ratio. It comes from the reduced χ^2 of the mean frequency ratio for the carbon-cluster cross-reference measurements.

This procedure was first done for the data sets from both beamtimes individually. The frequency ratios obtained in both beamtimes were checked for consistency (see figure 5.4). The only major deviation was found for rhodium ^{98}Rh , where the ratios from 2007 and 2008 deviate by almost three standard deviations σ , which is still a good agreement. Then all data for an individual nuclide from both beamtimes were evaluated as a single data set. In case of rhodium ^{96}Rh the data obtained with octupolar excitation were also taken into the complete data set.

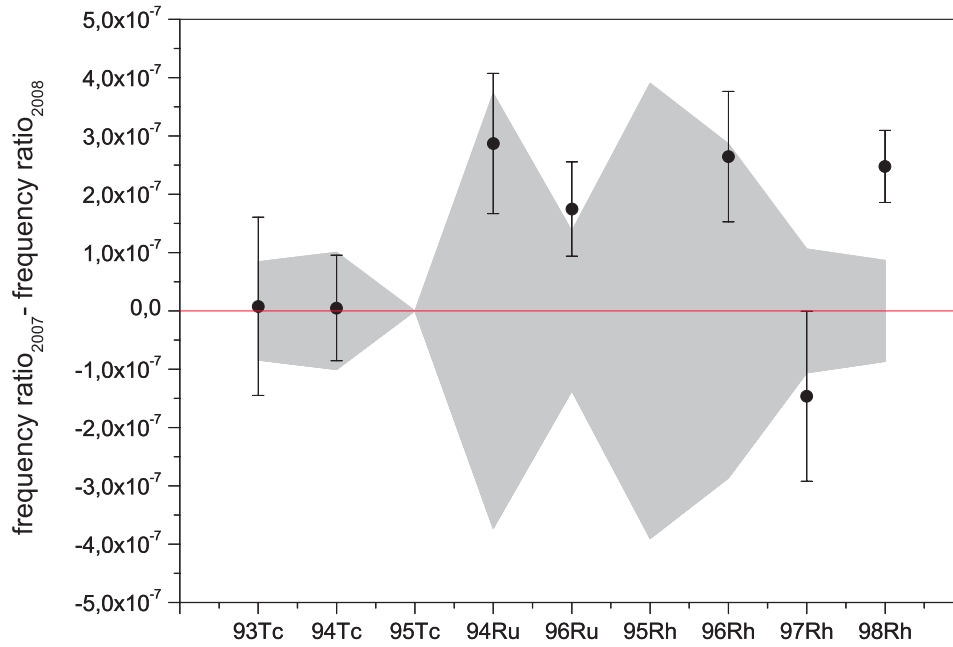


Figure 5.4: Comparison of the frequency ratios obtained in both beamtimes. The uncertainty envelope of the 2007 beamtime is shown as the shaded area, the data points are the difference between the ratios of 2007 and 2008, with the error bars from the 2008 measurement. The isotopes ^{95}Tc and ^{95}Rh were not measured in both beamtimes and are therefore not shown.

5.3 Data Evaluation and Atomic Mass Evaluation

From the frequency ratios obtained in this work (see table 5.2) atomic masses were calculated. These were compared to the Atomic Mass Evaluation (AME), which collects all available mass data from mass spectrometric and decay energy studies [Aud03b]. Wherever multiple input data for an atomic mass exist, an adjustment procedure using the least-squares method is used [Wap03]. We give the mass values as the mass excess

$$M = m - A \cdot u \quad (5.3)$$

with the atomic mass m , the mass number A and the atomic mass unit u .

Where necessary the data were corrected for admixtures of isomeric states as described in appendix B of [Wap03]. Knowing the excitation energy E_1 , one can deduce from the measured mass excess the corrected ground state mass excess by

$$M_0 = M_{exp} - R_{mI} E_1 \quad (5.4)$$

with R_{mI} being the mixing ratio of the isomeric state, and an uncertainty

$$\sigma_0 = \sqrt{\sigma_{exp}^2 + (R_{mI} \sigma_1)^2} \quad (5.5)$$

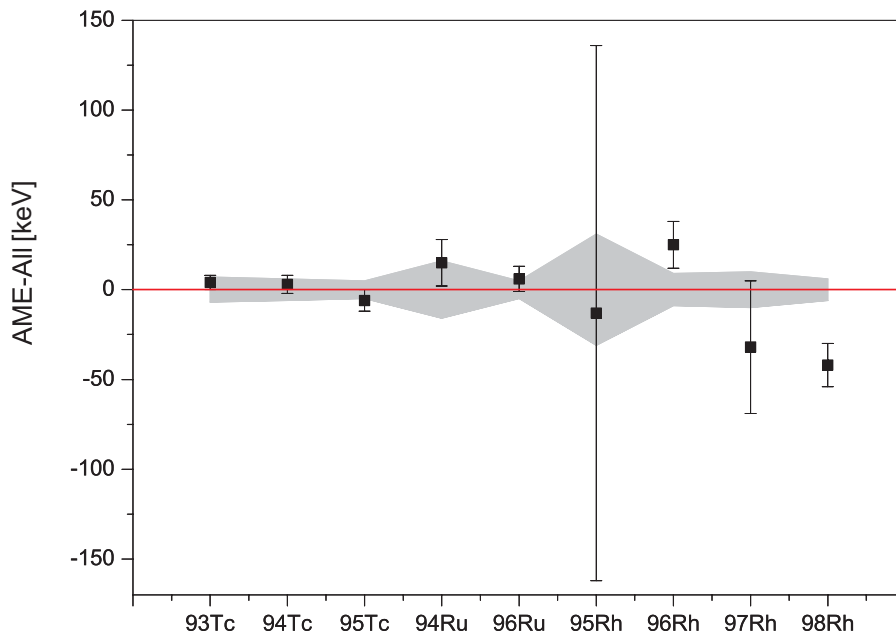


Figure 5.5: Mass results without isomeric correction. The data points are the deviation of the values given in the Atomic Mass Evaluation from the obtained results. The shaded area is the uncertainty envelope of the SHIPTRAP data, the error bars are the uncertainty of the AME data.

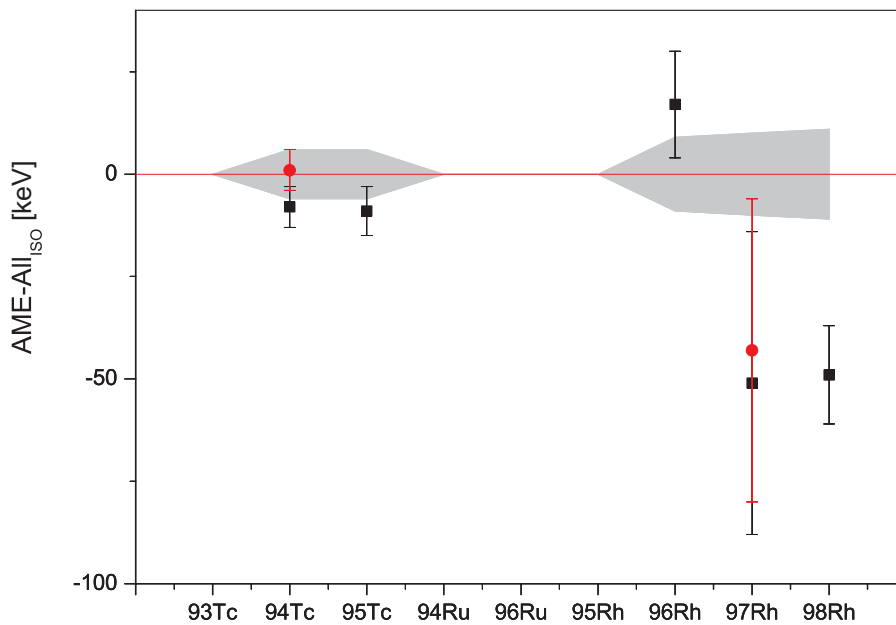


Figure 5.6: Mass results with isomeric correction. The black data points are the deviation of values from the Atomic Mass Evaluation from the obtained results including the isomeric correction. The shaded area is the uncertainty envelope of the SHIPTRAP data, the error bars are the uncertainty of the AME data. The red data points are an average of the data from both beamtimes, when the isomeric correction was necessary only in one beamtime.

Table 5.3: Atomic mass results for each beamtime. The experimental values (index *exp*) and the isomeric corrected values (index *iso*) are given for each beamtime. In **All** both data sets have been evaluated as one. For ^{94}Tc and ^{97}Rh an averaged value (index *ave*) is also given. Here the isomeric correction was only to be done in one beamtime. The result from this was averaged with the experimental value from the other beamtime.

2007			
Nuclide	$M_{ST}[\text{keV}]$	$M_{AME}[\text{keV}]$	$\Delta M_{AME-ST}[\text{keV}]$
$^{93}\text{Tc}_{exp}$	-83606(7)	-83603(4)	3(8)
$^{94}\text{Tc}_{exp}$	-84159(8)	-84154(5)	5(10)
$^{94}\text{Tc}_{iso}$	-84148(8)	-84154(5)	6 (10)
$^{94}\text{Ru}_{exp}$	-82569(29)	-82568(13)	1(32)
$^{96}\text{Ru}_{exp}$	-86066(11)	-86072(7)	-6(13)
$^{95}\text{Rh}_{exp}$	-78326(31)	-78339(149)	-13(152)
$^{96}\text{Rh}_{exp}$	-79684(23)	-79679(13)	5(26)
$^{96}\text{Rh}_{iso}$	-79676(23)	-79679(13)	3(26)
^{97}Rh	-82557(8)	-82586(37)	-29(38)
$^{98}\text{Rh}_{exp}$	-83116(7)	-83175(12)	-59(14)
$^{98}\text{Rh}_{iso}$	-83109(11)	-83175(12)	-66(16)
2008			
Nuclide	$M_{ST}[\text{keV}]$	$M_{AME}[\text{keV}]$	$\Delta M_{AME-ST}[\text{keV}]$
$^{93}\text{Tc}_{exp}$	-83607(9)	-83603(4)	4(10)
$^{94}\text{Tc}_{exp}$	-84159(4)	-84154(5)	5(7)
$^{95}\text{Tc}_{exp}$	-86011(5)	-86017(6)	-6(8)
$^{95}\text{Tc}_{iso}$	-86008(6)	-86017(6)	-9(8)
^{94}Ru	-82592(10)	-82568(13)	24(16)
^{96}Ru	-86079(6)	-86072(7)	7(10)
$^{96}\text{Rh}_{exp}$	-79705(9)	-79679(13)	26(16)
$^{96}\text{Rh}_{iso}$	-79697(9)	-79679(13)	18(16)
$^{96}\text{Rh}_{exp}^{oct}$	-79718(15)	-79679(13)	39(20)
$^{96}\text{Rh}_{iso}^{oct}$	-79710(15)	-79679(13)	31(20)
$^{97}\text{Rh}_{exp}$	-82545(12)	-82586(37)	-41(39)
$^{97}\text{Rh}_{iso}$	-82528(12)	-82586(37)	-58(39)
$^{98}\text{Rh}_{exp}$	-83136(5)	-83175(12)	-39(13)
$^{98}\text{Rh}_{iso}$	-83128(10)	-83175(12)	-47(16)
All			
Nuclide	$M_{ST}[\text{keV}]$	$M_{AME}[\text{keV}]$	$\Delta M_{AME-ST}[\text{keV}]$
$^{93}\text{Tc}_{exp}$	-83607(7)	-83603(4)	4(8)
$^{94}\text{Tc}_{exp}$	-84157(6)	-84154(5)	3(8)
$^{94}\text{Tc}_{iso}$	-84146(6)	-84154(5)	-8(8)
$^{94}\text{Tc}_{ave}$	-84155(9)	-84154(5)	1(10)
$^{95}\text{Tc}_{exp}$	-86011(5)	-86017(6)	-6(8)
$^{95}\text{Tc}_{iso}$	-86008(6)	-86017(6)	-9(8)

continued on the next page

continued from previous page			
Nuclide	$M_{ST}[\text{keV}]$	$M_{AME}[\text{keV}]$	$\Delta M_{AME-ST}[\text{keV}]$
$^{94}\text{Ru}_{exp}$	-82583(16)	-82568(13)	15(21)
$^{96}\text{Ru}_{exp}$	-86078(5)	-86072(7)	6(9)
$^{95}\text{Rh}_{exp}$	-78326(31)	-78339(149)	-13(152)
$^{96}\text{Rh}_{exp}$	-79704(9)	-79679(13)	25(15)
$^{96}\text{Rh}_{iso}$	-79696(9)	-79679(13)	17(15)
$^{97}\text{Rh}_{exp}$	-82554(10)	-82586(37)	-32(39)
$^{97}\text{Rh}_{iso}$	-82535(10)	-82586(37)	-51(39)
$^{97}\text{Rh}_{ave}$	-82543(12)	-82586(37)	-43(39)
$^{98}\text{Rh}_{exp}$	-83133(6)	-83175(12)	-42(14)
$^{98}\text{Rh}_{iso}$	-83126(11)	-83175(12)	-49(16)

with σ_1 being the uncertainty of the excitation energy.

Overall we had to suppose an isomeric admixture in the case of five nuclides, while in four nuclides we could rule out the admixture (see section 5.3.2). From literature values on the production rates of ground state and isomeric state and a statistical analysis (section 5.3.1) we could give an upper limit of the possible isomeric admixture in each case, where it could not be resolved. This led to the obtained results shown in table 5.3 and figures 5.5 and 5.6.

5.3.1 Statistical analysis on the resolving power of the two-resonances fit

Both beamtimes aimed for the measurement of the isomeric states in the investigated nuclides. Since the second resonance was not found in any spectrum, the question arose, from which production ratio (between the two states) on, the second resonance will be visible in our measurements. From [Rau06] we know, that a second state with an abundance of about 25% and a cyclotron frequency separation of about 3.5 Hz is clearly visible with the present data evaluation scheme of SHIPTRAP. Nevertheless, the detection probability of a second resonance has not been investigated systematically before. This work now presents a statistical analysis on the visibility of a second resonance in dependance of the cyclotron frequency separation between the resonance centers and the production ratio, using artificially produced spectra where these parameters are predefined. These spectra were fitted with a single-resonance fit and a two-resonances fit. The influence of additional time-of-flight jitter and of the count rate in the second resonance on its detection was analyzed.

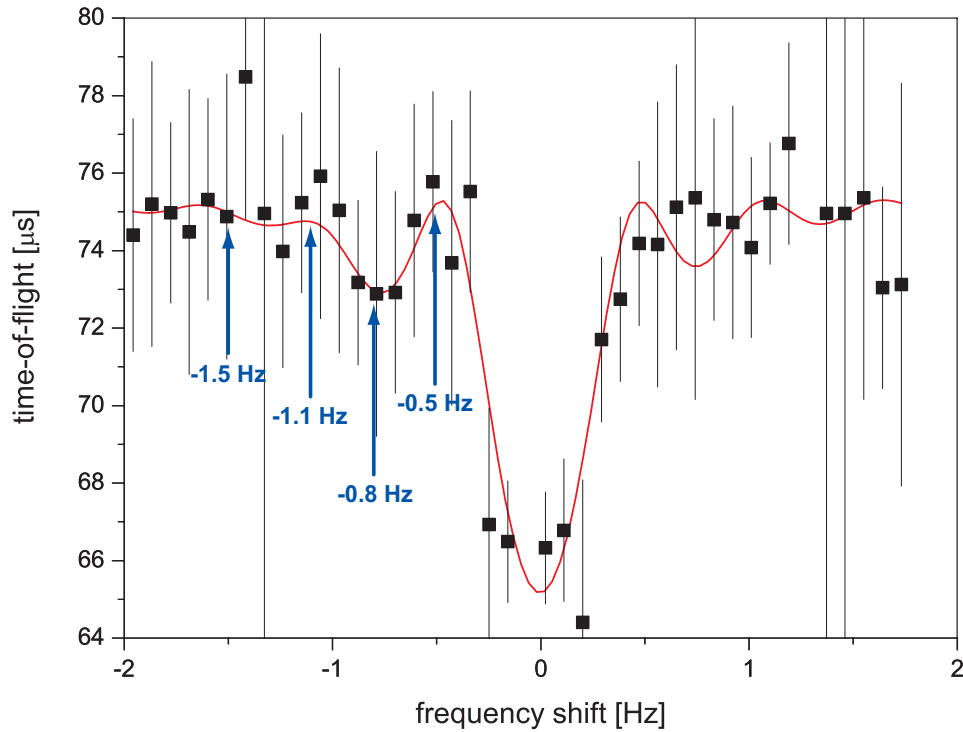


Figure 5.7: Location of the artificial isomeric state resonances. The distances to the ground state resonance are shown. The red curve shows the single-resonance fit with the sidebands.

Production rates of the isomeric states of interest

The production rate of the isomeric state in the measured nuclides depends on the production reaction. From literature we find the following trend for the nuclides we measured: A reaction induced by protons or deuterons on a target with a mass number one less than or equal to the nuclide of interest usually populates the isomeric state much more strongly than the ground state (factor 2 to 30) [Eas53, Ohy74, Ash70, Rao79]. Reactions using heavier projectiles (and a bit lighter targets) tend to populate the isomeric state much less than the ground state (in the order of a few to ten percent) [Zis73, Nol80].

In [Zis73] the production yield of the isomeric state in technetium ^{93}Tc for an 78 MeV beam of ^{12}C on an enriched ^{92}Mo target is given as 7%. We assume similar production rates for the isomeric states in technetium ^{93}Tc and ^{95}Tc as well as rhodium ^{95}Rh and ^{97}Rh , with the reactions $^{92}\text{Mo}(^{12}\text{C},5p,6n)$, $^{92}\text{Mo}(^{12}\text{C},5p,4n)$, $^{92}\text{Mo}(^{12}\text{C},3p,6n)$ and $^{92}\text{Mo}(^{12}\text{C},3p,4n)$, respectively, since these nuclides have equal spin and parity values for the isomeric ($-1/2$) and the ground state ($+9/2$).

Spectrum creation

The basic conditions for the artificial spectra are given by the presumably low production rate and the low excitation energy of the isomeric states of interest, resulting in a low frequency separation. In our measurements all unresolved low-lying isomeric states have a cyclotron frequency separation from the ground state between 0.5 and 1 Hz and lie within the sidebands of the single resonance fit. The isomeric state of rhodium ^{97}Rh with a frequency separation of 3.2 Hz could not be excluded for the beamtime of 2008. At the resolution we obtained then, it lies also within the first two sidebands.

The artificial spectra now address four cases of frequency separation values (see also figure 5.7):

- The isomeric state resonance center coincides with the border of the ground state resonance (in our case -0.5 Hz).
- The isomeric state resonance coincides with the first sideband of the ground state resonance (-0.8 Hz).
- The isomeric state resonance is between the first and the second sideband of the ground state resonance (-1.1 Hz).
- The isomeric state resonance begins at the border of the measurement window (-1.5 Hz)

For each of these cases spectra with mixing ratios between isomeric state and ground state of 5, 10, 15 and 20% were created. To keep the spectra realistic, they were built using an example case - technetium ^{94}Tc -, with a measurement resolution of 0.09 Hz ($8 \cdot 10^{-8}$).

An overview on the spectrum creation can be found in figure 5.8. The first step was to apply a single-resonance fit on the example spectrum, choosing the time-of-flight (TOF) error such, that χ^2 of the fit was 1.0000. The fit curve and the original data points were saved. Also saved were the ions vs. TOF data for each data point.

The theoretical curves of two resonances were created with similar values for TOF window, TOF error, conversion (from magnetron to cyclotron motion) and damping. The frequency separation (called distance) of the resonances and the weight of the first resonance were fixed according to the distance and the mixing ratio the curve should display. This way a set of 16 theoretical curves - four with different weights per distance - were created and saved. Finally 42 measurement points with a step width of 0.09 Hz were created. Each of these data points corresponds to the mean time-of-flight value for the according frequency. To get a realistic count distribution around this TOF value, we shifted the counts from the ions vs. TOF spectra for each frequency by the difference between their original mean TOF and the new one, thus keeping the

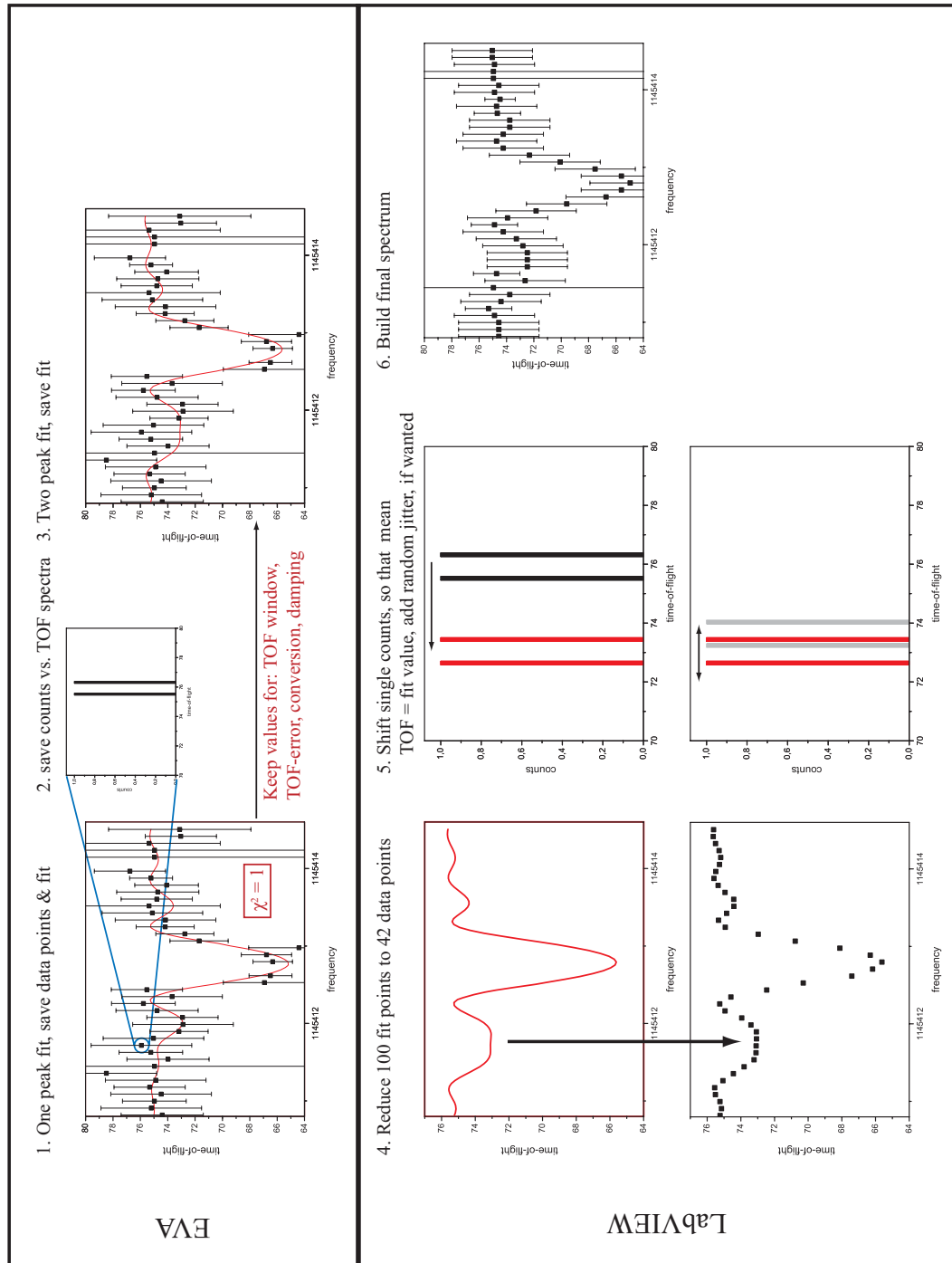


Figure 5.8: Overview on the spectrum creation for the statistical analysis.

distribution. Here a small deviation from the theoretical curve is introduced by the bin width of the ions vs. TOF spectra ($0.16 \mu\text{s}$). In this step an additional random jitter of $\pm 1 \mu\text{s}$ could be applied on this shift. The shifted ions vs. time-of-flight spectra are the data points in the final artificial spectra.

Spectra evaluation

The spectrum evaluation was done in three steps: First, the quality of our artificially generated spectra was checked. Then the artificial spectra without additional jitter were evaluated. These represent single spectra with high statistics. Then the more realistic case of low statistics in the single spectrum was evaluated. To do this, for each case of resonance to resonance distance and resonance weight 20 spectra with random jitter in the data points were created. On these the influence of a higher count rate in the second resonance in comparison to the zero line (the time-of-flight, when no conversion from magnetron to cyclotron motion occurs) was analyzed. Also the effect of a single highly deviating data point within the second resonance was analyzed.

Quality of the artificial spectra: To get an idea, if the generated spectra represent the fitting curves well, an artificial spectrum was constructed from a single-resonance fit using no additional jitter. Then this spectrum was fitted using the original fitting parameters. If the artificial spectrum was perfect, a χ^2 of 0 would be expected. The fit yielded a χ^2 of 0.030. If the parameters were left free, their values did not change, but χ^2 was reduced to 0.028. This is due to the error on the fitting parameters, which is not existent when the parameters are fixed. The difference of χ^2 from 0 is due to the small deviations of the mean time-of-flight values from the nominal fit value due to the bin width. Nevertheless the spectrum creation is accurate enough for our analysis.

Spectra without jitter: To evaluate the spectra without jitter, a limit on the natural variance of χ^2 for the single resonance fit had to be set. For this, 21 spectra with additional jitter of $\pm 1 \mu\text{s}$ were created from the theoretical single resonance curve. All were fitted again using the original fit parameters. The resulting values of χ^2 were averaged and the standard deviation σ was calculated. We found, that the additional jitter reduces the fit reproducibility very much. The averaged χ^2 was 0.13 with a standard deviation of 0.02. In the analysis of the spectra without jitter, a deviation of 0.1, which is 5σ , in the values of χ^2 for the single and the two resonance fit was defined as significant.

The 16 spectra - one for each distance and weight - were fitted using the original fit parameters (TOF window, TOF error, conversion and damping) from the single resonance fit. The two resonances fit was done twice, first with fixed weight and distance, second, with both parameters running free. By this the detection power for an unknown resonance was tested.

Spectra with jitter: In the next step, additional jitter was added to the data points in the spectra with two peaks to deduce an upper limit for the production rate. Now the values for χ^2 scattered widely for both fits. Therefore a sample of 20 spectra for each distance and weight was created. These were fitted in the same way as the spectra without jitter. The values for χ^2 were averaged, the variance and the standard deviation were calculated for each sample and fit. The mean values of χ^2 for the single and the two resonance fit for each sample were compared. A t-test was employed to evaluate the significance of their difference.

The t-test is a hypothesis test of the form:

$$t = \frac{\bar{x}_1 - \bar{x}_2}{\sqrt{\frac{v_1}{n_1} + \frac{v_2}{n_2}}} \quad (5.6)$$

with \bar{x}_a being the mean value of the according sample a, v_a the variance and n_a the size of the sample. It is applicable for normal distributed sample values (given by the random jitter) and independent samples (the values for χ^2 stem from different fitting procedures). In the form used here it is also applicable for a non-equal variance of the samples. The t-test evaluates, if a statistic complies with the t-distribution, and is the standard test for the comparison of two mean values. We tested the hypothesis, that both mean values are equal. The quantile Q for the t-distribution for a two sided test at a significance level of 5% is 2.1. If $t > Q$ our hypothesis is not valid. The results of the t-test are shown in table 5.7.

Then we increased the count rate in the second resonance by a factor of 1.5. This was done, since the count rate in the main resonance is higher, than in the zero line. We evaluated samples of 10 spectra for each combination of distance and weight. Again a t-test was employed.

The influence of a single highly deviating data point in the second resonance was examined. In some of the spectra with a higher count rate one data point in the -0.5 Hz second resonance was off the theoretical curve by more than 1.5 TOF error. We shifted this point back to a value near the theoretical value and compared the fit results from this to the results with the deviated point.

Results

Spectra without jitter: The results are shown in tables 5.4 and 5.5 as well as figures 5.9 and 5.10. Taking 5σ as the significance limit, we find, that the second resonance becomes clearly detectable from a production rate between 15% and 20%. As expected, the rate has to be higher at the border of the first resonance (-0.5 Hz) to reach a clear distinction. But this is only valid, when the distance and the weight of the second resonance is - at least approximately

Table 5.4: Results for the statistical analysis on the isomer resolution for the spectra without jitter. Given are the χ^2 values for the single resonance fit and the two resonances fit with fixed resonance weight and distance.

2^{nd} resonance weigh [%]	distance [Hz]							
	-0.5		-0.8		-1.1		-1.5	
	single	two	single	two	single	two	single	two
5	0.029	0.029	0.030	0.029	0.032	0.031	0.030	0.030
10	0.049	0.040	0.063	0.029	0.054	0.033	0.044	0.035
15	0.087	0.040	0.114	0.031	0.105	0.044	0.076	0.035
20	0.155	0.040	0.215	0.025	0.168	0.025	0.126	0.027

Table 5.5: Results of the two resonances fit with distance and weight running. Given are the χ^2 values for the spectra without additional jitter. n.f. means, that the second resonance was not found by the fit. For all cases, the error on the weight is in the order of 0.10%, the error on the distance is in the order of 0.3 Hz.

2^{nd} resonance weigh [%]	nominal distance [Hz]					
	-0.5			-0.8		
	χ^2	dist	weight	χ^2	dist [Hz]	weight
5	0.026	.n.f.	.n.f.	0.028	.n.f.	.n.f.
10	0.036	-0.47	0.93	0.030	-0.82	0.91
15	0.037	-0.49	0.88	0.031	-0.82	0.86
20	0.036	-0.49	0.83	0.024	-0.83	0.81

2^{nd} resonance weigh [%]	nominal distance [Hz]					
	-1.1			-1.5		
	χ^2	dist [Hz]	weight	χ^2	dist [Hz]	weight
5	0.031	.n.f.	.n.f.	0.030	.n.f.	.n.f.
10	0.032	-1.04	0.92	0.033	-1.50	0.96
15	0.043	-1.08	0.87	0.034	-1.48	0.87
20	0.023	-1.07	0.82	0.025	-1.50	0.83

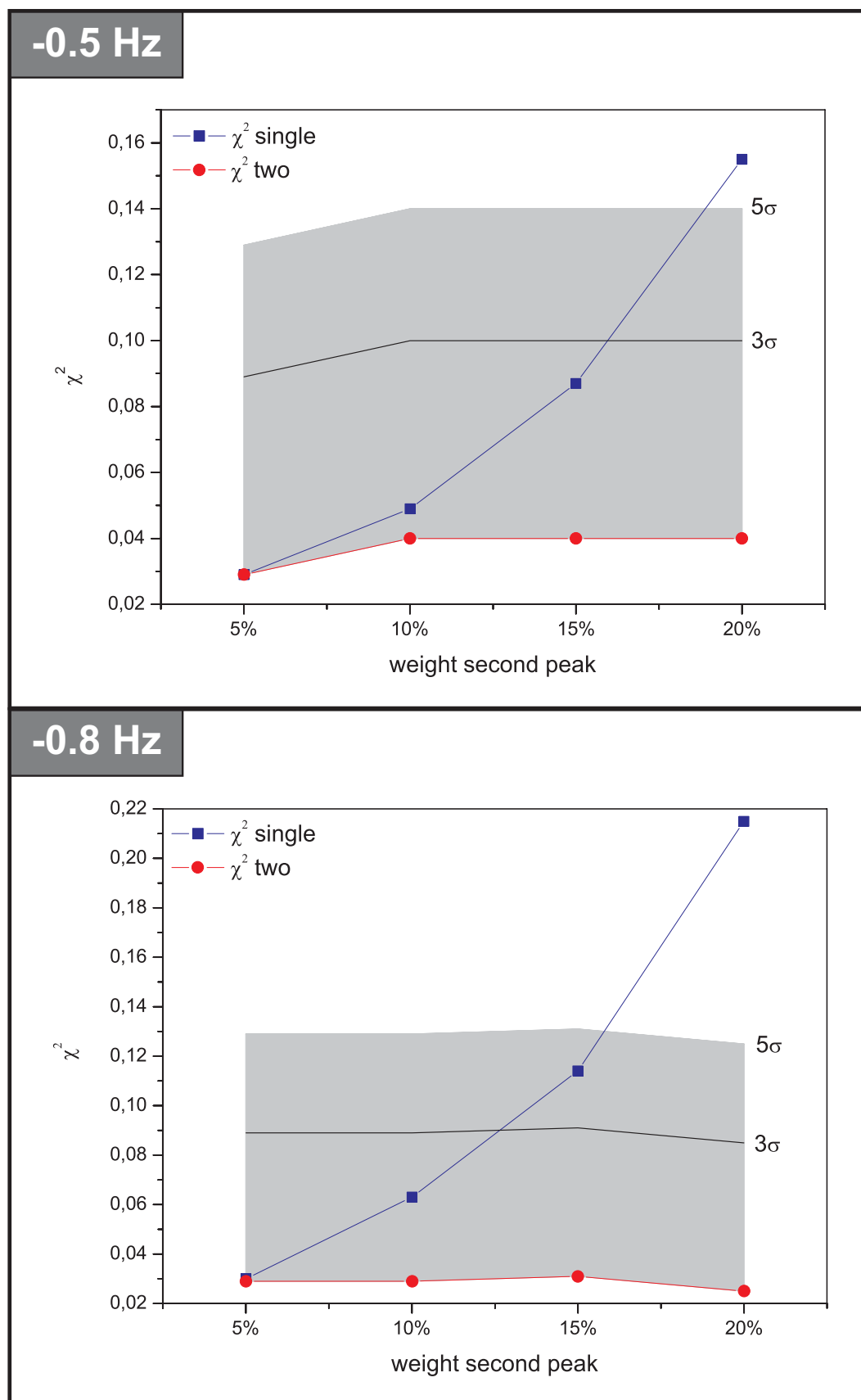


Figure 5.9: Results for the statistical analysis on the isomer resolution for the distance -0.5 Hz and -0.8 Hz. χ^2 is given for the single (blue) and the two resonance fit (red). The shaded area is the positive 5σ area, while the 3σ difference is marked by a black line.

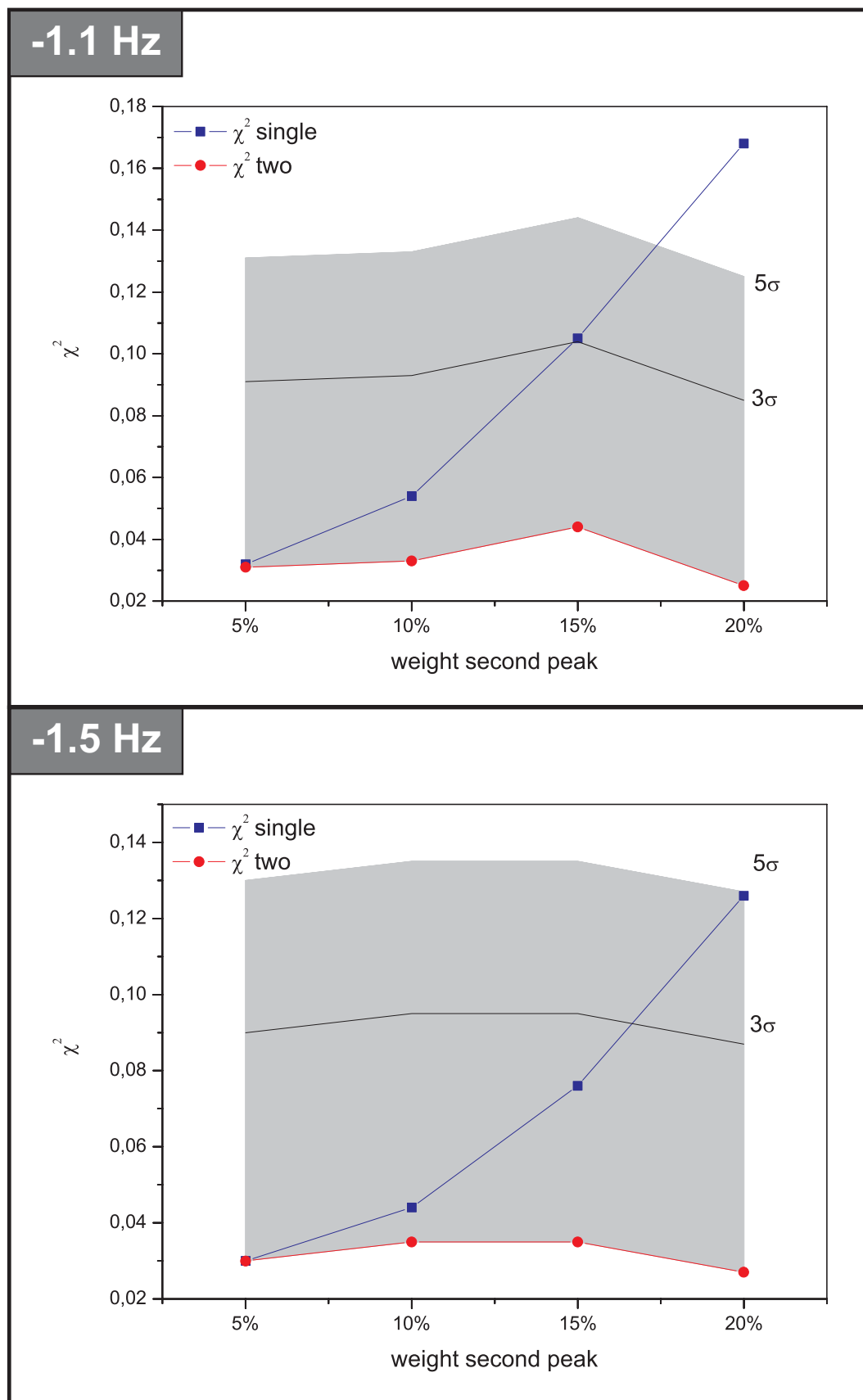


Figure 5.10: Results for the statistical analysis on the isomer resolution for the distances -1.1 Hz and -1.5 Hz. χ^2 is given for the single (blue) and the two resonance fit (red). The shaded area is the positive 5σ area, while the 3σ difference is marked by a black line.

Table 5.6: Results for the statistical analysis on the isomer resolution for spectra with jitter. Given are the mean χ^2 values for the single and the two-resonances fit with fixed resonance weight and distance with their standard deviation σ . The samples consisted of 20 spectra each.

2^{nd} resonance depth [%]	nominal distance [Hz]							
	-0.5				-0.8			
	single χ^2	sigma	two χ^2	sigma	single χ^2	sigma	two χ^2	sigma
5	0.125	0.021	0.126	0.021	0.133	0.024	0.128	0.24
10	0.152	0.029	0.146	0.025	0.166	0.034	0.137	0.28
15	0.187	0.026	0.146	0.011	0.233	0.046	0.148	0.22
20	0.273	0.067	0.158	0.038	0.317	0.048	0.143	0.28
2^{nd} resonance depth [%]	nominal distance [Hz]							
	-0.5				-0.8			
	single χ^2	sigma	two χ^2	sigma	single χ^2	sigma	two χ^2	sigma
5	0.133	0.022	0.128	0.023	0.137	0.028	0.134	0.030
10	0.171	0.047	0.154	0.048	0.141	0.024	0.129	0.027
15	0.195	0.048	0.138	0.033	0.182	0.036	0.149	0.032
20	0.285	0.61	0.151	0.054	0.237	0.038	0.158	0.40

- known, since the second resonance at -0.5 Hz is not found, when these two parameters are running free. If the second resonance lies directly in the first sideband of the main resonance (-0.8 Hz), it is detected reliably if the resonance weight is a few percent higher than the sideband depth. When the second resonance lies between the first two sidebands, the production rate has to be a bit higher, to clearly detect the second resonance. At the border of the measurement window the second resonance is resolved only from an abundance of the 20% on. One has to remember, that the spectra without jitter represent real spectra with high statistics, so to say a 'best case'. The results show, that we are not able to measure a second resonance with a production rate of under 10% in a single spectrum.

Spectra with jitter: In the spectra with additional jitter we found the values for χ^2 to straggle strongly from spectrum to spectrum, with a higher variance for the single resonance fit. The unambiguous detection of a second resonance is just possible in some spectra. Averaging the values for χ^2 - 20 values for the single resonance fit and 20 for the two resonance fit for each distance and weight pair - we find a deviation of the mean values as shown in table 5.6 and figures 5.11 and 5.12. The mean values show the same trend as the values for χ^2 for the jitter-free spectra - χ^2 for the single resonance fit increases significantly with the weight of the second resonance, χ^2 for the

Table 5.7: Results of the T-test on the mean χ^2 of the single and the two resonances fit. True states, that the mean χ^2 of the single and the two resonances fit are equal with 95% confidence, false, that they are not equal.

2 nd resonance depth [%]	distance [Hz]			
	-0.5	-0.8	-1.1	-1.5
5	true	true	true	true
10	true	false	true	true
15	false	false	false	false
20	false	false	false	false

two-resonances fit stays roughly the same.

The significance of the deviation of the mean χ^2 of the single and the two resonances fit was tested with the t-test. The results are shown in table 5.7. The confidence level chosen for the test was 95%, true shows that the mean values are equal, false shows that they are not equal within the confidence level. From the t-values we can even state, that the results shown in table 5.7 are valid for a confidence level of 98.7%. For a confidence level of 99.9% the result of the t-test only switches to true for -0.8 Hz/10% and -1.5 Hz/15%.

From a sample of spectra with low statistics, the second resonance can be detected clearly from a mixing ratio of 15% on. In a single spectrum with low statistics this is not necessarily possible. This is in agreement with the fact, that from a mixing ratio of 15% the second resonance was very well detected by the two-resonances fit with the fit parameters distance and weight running free. Nevertheless the weight of the second resonance is in most cases underestimated by a few percent.

Increasing the number of counts in the second resonance enhanced the detection probability just slightly. The t-test for a cyclotron frequency separation of -0.8 Hz was positive for all weights (95% confidence). This might be due to a better distinction between a second resonance and the sideband of the first resonance due to the higher count rate. Nevertheless this result has to be taken carefully, since it might be a false interpretation of the sideband by the fit procedure. The only true change in the result is the better detection of the -1.5 Hz resonance - now from 10% on. All in all the variance of the χ^2 values for the two resonance fit in respect to the variance of the single resonance fit decreases with the enhanced count rate in the second resonance.

The comparison of spectra (for a distance of -0.5 Hz and higher count rate) where all data points of the second resonance were near the theoretical value and spectra where one of these data points was off by more than 1.5 TOF error showed, that a clear detection of the second resonance is possible from 10%

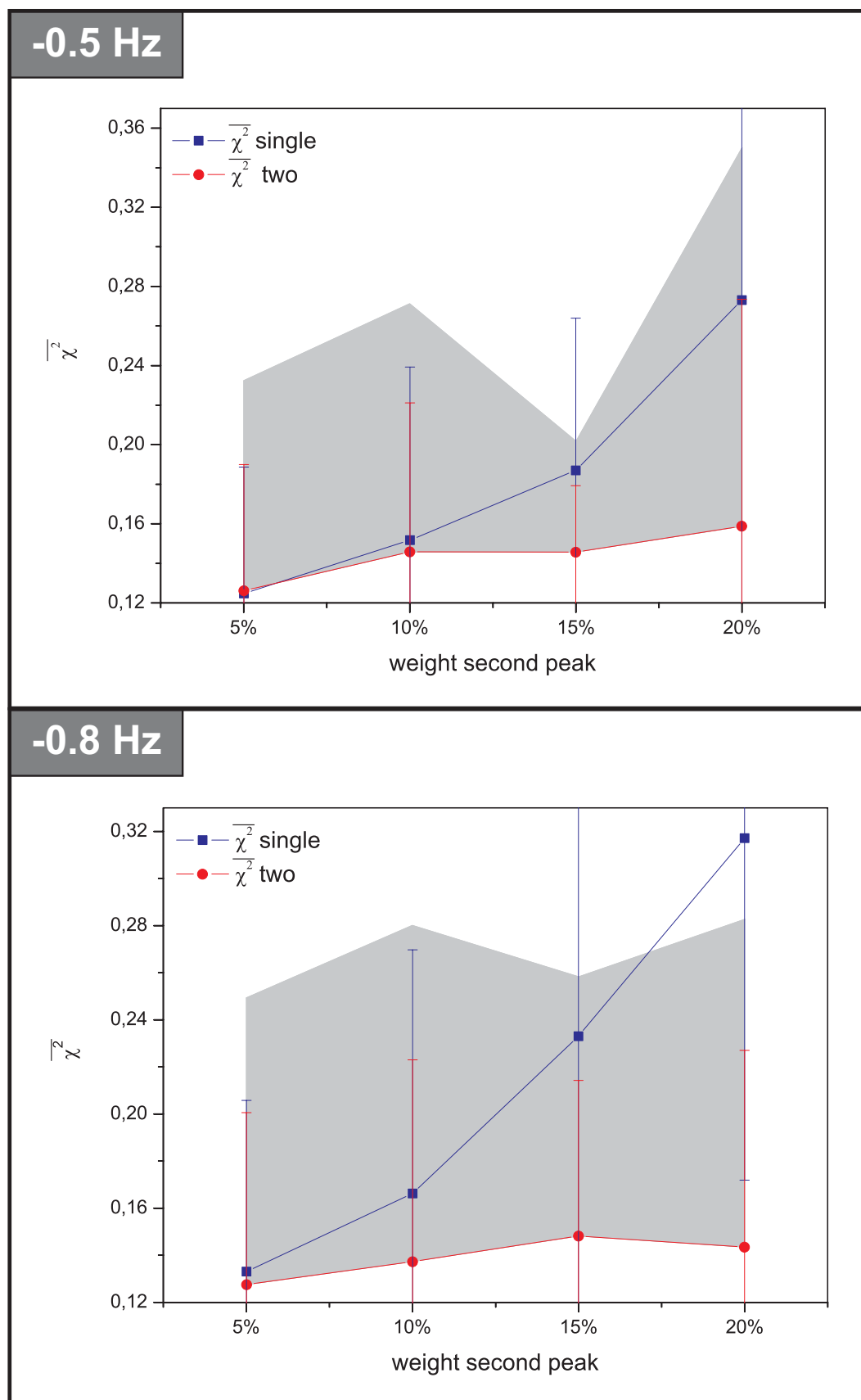


Figure 5.11: Results for the statistical analysis on the isomer resolution for spectra with jitter for the distances -0.5 Hz and -0.8 Hz. The mean χ^2 from a sample of 20 spectra is given for the single (blue) and the two resonances fit (red). The shaded area is the positive 5σ area of the two resonances fit. The error bars give the 3σ distance.

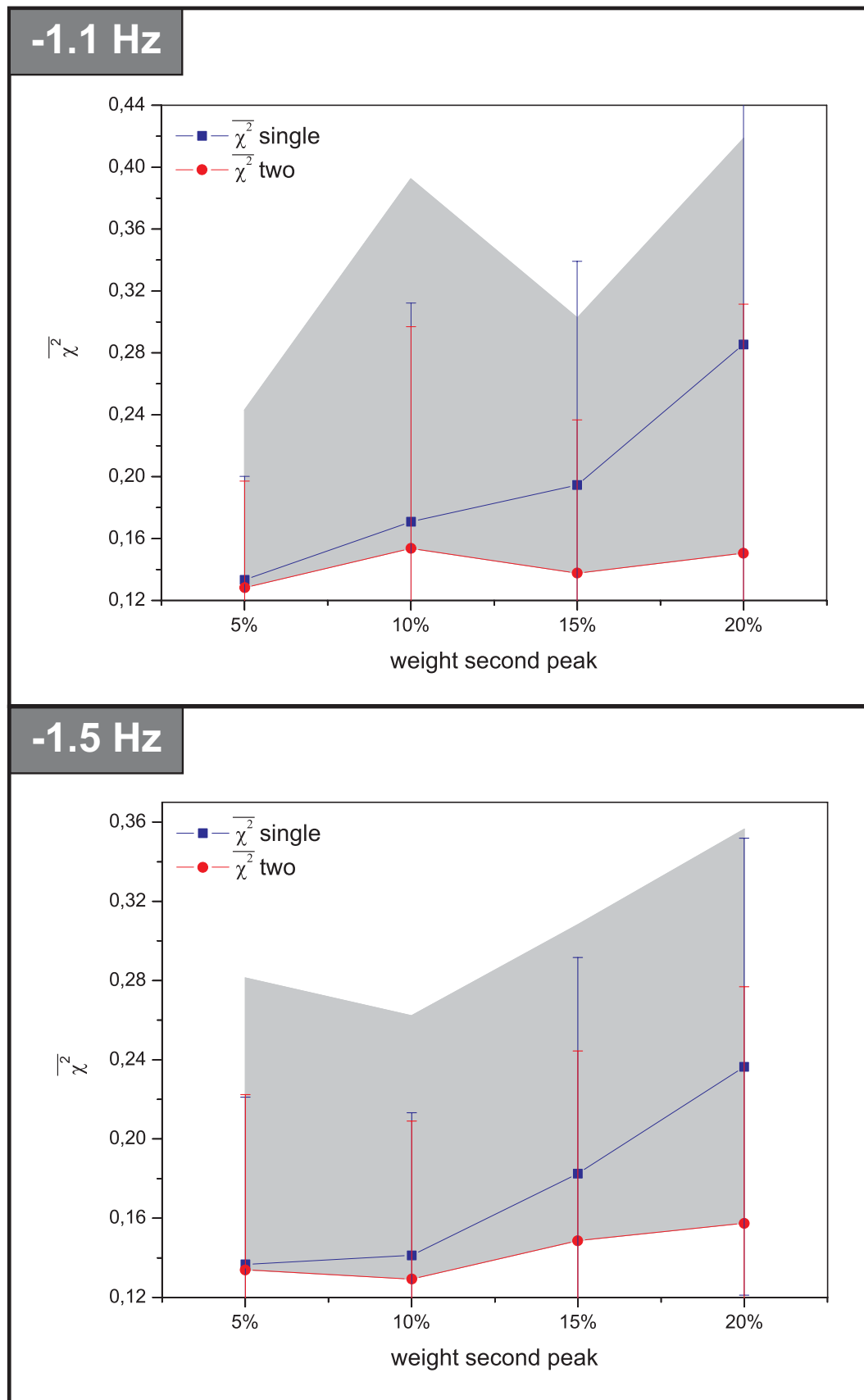


Figure 5.12: Results for the statistical analysis on the isomer resolution for spectra with jitter for the distances -1.1 Hz and -1.5 Hz. For each distance the mean χ^2 from a sample of 20 spectra is given for the single (blue) and the two resonances fit (red). The shaded area is the positive 5σ area of the two resonances fit. The error bars give the 3σ distance.

on, when all data points are close to the theoretical value.

Summarizing, we find for our cases of spectra, that a second resonance can be clearly resolved from a mixing ratio of about 15% on. In single spectra this or even a slightly lower mixing ratio is resolvable, if the statistics are high. In spectra with low statistics, a statistical analysis might be necessary to verify the detection of the second resonance. Even if the distance between the resonances and the mixing ratio is not known, the two resonances fit detects the second resonance reliably from a mixing ratio of 15%. However, the error in the weight is in the order of 7%. Turning the argument, we can conclude that in those cases, where we could resolve the isomeric state, but do not detect it, its production ratio is under 15%.

5.3.2 Discussion of the isomeric state admixtures

The average number of ions in the measurement trap at SHIPTRAP is about one to two. Given a production rate for the isomeric state of under 15%, we can assume, that we do not have both, the ground state and the isomeric state, in the trap at the same time. Therefore an isomeric correction is not necessary, when the resonances of ground state and isomeric state are resolved.

⁹³Tc

Both known isomeric states could be excluded from our measurement. The n-state has a lifetime of only 10.2 μ s, which means, that this state has decayed before the ion is measured with a typical excitation time of 900 ms. The m-state has a lifetime of 43.5 m and an excitation energy of 392 keV, which corresponds to a cyclotron frequency shift of more than 5 Hz. This could be clearly resolved with 900 ms excitation time, but was not seen in any of the measurements. The population ratio of isomeric state to ground state in ⁹³Tc for the reaction of an 78 MeV ¹²C beam on an enriched ⁹²Mo target is given in [Zis73] as 7%. We conclude, that we see only the ground state.

⁹⁴Tc

The isomeric state of ⁹⁴Tc has a lifetime of 52 min and an excitation energy of 76 keV, leading to a frequency shift of 1 Hz. This could not be resolved in the 2007 beamtime. Since the state was not detected in the 2008 beamtime, where the resolution was good enough, we assume that the admixture of the isomeric state was under 15% and we only see the ground state in the data from 2008. The resonance would lie in the first sideband, where it should be clearly detectable with a mixing ratio of 15% or more. So we can give an upper limit for the production of the isomeric state in the reaction ¹²C on ⁹²Mo. Therefore the isomeric correction was done for an admixture of 15%.

⁹⁵Tc

The excitation energy of the m state is 39 keV, corresponding to a shift of 0.5 Hz, which was not resolved. The lifetime of 61 days meant that here the

isomeric correction also had to be done. We assume the same ratio as for ^{93}Tc , 7%, since the spin and parity values of ground and isomeric state are the same as in ^{93}Tc .

^{94}Ru

Since the lifetime of the known isomeric state of ^{94}Ru is only 71 μs , and the state decays therefore well before the measurement trap, an isomeric admixture can be excluded.

^{96}Ru

^{96}Ru is a stable element with no isomeric states.

^{95}Rh

The excitation energy of the first isomeric state in ^{95}Rh is 543 keV and corresponds to a frequency shift of 7 Hz, which would have been clearly resolved but is not detected. We assume here also a production ratio of 7% for the isomeric state - the same spin and parity values as in ^{93}Tc -, so that the detected state is the ground state.

^{96}Rh

The isomeric state has a lifetime of 1.5 minutes and an excitation energy of 52 keV, which results in an unresolved frequency shift of 0.7 Hz. Since in some spectra, the second resonance would be found at the border of the first resonance, and should therefore be detectable from an admixture of 15% on, the isomeric correction was done for a mixing ratio of 15% as an upper limit on the production rate.

^{97}Rh

The data from the beamtime 2008 did not show a good enough resolution to clearly distinguish between the ground state and the isomeric state 3 Hz away (excitation energy of 259 keV). Nevertheless, the resolution of most of the spectra from 2007 was good enough and the isomeric state was not detected here. We assume a production rate of about 7% as for ^{93}Tc in both beamtimes. For the data from 2008 an isomeric correction for an admixture of 7% was done, while we assume, that in the data of 2007 only the ground state is measured - especially since the frequency ratios within each beamtime do not differ so much, but from beamtime to beamtime, they differ by more than one standard deviation. The data set for **AII** is without isomeric correction. Averaging the mass excess values for the 2007 and the 2008 beamtime, the latter with isomeric correction, leads to a value of 82561(14) keV.

^{98}Rh

The isomeric state with a lifetime of 3.6 m and an extrapolated excitation energy of 50 keV, corresponding to a frequency shift of 0.6 Hz, could not be resolved in both beamtimes. In one spectrum from 2008, the resolution would be good enough to detect the second resonance, but it is not seen there, so the

relative production rate is under 15%. The isomeric correction was done for an admixture of 15%.

5.4 Discussion of the obtained results

5.4.1 Comparison between this work and the Atomic Mass Evaluation

^{93}Tc

The mass excess of -83607(7) keV for the ground state measured in this work is in good agreement with the value in the AME of -83603(4) keV, which comes from the Q-value of the β^+ -decay of the 10.8 s isomer in ^{93}Ru and the $^{92}\text{Mo}(p,\gamma)^{93}\text{Tc}$ resonance reaction [Äys73]. A more recent value of -83582(29) keV from Schottky mass spectrometry at the ESR at GSI [Lit05] is consistent within its much bigger uncertainty.

^{94}Tc

The AME value for the mass excess of ^{94}Tc (-84154(5) keV) is derived independently from the Q-values of the β^+ -decay of ^{94}Tc [McP73] and the reaction $^{94}\text{Mo}(p,n)^{94}\text{Tc}$ [Ham64]. This is in perfect agreement with the value measured in this work (-84154(9) keV), which is the average between the isomeric corrected value for the data of 2007 and the value for 2008. The value derived from Schottky mass spectrometry at the ESR [Lit05] with isomeric correction (-84171(36) keV) agrees with both values, due to its higher uncertainty. We can conclude from our data, that the assumption of an upper limit for the isomeric admixture of 15% is valid. Taking the AME value as reference, we can estimate the isomeric admixture to be less than 10%. Since the averaged value and the value without isomeric correction for all data sets are equal within the uncertainty, we cannot exclude the production of the isomeric state.

^{95}Tc

Due to the small admixture of 7%, the mass excess values with (-86008(6) keV) and without isomeric correction (-86011(5) keV) are equal within the uncertainty. Since the admixture could not be ruled out, the relevant value is the one with the isomeric correction. This agrees well with the AME value (-86017(6) keV). The latter is derived from the averaged Q-value of $^{95}\text{Tc}(\beta^+)^{95}\text{Mo}$ [Cre65, Ant74]. Here again a value (corrected for an unknown isomeric contamination) from a Schottky mass measurement at GSI is given in [Lit05]. With -86086(30) keV this is by 2σ off our measurement.

^{94}Ru

The mass excess value obtained in this work (-82583(16) keV) agrees well with the data from the AME (-82568(13) keV), which is derived from the β -decays of the 26-s and the 71-s states of ^{94}Rh [Oxo80] and the reaction

$^{96}\text{Ru}(\text{p,t})^{94}\text{Ru}$ [Bal71].

^{96}Ru

The ground state mass excess of ^{96}Ru was determined in this work to $-86078(5)$ keV. This is in good agreement with the AME value of $-86072(7)$ keV, which was derived from a comparison to C_7H_{12} (79%) [Dam63] and Q-values of $^{96}\text{Ru}(\text{p,d})^{95}\text{Ru}$ [Bal71].

^{95}Rh

The mass excess given in the AME ($-78339(149)$ keV) comes from the Q-value of $^{95}\text{Rh}(\beta^+)^{95}\text{Ru}$ [Wei75]. Our value of $78326(31)$ keV is in very good agreement with this. We could reduce the uncertainty by a factor of almost 5.

^{96}Rh

For ^{96}Rh the mass excess value obtained within this work ($79696(9)$ keV) agrees with the AME value of $79679(13)$ keV within 2σ , respectively. The AME value stems from the mentioned mass excess of ^{96}Ru [Dam63] combined with the $^{96}\text{Ru}(\text{p,n})^{96}\text{Rh}$ reaction Q-value [Ash70]. The resulting value was recalculated by Rykaczewski et al. to the actual value [Ryk85]. Here again, our values with and without isomeric correction are equal within the uncertainty, so that the production of the isomeric state cannot be excluded.

^{97}Rh

This work determined the mass excess of ^{97}Rh to $-82543(12)$ keV. This is the average between the mass excess for the 2007 beamtime and the isomeric corrected mass excess for the 2008 beamtime, since in the latter the admixture could not be ruled out. The isomeric correction was done with an admixture of 7%. Our measurement agrees with the AME value of $-82586(37)$ keV within the uncertainty. This value was obtained from the $^{97}\text{Pd}(\beta^+)^{97}\text{Rh}$ reaction [Gök80]. The uncertainty of this mass could be reduced by this work by a factor of 3. All three values given in table 5.3 agree within the uncertainty, so that here again no further statements on the production rate of the isomer are possible.

^{98}Rh

The mass excess for ^{98}Rh obtained in this work ($-83126(11)$ keV) deviates by more than 3σ from the value stated in the AME ($-83175(12)$ keV). The AME value is derived from the reaction $^{98}\text{Ru}(\text{p,n})^{98}\text{Rh}$ [Ash70]. The study of the β^+ -decay of ^{98}Rh to ^{98}Ru yields the same value as the AME, but with a larger uncertainty [Ban94], whereas the Schottky mass spectrometry experiment from 2003 yields a value of $-83184(43)$ keV with isomeric correction included [Lit05]. For this nuclide again, the difference between the isomeric corrected value and the uncorrected value is smaller than the uncertainty.

5.4.2 Discussion of the results

The statistical analysis shows that the resolution of low-lying isomeric states with production rates of 15% and more can be detected with the present SHIPTRAP measurement technique. Since no isomeric state was detected, we conclude that the production rates of the isomeric states in all isotopes was below 15%. This is in good agreement with [Zis73], where the production ratio for the first isomeric state of ^{93}Tc was measured for the same production reaction as used in this work. In the measured nuclides, which have other spin and parity values for ground and isomeric state than ^{93}Tc , we find the isomeric states also weakly populated. In the quest for low-lying isomeric states, a reaction with a proton or deuterium projectile might be advantageous. Using the cryogenic FT-ICR set-up at SHIPTRAP, which allows for longer excitation times and therefore higher resolution, might improve the situation. The 15% minimum production ratio refers to a second resonance near the first one. At higher resolution this is overcome. With further studies on the yet unsuccessful octupolar excitation scheme, the resolution of the present set-up might also be improved to resolve the isomeric states with about 1 Hz frequency difference to the ground state with a production rate of less than 15%.

We find, that the mass measurements with SHIPTRAP agree well with the data from the Atomic Mass Evaluation. For the rhodium isotopes ^{95}Rh and ^{97}Rh the uncertainty of the mass excess values have been reduced by a factor of 5 and 3, respectively.

Two values, the ones for the rhodium isotopes ^{96}Rh and ^{98}Rh , deviate more strongly from the literature values, even with the isomeric correction applied, in case of ^{98}Rh even by more than 3σ . This is not due to an underestimation of the isomeric admixture. In ^{96}Rh the admixture would have to be in the regime of more than 30% to push the values close enough together. This would have been clearly detected in the spectra with high enough resolution, which was not the case. The 2007 mass excess value agrees very well with the AME value. Due to its lower statistics than the 2008 data, the overall value is not too much influenced by the 2007 data. For ^{98}Rh the case for the isomeric admixture is vice versa. An assumed larger isomeric admixture would enhance the discrepancy. In both cases our data is the first direct mass measurement with the same precision as the AME value.

Chapter 6

Summary, conclusions and outlook

In this thesis an overview on the experimental facilities of HITRAP and SHIPTRAP within the framework of GSI was given. All parts of both facilities were described in detail in their present status.

For HITRAP, which is still in the commissioning phase, the linear decelerator was described, with the results of the commissioning runs up to now. The design and the status of the Cooler Penning Trap was discussed. A part of the scientific program foreseen at HITRAP was introduced. Here special attention was paid to the mass measurements, since part of this thesis also covers mass measurements at SHIPTRAP.

For SHIPTRAP the features of the gas cell, the radio-frequency cooler and buncher and the Penning traps were discussed. SHIPTRAP is fully operational and mass measurements around $A = 96$ were performed.

This work had two main objectives. First the detection and cooling electronics for the HITRAP Cooler Trap have been developed and built. The principle of resistive cooling was explained. Within this work, the coils for the resonant circuits for the detection and cooling of the axial and the cyclotron motion were designed and set up. The results of the optimization process of the geometry and winding technique as well as the test results of the final coils were presented. A cryogenic amplifier was built and tested as well as noise filters for the electrode voltage supply lines. Furthermore, an indium-sealed UHV-chamber to house all cryogenic electronics was designed and built.

The second objective was the resolution of isomeric states in mass measurements at SHIPTRAP. The results of these mass measurements - nine masses around $A = 96$ - were presented and discussed. In these measurements the octupolar excitation scheme in the Penning trap was tested and studied. A statistical analysis on the resolving power of low lying isomeric states for the present SHIPTRAP measurement scheme was presented. It has been found,

that a production rate of 15% is necessary for the isomeric state to be detected.

The implementation of a field programmable gate array as timing card for HITRAP was described. This card is already successfully used at SHIPTRAP, so that this part of the work connects both experimental facilities.

At HITRAP now the last steps to an operational facility are taken. The last beamtime from April 6th to 12th 2009 was dedicated to the commissioning of the radio-frequency quadrupole structure, the last part of the linear decelerator. All electrodes of the Cooler Trap have been gold-plated and the final assembly of the trap is now under way. The magnet was already tested in 2007, so that first tests of the trap will be possible in May or June 2009. These tests will be conducted with a test ion source and include the transmission test of the low energy beam transport line and the injection, storage and cooling of ions in the trap itself. As a first experiment at the trap, the electron string mode of a dedicated electron source will be characterized. All in all first on-line trap test are expected end of the year 2009.

As soon as the trap will be operational, the final adjustments of the coils for the resonant circuits can be done. First tests on the cooling of the ions in the trap will show, if the low quality factor of the resonant circuit with preamplifier results in a good cooling behaviour by addressing a broad bandwidth. If the bandwidth need to be decreased, a coil and resonator made of superconducting material is proposed.

The cooling tests will be the first experimental insights in resistive cooling of a large ion cloud. This will provide a crucial test on the simulations done in this area, giving a chance to refine the simulations and leading to an interplay of simulation and experiment. The simulations can help to understand effects coming from contaminant ions or can be used to do systematic studies on the effect of the bandwidth of the resonant circuit on the cooling behaviour of the trapped ions. These results again can lead to optimizations in the set-up.

The vertical beam line, connecting the Cooler Trap with the experiments, will be set up until the end of the year 2009, so that first cooled ions will be available for the experiments beginning of 2010. The EBIT, working as offline ion source, is being installed on top of the reinjection channel right now. The by now most advanced experimental set-up is the laser spectroscopy experiment SPECTRAP, while the surface experiment from KVI in Groningen will soon arrive at GSI.

SHIPTRAP has shown its high potential in mass-measurements on nuclides near the proton drip-line [Rau06] and recently also of short-lived transuranium nuclides like nobelium [Blo09]. The resolution of isomeric states is of high interest for the accuracy of the measured masses, the precise determination of the excitation energy of these states and the prediction of what to expect far

out from stability. Therefore, octupolar excitation of the cyclotron motion in the Penning trap should be employed. This should gain a ten times higher resolution. First promising tests were conducted and further studies are now under way.

At the moment a cryogenic stopping gas cell for SHIPTRAP is designed. This will give a higher gas density at the same pressure (factor four at 77 K), leading to more efficient stopping and a smaller stopping distribution. Furthermore, higher RF amplitudes at the exit funnel will be possible in this set-up, so that the extraction efficiency will also be enhanced. The cryogenic gas cell will enable SHIPTRAP to study more transuranium isotopes, which are not reachable with the present set-up due to their small production cross-sections.

Furthermore a Fourier-Transform Ion-Cyclotron-Resonance detection set-up for SHIPTRAP has been developed [Ket06]. This will enable higher mass resolution due to longer excitation times, and therefore the resolution of isomers.

A future prospect for both facilities is the quest for the absolute value of the neutrino mass. This can be determined taking advantage of electron capture decays. The calorimetric spectrum of this decay is an inverse neutrino spectrum due to the two-body nature of the process. If one compares the mass difference of mother and daughter nuclide (the excited state of the daughter nuclide, respectively), Q , and the calorimetric spectrum of the decay, the difference between the endpoint of the spectrum and Q should give the neutrino rest mass [Nov09]. A first screening of the candidates is to be done at SHIPTRAP and at ISOLTRAP at CERN. This pins down the candidates useful for the final mass measurements, which should take place at the five-fold Penning trap situated at HITRAP.

Appendix A

Fast-Fourier-Transformation

The FFT is a special case of the discrete Fourier Transformation, which can be derived from the continuous one:

$$\mathcal{F}\{f(t)\} = F(\nu) = \int_{-\infty}^{\infty} g(t)e^{-i2\pi ft} dt \quad (\text{A.1})$$

This continuous transformation pair $f(t)$ and $F(\nu)$ has to be transformed into a discrete pair for digital processing [Bri97]. First the analogue signal has to be band-width limited, for example with a band pass filter. The discretization is then done by convolution of the time domain signal with a series of delta functions at a sampling frequency $1/T$.

$$\Delta(t) = \sum_n \delta(t - nT) \quad (\text{A.2})$$

This leads to a series of discrete values

$$\hat{f}(t) = \sum_n f(nT)\delta(t - nT) \quad (\text{A.3})$$

and their Fourier Transformation

$$\mathcal{F}\left[\hat{f}(t)\right](\nu) = \sum_n \mathcal{F}[f(t)]\left(\nu - \frac{n}{T}\right) \quad (\text{A.4})$$

which is a convolution of the Fourier transformations of the delta function and the time domain signal. The sampling frequency has to be at least twice the band-width to avoid overlaps between two samples (so-called aliasing). To enable the processing the analogue sampled signal has to be time limited, which is realized by convolution with a rectangular function of the form

$$r(t) = 1 \quad \text{for } -\frac{T}{2} < t < T_0 - \frac{T}{2}, \\ r(t) = 0 \quad \text{else.} \quad (\text{A.5})$$

The window T_0 can be chosen in a way, that time domain overlaps are excluded and N samples are within it. In the frequency domain this procedure will add some distortion due to the time limitation. Since we need a pair of discrete

functions the frequency domain has to be sampled as well. This leads to a time domain function consisting of the analogue signal, the delta function and the rectangular function, convoluted with the inverse Fourier Transformation of the sampling function from the frequency domain. This gives us the discrete Fourier Transformation

$$F\left(\frac{n}{NT}\right) = \sum_{k=0}^{N-1} h(kT) e^{\frac{-i2\pi nk}{N}}; \quad \text{with } n = 0, \dots, N-1 \quad (\text{A.6})$$

The Fast Fourier Transformation now uses the Cooley-Turkey algorithm [Coo65] for the reduction of calculation steps within the discrete Fourier Transformation. If we rewrite equation A.6 with k for kT and n for n/NT , and defining a matrix $W \equiv e^{\frac{-i2\pi}{N}}$, we get:

$$F(n) = \sum_{k=0}^{N-1} h(k) W^{nk}; \quad \text{with } n = 0, \dots, N-1 \quad (\text{A.7})$$

The calculation of the transformation consists of N^2 complex multiplications and $N(N-1)$ complex additions. These numbers are reduced by factorizing the matrix W . Consider the special case $N = 2^\gamma$ ($\gamma \in \mathbb{N}$), where we can write n and k as binary numbers

$$\begin{aligned} n &= 2^{\gamma-1}n_{\gamma-1} + 2^{\gamma-2}n_{\gamma-2} + \dots + n_0, \\ n &= 2^{\gamma-1}k_{\gamma-1} + 2^{\gamma-2}k_{\gamma-2} + \dots + k_0 \end{aligned} \quad (\text{A.8})$$

With the so factorized matrix, equation A.7 becomes

$$\begin{aligned} F(n_{\gamma-1}, n_{\gamma-2}, \dots, n_0) &= \sum_{k_0=0}^1 \sum_{k_1=0}^1 \dots \sum_{k_{\gamma-1}=0}^1 h(k_{\gamma-1}, k_{\gamma-2}, \dots, k_0) \\ &\quad \times W^{2^{\gamma-1}(n_0+k_{\gamma-1})} W^{(2n_1+n_0)2^{\gamma-2}k_{\gamma-2}} \dots \\ &\quad \times W^{2^{\gamma-1}n_{\gamma-1}+2^{\gamma-2}n_{\gamma-2}+\dots+n_0)k_0} \end{aligned} \quad (\text{A.9})$$

Equation A.9 can be separated into γ equations and can therefore be calculated with only $\frac{N\gamma}{2}$ multiplications and $N\gamma$ additions.

Appendix B

Detailed description of the timing software

The new class programmed for the FPGA card is called `FPGA_HI` and comprises two parts: The `FPGA_VI` which is translated to VHDL and initializes the card as a timing device and the `Host_VIs`, which are the communication layer to the user interface.

Host_VI

The `Host_VIs` consists of different subVIs:

- The constructor, which initializes the `FPGA` object and gives it a reference. It further initializes the `FPGA` card and reads the trigger and channel information from the *CS*-database, since the MM6 does not feature the possibility to send this information. This information as well as the reference to the `FPGA` card are written to an object instance data called `iattribute`.
- The `ProcCases`, where the actual code is executed, depending on the case called. The cases here are *default*, *LoadData*, *StartTG*, *StopTG*, *ScanX* and *ScanY*.
- The `ProcEvents`, which assigns the case to a received event.
- The `ProcPeriodic`, which periodically reads out the stop variable and the state of the `FPGA_VI`. If the state is *running* and the stop variable is 'false', nothing happens. As soon as the state is back to *loaded* or a stop was received, the command 'CycleFinished' is sent to the `MM6.vi` and the periodic interval is set back to infinity.
- The destructor, which closes the `FPGA` object and destroys the reference.

Now a detailed description of the single cases in `ProcCases` is given:

LoadData: The trigger and channel information consists of three parts: The number of triggers (integer), the number of channels (integer) and the individual trigger values (string of three digits numbers separated by blanks), which code the state of the trigger to be waited for.

The pattern data sent by the MM6.vi consist of 6 parts: An array of 26 double-precision numbers (time table) assigning a time interval in μs to every letter of the alphabet. An array of strings (pattern table) assigns a sequence of letters to each channel, where upper case letters stand for 'channel is on' and lower case letters for 'channel is off'. Since the MM6 has the possibility to use three different time and pattern tables, each has a so-called MemID (from 0-2). For each pattern table the time table can be assigned (TT2use). Then there is a string for ScanX and ScanY each. It consists of a letter and a number, stating which letter should be scanned using which time table (see also figure B.1).

The first action in *LoadData* is to check, whether number of triggers is greater than one. If not, enough 16 channel patterns are appended (maximum 48 channels, i.e. 3 pattern tables) to fit the number of channels wanted. In this case all pattern tables must use the same time table. After all tables have been appended, the timing sequence for the card is built.

If the number of triggers is greater one, the number of channels for the first trigger is checked. If this is 16, the timing sequence for this trigger built. If the number of channels is greater than 16, the corresponding number of pattern tables is appended, before the timing sequence is built. Each individual triggered timing sequence may use its own time table. After all timing sequences are built, they are stacked. Since they use a 32-bit nomenclature, it is checked, whether the channels assigned to each timing sequence are the first or the last 16 channels.

To build the timing sequence, first the appended or single pattern tables and the time tables are checked for completeness. Then the letters are translated to time durations. After this the time steps are calculated. Every time a channel changes its state, a time step is made. The result is put into two arrays. One is a 2-dimensional array of 32-bit integers, where each row codes 32 channels at a connector and each column a time step. The second is a 1-dimensional 32-bit integer array, where each entry codes a time step. The trigger information is in parallel fed to an array of 32-bit integers. The first 4 entries are: Number of triggers, trigger value, start and stop. The trigger value is read from an database, containing information on all *CS* classes. The trigger value is given as a string. The part of the string, that corresponds to the MemID of the active pattern is formatted to integer. Start and stop are calculated from the according length of the time step arrays (before stacking). The last value to enter the trigger array is the overall length of the timing sequence. The trigger array is filled with zeros to match the length of the time step array.

ptinj_killrf

Time1	Time2	Time3
A	Accumulation1	5.0
B	cooling	10000.0
C	offset	5.0
D	RFCoolon	1.0
E	DTpulse	6.3
F	PTinj	42.65
G	PTwait	2.0
H	Cleaning	10000.0
I	RF	100000.0
J	Pgate wait	25.8
K	TScope1	10.0
L		0.0
M	wait	100000.0

A..M

TG1	TG2	TG3
1	cooling	mA
2		
3	scope	mabZ
4	PTinj	MABFz
5	excitation	mabfghlz
6	PTej	MABfghZ
7		
8	cleaning	mabfghiz
9	buncherEject	mabZ
10		
11	PulsedDT	mabeZ
12	KillRF	MAB
13	PGate	MABJoZZ
14		
15		MABfghZz
16		

ScanX ScanY

Save Cancel

Use time table
☒ 1 ☐ 2 ☐ 3

Figure B.1: Screenshot of the timing information in the MM6.cpp. The time table is marked in blue, the pattern table in red. Green is the scan information and light blue the information, which time table is to be used. A single pattern corresponds to a column in the pattern table, while one time step corresponds to the time coded for a letter.

If the time step array is shorter than four entries, it is lengthened with zeros. The final trigger array is loaded to the card together with the timing sequence.

The timing sequence arrays (time step array and pattern array) are loaded to the FPGA_VI stepwise, since the implementation of arrays on the FPGA card is too costly in terms of consumed gates. This stepwise loading uses a hand-shake mechanism. The case *LoadData* sets the boolean for the command 'reload' as true and waits for the state on the FPGA_VI to change to *load*. Then the first elements of the trigger array, the time array and the rows of the 2-D pattern array are written to the FPGA_VI. That again sets the hand-shake boolean to true as long as it processes the received data. The Host_VI waits for this boolean to turn to false again, before sending the next data set. When the last element of the arrays is reached, the Host_VI sets the boolean

'last element' as true, and the pattern loading stops. Before leaving the case *LoadData*, the error cluster of the state machine is read out.

ScanX/Y: At calling *ScanX/Y*, the MM6.vi sends a new time value to the Host_VI. The information which letter is to be scanned, using which time table is coded in the string for ScanX or ScanY, respectively. The corresponding time value (read from the iattribute) is compared to the new time value. If the values differ, the new value replaces the old value in the time table, which then is written back to the iattribute. Now the FPGA card is reloaded using the changed time table to build the new timing sequence. After this the MM6.vi automatically calls the case *StartTG*. That is repeated until all scan steps have been processed.

StartTG: This case sets the periodic interval for the ProcPeriodic to 1 ms and then sends the command 'execute' to the FPGA_VI. In parallel it sets the global stop variable to 'false'.

StopTG: Here the command 'stop' is sent to the FPGA_VI and the global stop variable is set to 'true'.

FPGA_VI

At the moment only two connectors of the FPGA card are initialized with five ports each, since we do not need more than 64 channels. The last port at connector 0 is defined as 8-bit trigger input. On the FPGA four memories and nine FIFOs are defined. There is one memory for each of the two connectors, one for the time steps and one for the trigger information. The nine FIFOs are distributed one for each port and one for the time steps. The memories and the time FIFO have a depth of 1028 unsigned 32-bit integers, the port FIFOs have a depth of 1028 unsigned 8-bit integers.

The state machine controlling the pattern execution is realized as a case structure with each case corresponding to one state. Only the default state can react to commands from outside. Now a detailed description of the states follows:

loaded: By reading out the corresponding controls one after the other, it is checked if any command has been given or if an error has occurred. If this is the case the corresponding state is set and called. If this is not the case, the state *loaded* calls itself again.

load: On the command 'reload' this state is called. Here a loop receives the data from the Host_VI. When the first data are received, the hand-shake boolean is set to 'true', indicating, that no new data can be received. The received data are then written to the according memories on the FPGA card.

After this is done, the boolean is set back to 'false' and new data can be received. When a 'true' for the last element is received, the loading loop stops after writing this element and the default state is called, if now error has occurred. Otherwise the state *error* is called.

running: On the command 'execute' the state *running* is called. This is divided in three steps. In the first step, the overall timing sequence length is read out and the data from the memories are written to the corresponding FIFOs. In this process, the 32-bit integers for the channel states for each connector are split into four 8-bit integers for the corresponding ports on the corresponding connector, which are written to the FIFOs. In the second step the trigger information is read out and the pattern execution started. If a trigger is to be expected, the program waits until the specific trigger is received by checking the 8-bit input. Then a loop starts, which first initializes all channels as zero and reads out the first FIFO element, this is written in the second step to the according port. The value read from the time FIFO sets the waiting time after which the next loop cycle is started. This happens as long as either the number of loop cycles equals the length - in time steps - of the active timing sequence, or a 'stop' is received, or one of the FIFOs is empty. Then all channels are set back to zero. In step three the next state is called. *error*, if an error occurred, otherwise *loaded*.

error: If an error occurred somewhere in the state machine, this state is called. After a waiting time of 10 ms, which is enough for the error to be read by the Host_VI, the error cluster is set back to 'no error' and the state *loaded* is called.

Bibliography

- [Alo07] J.A. Alonso Otamendi, *Development of an Experiment for Ultrahigh-Precision g -Factor Measurements in a Penning-Trap Setup*, PhD Thesis, Mainz (2007).
- [Amo04] M. Amoretti et al., *The ATHENA antihydrogen apparatus*, Nucl. Meth. Phys. Res. A **518** (2004) 679.
- [Ant74] N.M. Antoneva, A.V. Barkov, A.V. Zolotavin, P.P.Dmitriev, S.V. Kamynov, G.S. Katykhin, E.T. Kondrat, N.I. Krasnov, Y.N. Podkopaev, V.A. Sergienko and V.I. Fominykh *The Decay of ^{95}Tc* , Izv. Akad. Nauk. SSSR, Ser. Fiz. **38** (1974) 48.
- [Arn99] M. Arnould, K. Takahashi, *Nuclear astrophysics*, Rep. Prog. Phys. **62** (1999) 395.
- [Ash70] J. Ashkenazi, E. Friedman, D. Nir and J. Zioni, *Properties of $^{96,98}\text{Rh}$ from the $^{96,98}\text{Ru}(p,n)$ Reaction*, Nuc. Phys. A **158** (1970) 146.
- [Aud03a] G. Audi, O. Bersillon, J. Blachot, A. H. Wapstra, and C. Thibault, *The NUBASE evaluation of nuclear and decay properties*, Nucl. Phys. A **729** (2003) 3.
- [Aud03b] G. Audi, A. H. Wapstra, and C. Thibault, *The AME2003 atomic mass evaluation (II). Tables, graphs and references*, Nucl. Phys. A **729**, (2003) 337.
- [Äys73] J. Äystö, J. Honkanen, W. Trzaska, K. Eskola, K. Vierinen and S. Messelt, *Features of the beta decay of ^{93}Ru to proton emitting states in ^{93}Tc* , Nucl. Phys. A **404** (1973) 1.
- [Bal71] J.B. Ball, *Studies of ^{95}Ru and ^{94}Ru with the $^{96}\text{Ru}(p,d)$ and (p,t) reactions*, Nuc. Phys. A **160** (1971) 225.
- [Ban94] V. Banerjee, A. Banerjee, G.S.N. Murthy, R.P. Sharma, S.K. Pardha Saradhi and A. Chakrabarti, *Decay of ^{98}Rh* , Phys. Rev. C **49** (1994) 1221.
- [Bar08] W. Barth, *The Injector Systems for the FAIR Project*, Proc. of LINAC2008, Vancouver, 2008.

- [Bec04] D. Beck, K. Blaum, H. Brand, F. Herfurth, S. Schwarz *A new control system for Isoltrap.*, Nucl. Instr. and Meth. A **527** (2004) 567.
- [Beh09] Behlke Power Electronics online catalogue, <http://www.behlke.de> (2009).
- [Bei00] T. Beier, *The g_j factor of a bound electron and the hyperfine structure splitting in hydrogelike ions*, Phys. Rep. **339** (2000) 79.
- [Bei02] T. Beier, H. Häffner, N. Hermanspahn, S.G. Karshenboim, H.-J. Kluge, W. Quint, S. Stahl, J. Verdú, G. Werth, *New Determination of the Electron's Mass*, Phys. Rev. Lett. **88** (2002) 011603.
- [Bei03] T. Beier, P. Indelicato, V.M. Shabaev, V.A. Yerokhin, *New value for the electron's mass - theoretical foundations*, J. Phys. B **36** (2003) 1019.
- [Bei03a] T. Beier, *Determination of the electron's mass from g -factor experiments on $^{12}\text{C}^{5+}$ and $^{16}\text{O}^{7+}$* Nucl. Instr. Meth. B **205** (2003) 15.
- [Bla06] K. Blaum, *High-accuracy mass spectrometry with stored ions*, Phys. Rep. **425** (2006) 1.
- [Blo09] M. Block, to be published.
- [Bol06] G. Bollen, D. Davies, M. Facina, J. Huikari, E. Kwan, P. A. Lofy, D. J. Morrissey, A. Prinke, R. Ringle, J. Savory, P. Schury, S. Schwarz, C. Sumithrarachchi, T. Sun, and L. Weissman, *Experiments with Thermalized Rare Isotope Beams from Projectile Fragmentation: A Precision Mass Measurement of the Superallowed β Emitter ^{38}Ca* , Phys. Rev. Lett. **96** (2006) 152501.
- [Bra36] N.E. Bradbury and R.A. Nielsen, *Absolute Values of the Electron Mobility in Hydrogen*, Phys. Rev. **49** (1936) 388.
- [Bra99] M.P. Bradley, J.V. Porto, S. Rainville, J.K. Thompson, D.E. Pritchard, *Penning Trap Measurements of the Masses of ^{133}Cs , $^{85,87}\text{Rb}$, and ^{23}Na with Uncertainties ≤ 0.2 ppb*, Phys. Rev. Lett. **83** (1999) 4510.
- [Bri96] J.-P. Briand, S. Thuriez, G. Giardino, G. Borsoni, M. Froment, M. Ed-drief, C. Sébenne, *Observation of Hollow Atoms or Ions above Insulator and Metal Surfaces*, Phys. Rev. Lett. **77** (1996) 1452.
- [Bri97] E.O. Brigham, *FFT-Anwendungen*, Oldenbourg, München (1997).
- [Bro86] L.S. Brown, G. Gabrielse, *Geonium theory: Physics of an electron or ion in a Penning trap*, Rev. Mod. Phys. **58** (1986) 233.
- [Cha07] A. Chaudhuri, *Carbon-cluster mass calibration at SHIPTRAP*, PhD thesis, Greifswald, (2007).

- [Coo65] J. W. Cooley and J. W. Tukey, *An Algorithm for the Machine Calculation of Complex Fourier Series*, Math. Comput. **19** **297** (1965).
- [Cre65] T. Cretzu, K. Hohmuth and J. Schintlmeister *Der Zerfall von Tc^{95m}* , Nuc. Phys. **70** (1965) 129.
- [Dah04] L. Dahl, W. Barth, Th. Beier, W. Vinzenz, C. Kitegi, U. Ratzinger, A. Schempp, *The HITRAP-Decelerator for Heavy Highly-Charged Ions*, JACoW Conf Proc. of EPAC 2004, Lübeck (2004) 39.
- [Dah06] L. Dahl, W. Barth, Th. Beier, W. Vinzenz, C. Kitegi, U. Ratzinger, A. Schempp, *The HITRAP Decelerator Project at GSI*, JACoW Conf Proc. of EPAC 2006, Edinburgh (2006) 1568.
- [Dam63] R.A. Damerow, R.R. Ries and W.H. Johnson jr., *Atomic Masses from Ruthenium to Xenon*, Phys. Rev. **132** (1963) 1673.
- [Deh58] H.G. Dehmelt, *Spin Resonance of Free Electrons Polarized by Exchange Collisions*, Phys. Rev. **109** (1958) 381.
- [Deh67] H.G. Dehmelt, *Radio-frequency spectroscopy of stored ions. I. Storage*, Adv. At. Mol. Phys. **3** (1967) 53.
- [Deh68] H.G. Dehmelt, F.L. Walls, *"Bolometric" technique for the rf-spectroscopy of stored ions*, Phys. Rev. Lett. **21** (1968) 127.
- [Deh69] H.G. Dehmelt, *Radio-frequency spectroscopy of stored ions. II. Spectroscopy*, Adv. At. Mol. Phys. **5** (1969) 109.
- [Dör00] R. Dörner, V. Mergel, O. Jagutzki, L. Spielberger, J. Ullrich, R. Moshammer, H. Schmidt-Böcking, *Cold Target Recoil Ion Momentum Spectroscopy: a 'momentum microscope' to view atomic collision dynamics*, Phys. Rep. **330** (2000) 95.
- [DRE08] DREEBIT website, <http://www.dreebit.com> (2008).
- [Dub99] D.H.E. Dubin, T.M. O'Neil, *Trapped nonneutral plasmas, liquids, and crystals (the thermal equilibrium states)*, Rev. Mod. Phys. **71** (1999) 87.
- [Dyc87] R.S. Van Dyck, P.B. Schwinberg, H.G. Dehmelt, *New High-Precision Comparison of Electron and Positron g Factors*, Phys. Rev. Lett. **59** (1987) 26.
- [Dyc04] R. S. Van Dyck, S. L. Zafonte, S. Van Liew, D. B. Pinegar, and P. B. Schwinberg *Ultraprecise Atomic Mass Measurement of the α Particle and ^4He* , Phys. Rev. Lett. **92** (2004) 220802.
- [Ear42] S. Earnshaw, *On the Nature of the Molecular Forces which Regulate the Constitution of the Luminiferous Ether*, Trans. Camb. Phil. Soc. **7** (1842) 97.

- [Eas53] H.T. Easterday and H.A. Medicus, *Isomeric Transitions in Tc^{93} and Tc^{96}* , Phys. Rev. **89** (1953) 752.
- [Eli07a] S. Eliseev, M. Block, A. Chaudhuri, F. Herfurth, H.-J. Kluge, A. Martin, C. Rauth, G. Vorobjev, *Octupolar excitation of ions stored in a Penning trap mass spectrometer A study performed at SHIPTRAP*, Int. J. of Mass Spec. **262** (2007) 45.
- [Eli07b] S. Eliseev, M. Block, A. Chaudhuri, Z. Di, D. Habs, F. Herfurth, H.-J. Kluge, J. B. Neumayer, W. R. Plass, C. Rauth, P. G. Thirolf, G. Vorobjev, Z. Wang, *Extraction efficiency and extraction times of the SHIPTRAP gas-filled stopping cell*, Nucl. Instr. and Meth. B **258** (2007) 479.
- [Fau79] W. Faust, K. Güttner, G. Münzenberg, S. Hofmann, W. Reisdorf, K. H. Schmidt and P. Armbruster, *The Efficiency of the Velocity Filter SHIP for Unslowed Evaporation Residues*, Nucl. Instr. and Meth. **166**, 397 (1979).
- [Fra87] B. Franzke, *The heavy ion storage and cooler ring project ESR at GSI*, Nucl. Instr. Meth. B **24** (1987) 18.
- [Fri91] J. Friedrich, A. Schempp, H. Deitinghoff, U. Bessler, H. Klein, R. Veith, N. Angert, J. Klabunde, *Properties of the GSI HLI-RFQ Structure*, PAC Conf. Proc. (1991) 3044.
- [Gab84] G. Gabrielse, F.C. Mackintosh, *Cylindrical Penning traps with orthogonalized anharmonicity compensation*, Int. J. Mass Spec. Ion Proc. **57** (1984) 1.
- [Gab89] G. Gabrielse, L. Haarsma, S.L. Rolston, *Open-endcap Penning traps for high precision experiments*, Int. J. Mass Spec. Ion Proc. **88** (1989) 319.
- [Gab99a] G. Gabrielse, D.S. Hall, T. Roach, P. Yesley, A. Khabbaz, J. Estrada, C. Heimann, H. Kalinowsky, *The ingredients of cold antihydrogen: Simultaneous confinement of antiprotons and positrons at 4 K*, Phys. Lett. B **455** (1999) 311.
- [Gab99b] G. Gabrielse, A. Khabbaz, D. S. Hall, C. Heimann, H. Kalinowsky, and W. Jhe, *Precision Mass Spectroscopy of the Antiproton and Proton Using Simultaneously Trapped Particles*, Phys. Rev. Lett. **82** (1999) 3198.
- [Gab06] G. Gabrielse, D. Hanneke, T. Kinoshita, M. Nio, B. Odom, *New Determination of the Fine Structure Constant from the Electron g -value and QED*, Phys. Rev. Lett. **97** (2006) 030802.
- [Gab08] G. Gabrielse, *The true cyclotron frequency for particles and ions in a Penning trap*, Int. J. Mass Spec. **279** (2008) 107.

- [Gas00] C. Gaspar, M. Dönszelmann and P. Charpentier, *DIM, a Portable, Light Weight Package for Information Publishing, Data Transfer and Inter-process Communication*, presented at: International Conference on Computing in High Energy and Nuclear Physics (Padova, Italy, 1-11 February 2000).
- [Grä80] G. Gräff, H. Kalinowsky and J. Traut, *A direct determination of the proton electron mass ratio*, Z. Phys. A **297** (1980) 35.
- [Gre00] R.G. Greaves, C.M. Surko, *Inward Transport and Compression of a Positron Plasma by a Rotating Electric Field*, Phys. Rev. Lett. **85** (2000) 1883.
- [Gök80] H. Göktürk, N.K. Aras, P. Fettweis, P. del Marmol, J. Vanhorenbeeck and K.Cornelis, *The Decay of ^{97}Pd* , Nuc. Phys. A **344** (1980) 1.
- [Häf00] H. Häffner, T. Beier, N. Hermanspahn, H.-J. Kluge, W. Quint, S. Stahl, J. Verdú, G. Werth, *High-accuracy Measurements of the Magnetic Moment Anomaly of the Electron Bound in Hydrogenlike Carbon*, Phys. Rev. Lett. **85** (2000) 5308.
- [Häf03] H. Häffner, T. Beier, S. Djekić, N. Hermanspahn, H.-J. Kluge, W. Quint, S. Stahl, J. Verdú, T. Valenzuela, G. Werth, *Double Penning trap technique for precise g factor determinations in highly charged ions*, Eur. Phys. J. D **22** (2003) 163.
- [Ham64] J.H. Hamilton, K.E.G. Löbner, A.R. Sattler and R. van Lieshout *The energy levels in ^{94}Mo populated by the decays of ^{94}Tc and $^{94}\text{Tc}^m$* , Physica **30** (1964) 1802.
- [Han08] D. Hanneke, S. Fogwell, G. Gabrielse, *New Measurement of the Electron Magnetic Moment and the Fine Structure Constant*, Phys. Rev. Lett. **100** (2008) 120801.
- [Har01] J.C. Hardy, I.S. Towner, *Standard-Model Tests with Superallowed β -Decay: An Important Application of Very Precise Mass Measurements*, Hyp. Int. **132** (2001) 115.
- [Har05] J. C. Hardy and I. S. Towner, *Superallowed $0^+ \rightarrow 0^+$ nuclear β decays: A critical survey with tests of the conserved vector current hypothesis and the standard model*, Phys. Rev. C **71** (2005) 055501.
- [Her05] F. Herfurth, T. Beier, L. Dahl, S. Eliseev, S. Heinz, O. Kester, H.-J. Kluge, C. Kozhuharov, G. Maero, W. Quint, the HITRAP collaboration, *Highly charged ions at rest: the HITRAP project at GSI*, in: Y. Yamazaki, M. Wada, *Physics with ultra slow antiproton beams*, AIP Conf. Proc. **793** (2005) 278.

- [Her06] F. Herfurth, T. Beier, L. Dahl, S. Eliseev, S. Heinz, O. Kester, C. Kozhuharov, G. Maero, W. Quint, *Precision measurements with highly charged ions at rest: the HITRAP project at GSI*, Int. J. Mass Spec. **251** (2006) 266.
- [Her06a] F. Herfurth, *The fast switch for the Cooler Trap entrance electrode*, GSI internal report (2006).
- [Hof00] S. Hofmann and G. Münzenberg. *The discovery of the heaviest elements*, Rev. Mod. Phys. **72**, 733 (2000).
- [Hof06] B. Hofmann, A. Schempp, O. Kester, *The HITRAP RFQ decelerator at GSI*, JACoW Proc. of EPAC 2006, Edinburgh (2006) 1586.
- [Hof08] B. Hofmann, *Konstruktion und Aufbau einer kompakten RFQ-Spiral-Struktur zum Abbremsen hochgeladener Schwerionenstrahlen für das HITRAP-Projekt der GSI*, PhD thesis, Frankfurt (2008).
- [Huy02] M. Huyse, M. Facina, Y. Kudryavtsev and P. Van Duppen, *Intensity limitations of a gas cell for stopping, storing and guiding of radioactive ions* Nucl. Instr. and Meth. B **187**, 535 (2002).
- [Ich01] T. Ichioka, *Development of intense beam of ultracold antiprotons*, PhD thesis, Tokio (2001).
- [Ixy05] IXYS, datasheet *DGS 13-025CS, Gallium Arsenide Schottky Rectifier (2005)*, IXYS webpage (2009).
- [Kaj99] D. Kajfez, *Q factor measurements, analog and digital*, pdf-tutorial on <http://www.ee.olemiss.edu/darko/darko.html> (present in 2009), (1999)
- [Kel03] A. Kellerbauer, K. Blaum, G. Bollen, F. Herfurth, H.-J. Kluge, M. Kuckein, E. Sauvan, C. Scheidenberger, and L. Schweikhard, *From Direct to Absolute Mass Measurements: A Study of the Accuracy of ISOLTRAP*, Eur. Phys. J. D **22**, 53 (2003).
- [Kes06] O. Kester et al., *Proposal: HITRAP decelerator commissioning*, GSI internal document (2006).
- [Kes06a] O. Kester, W. Barth, L. Dahl, F. Herfurth, M. Kaiser, H.-J. Kluge, C. Kozhuharov, W. Quint, B. Hofmann, U. Ratzinger, A. Sauer, A. Schempp, *Deceleration of highly charged ions for the HITRAP project at GSI*, JACoW Proc. of LINAC 2006, Knoxville (2006) 189.
- [Ket06] J. Ketelaer, *Development of a non-destructive Fourier Transform-Ion Cyclotron Resonance detection system for singly charged ions in a cryogenic Penning trap*, Diploma thesis, Mainz (2006).
- [Khe98] H. Khemliche, T. Schlathölter, R. Hoekstra, R. Morgenstern, S. Schippers, *Hollow Atom Dynamics on LiF Covered Au(111): Role of the Surface Electronic Structure*, Phys. Rev. Lett. **81** (1998) 1219.

- [Kie89] P. Kienle, *Status of the SIS/ESR-Project at GSI*, GSI Preprint, March 1989.
- [Kin06] T. Kinoshita, M. Nio, *Improved α^4 term of the electron anomalous magnetic moment*, Phys. Rev. D **73** (2006) 013003.
- [Klu07] H.-J. Kluge, W. Quint, D.F.A. Winters, *Atomic physics experiments with trapped and cooled highly charged ions*, J. Phys.: Conf. Series **58** (2007) 9.
- [Klu07a] H.-J. Kluge, Y. Novikov, *New Promises for the Determination of the Neutrino Mass? A Brainstorm Meeting at GSI, Darmstadt*, Nuc. Phys. News **48** (2007) 17.
- [Kol04] V. S. Kolhinen, S. Kopecky, T. Eronen, U. Hager, J. Hakala, J. Huikari, A. Jokinen, A. Nieminen, S. Rinta-Antila, J. Szerypo and J. Äystö, *JYFLTRAP: a cylindrical Penning trap for isobaric beam purification at IGISOL*, Nucl. Instr. and Meth. A **528**, 776 (2004).
- [Kur05] N. Kuroda, H. A. Torii, K.Y. Franzen, Z. Wang, S. Yoneda, M. Inoue, M. Hori, B. Juhász, D. Horváth, H. Higaki, A. Mohri, J. Eades, K. Komaki, Y. Yamazaki, *Confinement of a Large Number of Antiprotons and Production of an Ultraslow Antiproton Beam*, Phys. Rev. Lett. **94** (2005) 023401.
- [Lem05] C. Lemell, X.M. Tong, K. Tokesi, L. Wirtz, J. Burgdörfer, *Electron emission from surfaces induced by HCI and lasers*, Nucl. Instr. Meth. Phys. Res. B **235** (2005) 425.
- [Lit05] Y. Litvinov, H. Geissel, T. Radon, F. Attallah, G. Audi, K. Beckert, F. Bosch, M. Falch, B. Franzke, M. Hausmann, M. Hellström, T. Kerscher, O. Klepper, H.-J. Kluge, C. Kozhuharov, K.E.G. Löbner, G. Münzenberg, F. Nolden, Y.N. Novikov, W. Quint, Z. Patyk, H. Reich, C. Scheidenberger, B. Schlitt, M. Steck, K. Sümmerer, L. Vermeeren, M. Winkler, T. Winkler and H. Wollnik, *Mass measurements of cooled neutron-deficient bismuth projectile fragments with time-resolved Schottky mass spectrometry at the FRS-ESR facility*, Nuc. Phys. A **756** (2005) 3.
- [Lom01] A.M. Lombardi, W. Pirkel, and Y. Bylinsky, *First operating experience with the CERN decelerating RFQ for antiprotons*, Proc. PAC **585** (2001).
- [Lun03] D. Lunney, J. M. Pearson, and C. Thibault, *Recent trends in the determination of nuclear masses*, Rev. Mod. Phys. **75** (2003) 1021.
- [Mac59] W.W. Macalpine, R.O. Schildknecht, *Coaxial resonators with helical inner conductor*, Proc. IRE **47**, (1959) 2099.
- [Mae08] G. Maero, *Cooling of highly charged ions in a Penning trap for HI-TRAP*, PhD thesis, Heidelberg (2008).

- [Mag99] Magnex Scientific LTD, *Technical Specification*, (1999).
- [Maj04] F.G. Major, V.N. Gheorghe, G. Werth, *Charged Particle Traps*, Springer, New York (2004).
- [Mal75] J.H. Malmberg, J.S. deGrassie, *Properties of Nonneutral Plasma*, Phys. Rev. Lett. **35** (1975) 577.
- [Man86] R. Mann, *Total One-Electron Capture Cross Sections for Ar^{q+} and I^{q+} in Slow Collisions on H_2 and He*, Z. Phys. D **3** (1986) 85.
- [Mar94] R.E. Marrs, S.R. Elliott, D.A. Knapp, *Production and Trapping of Hydrogenlike and Bare Uranium Ions in an Electron Beam Ion Trap*, Phys. Rev. Lett. **72** (1994) 4082.
- [McD02] J.W. McDonald, R.W. Bauer, D.H.G. Schneider, *Extraction of highly charged ions (up to 90+) from a high-energy electron-beam ion trap*, Rev. Sc. Instr. **73** (2002) 30.
- [McP73] M.R. McPherson and F. Gabbard *Excited States of ^{94}Tc Studied Through the Enhancement of Neutron and Gamma-Ray Yields from the $^{94}Mo(p,n)^{94}Tc$ Reaction at Isobaric Analog Resonances*, Phys. Rev. C **7** (1973) 2097.
- [Moh98] P.J. Mohr, G. Plunien, G. Soff, *QED corrections in heavy atoms*, Phys. Rep. **293** (1998) 227.
- [Moh08] P.J. Mohr, B.N. Taylor, D.B. Newell, *CODATA recommended values of the fundamental physical constants: 2006*, Rev. Mod. Phys. **80** (2008) 633.
- [Muk08] M. Mukherjee, D. Beck, K. Blaum, G. Bollen, J. Dilling, S. George, F. Herfurth, A. Herlert, A. Kellerbauer, H. -J. Kluge, S. Schwarz, L. Schweikhard and C. Yazidjian, *ISOLTRAP: An on-line Penning trap for mass spectrometry on short-lived nuclides*, Euro. Phys. J. A, **35** (2008) 1
- [Mün79] G. Münzenberg, W. Faust, S. Hofmann, P. Armbruster, K. Güttner and H. Ewald *The velocity filter SHIP, a separator of unslowed heavy ion fusion products.*, Nucl. Instr. Meth. **161**, 65 (1979).
- [Ner07] H. Nersisyan, C. Toepffer, G. Zwicknagel, *Interactions Between Charged Particles in a Magnetic Field*, Springer, Berlin-Heidelberg (2007).
- [Neu06] J. B. Neumayer, L. Beck, D. Habs, S. Heinz, J. Szerypo, P. G. Thirolf, V. Varentsov, F. Voit, D. Ackermann, D. Beck, M. Block, Z. Di, S. A. Eliseev, H. Geissel, F. Herfurth, F. P. Heberger, S. Hofmann, H.-J. Kluge, M. Mukherjee, G. Münzenberg, M. Petrick, W. Quint, S. Rahaman, C. Rauth, D. Rodriguez, C. Scheidenberger, G. Sikler, Z. Wang, C. Weber, W. R. Pla, M. Breitenfeldt, A. Chaudhuri, G. Marx, L. Schweikhard,

- A. F. Dodonov, Y. Novikov and M. Suhonen, *The ion-catcher device for SHIPTRAP*, Nucl. Instr. and Meth. B **244**, 489 (2006).
- [NI09] www.ni.com, product description FPGA module (2009).
- [Nol80] E. Nolte, G. Korschinek, and U. Heim, *Investigation of Very Neutron Deficient Ru and Rh Nuclei with the Help of $(^{40}\text{Ca};yp+\alpha\gamma)$ Reactions*, Z. Phys. A **298** (1980) 191.
- [Nov09] Y. Novikov, private communication (2009).
- [Odo06] B. Odom, D. Hanneke, B. D’Urso, G. Gabrielse, *New Measurement of the Electron Magnetic Moment Using a One-Electron Quantum Cyclotron*, Phys. Rev. Lett. **97** (2006) 030801.
- [Ohy74] S. Ohya *Nuclear Structure Studies of ^{97}Ru from the Decay of $^{97g,m}\text{Rh}$* , Nucl. Phys. A **235** (1974) 361.
- [Oxo80] K. Oxorn, B. Singh and S.K. Mark, *The Decay of 26-s and 71-s ^{94}Rh Isomers*, Z. Phys. A **294** (1980) 389.
- [Pac96] K. Pachucki, D. Leibfried, M. Weitz, A. Huber, W. König, T. W. Hänsch, *Theory of the energy levels and precise two-photon spectroscopy of atomic hydrogen and deuterium*, J. Phys. B **29** (1996) 177.
- [Pac98] K. Pachucki, *Quantum electrodynamics of weakly bound systems*, Hyp. Int. **114** (1998) 155.
- [Pan01] V.S. Pandit, P.R. Sarma, R. K. Bhandari, *Modification of a double drift bunching beam system to get the efficiency of a six harmonic buncher*, Proc. of Cyclotron and their Applications 2001, AIP Conf. Proc. **600** (2001) 452.
- [Pie49] J.R. Pierce, *Theory and Design of Electron Beams*, D. Van Nostrand Co., New York (1949).
- [Rai97] H. Raimbault-Hartmann, D. Beck, G. Bollen, M. König, H.-J. Kluge, E. Schark, J. Stein, S. Schwarz and J. Szerypo, *A Cylindrical Penning Trap for Caspture, Mass Selective Cooling and Bunching of Radioactive Ion Beams*, Nucl. Instr. and Meth. B **126**, 378 (1997).
- [Rao79] M.N. Rao, C.P. Massolo, S. Fortier, and J.M. Maison, *Nuclear Structure of ^{94}Tc* , Phys. Rev. C **20** (1979) 139.
- [Rau06] C. Rauth *Direct mass measurements beyond the proton dripline*, PhD thesis, Heidelberg (2006).
- [Rod03] D. Rodriguez Rubiales, *A RFQ Buncher for Accumulation and Cooling of Heavy Radionuclides at SHIPTRAP and High Precision Measurements of Unstable Kr Isotopes at ISOLTRAP*, PhD Thesis, Valencia (2003).

- [Ryk85] K. Rykaczewski, I.S. Grant, R. Kirchner, O. Klepper, V.T. Koslowsky, P.O. Larsosn, E. Nolte, G. Nyman, E. Roeckl, D. Schardt, L. Spanier, P. Tidemand-Petersson, E.F. Zganjar and J. Zylicz *The Gamow-Teller Transitions in the $^{96}\text{Pd} \rightarrow ^{96}\text{Rh}$ Decay*, Z. Phys. A **322** (1985) 322.
- [Sav91] G. Savard, St. Becker, G. Bollen, H.-J. Kluge, R. B. Moore, Th. Otto, L. Schweikhard, H. Stolzenberg and U. Wiess, *A new cooling technique for heavy ions in a Penning trap*, Phys. Lett. A **158** (1991) 247.
- [Sch84] A.S. Schlachter, *Charge-Changing-Collisions*, Proc. of the 10th Int. Cyclotron Conf. (1984) 563.
- [Sch91] L. Schweikhard, *Theory of quadrupole detection Fourier Transform-Ion Cyclotron Resonance*, Int. J. Mass. Spectrom. Ion Process. **107**, 281 (1991).
- [Sch98] H. Schatz, A. Aprahamian, J. Görres, M. Wiescher, T. Rauscher, J. F. Rembges, F.-K. Thielemann, B. Pfeiffer, P. Möller, K.-L. Kratz, H. Herndl, B. A. Brown, and H. Rebel *rp-Process Nucleosynthesis at Extreme Temperature and Density Conditions*, Phys. Rep. **294**, (1998) 167.
- [Sch01] H. Schatz, A. Aprahamian, V. Barnard, L. Bildsten, A. Cumming, M. Ouellette, T. Rauscher, F.-K. Thielemann, and M. Wiescher, *End Point of the rp Process on Accreting Neutron Stars*, Phys. Rev. Lett. **86** (2001) 3471.
- [Sch06a] H. Schatz, *The importance of nuclear masses in the astrophysical rp-process*, Int. J. Mass Spec. **251** (2006) 293.
- [Sch06b] L. Schweikhard and G. Bollen (Ed.), *Ultra-Accurate Mass Determination and Related Topics*, Int. J. Mass Spectrom. **251** (2006) 85.
- [See98] P. Seelig, S. Borneis, A. Dax, T. Engel, S. Faber, M. Gerlach, C. Holbrow, G. Huber, T. Kühl, D. Marx, K. Meier, P. Merz, W. Quint, F. Schmitt, M. Tomaselli, L. Völker, H. Winter, M. Würtz, K. Beckert, B. Franzke, F. Nolden, H. Reich, M. Steck, T. Winkler, *Ground State Hyperfine Splitting of Hydrogenlike $^{207}\text{Pb}^{81+}$ by Laser Excitation of a Bunched Ion Beam in the GSI Experimental Storage Ring*, Phys. Rev. Lett. **81** (1998) 4824.
- [Sha06] V.M. Shabaev, *g-Factor of Heavy Ions: A New Access to the Fine Structure Constant* Phys. Rev. Lett. **96** (2006) 253002.
- [Shi82] K. Shima, T. Ishihara, T. Mikumo, *Empirical Formula for the Average Equilibrium Charge-State of Heavy Ions Behind Various Foils*, Nucl. Instr. Meth. **200** (1982) 605.
- [Sie08] Datasheet for the n-channel dual gate GaAs MESFET CF739 from Siemens: <http://www.datasheetcatalog.com>

- [Sik03] G. Sikler, *Massenspektrometrie kurzlebiger Sr- und Sn-Isotope und Aufbau der SHIPTRAP-Penningfallen*, PhD Thesis, Heidelberg (2003).
- [Sta98] S. Stahl, *Aufbau eines Experimentes zur Bestimmung elektronischer g-Faktoren einzelner wasserstoffähnlicher Ionen*, PhD thesis, Mainz (1998).
- [Sta07] S. Stahl, private communication (2007).
- [Sta08] S. Stahl, private communication (2008).
- [Ste04] M. Steck, K. Beckert, P. Beller, B. Franczak, B. Franzke, F. Nolden, *Improved Performance of the Heavy Ion Storage Ring ESR*, JACoW Proc. of EPAC 2004, Lucerne (2004) 1168.
- [TDR03] T. Beier, L. Dahl, H.-J. Kluge, C. Kozhuharov, W. Quint, *HITRAP Technical Design Report*, GSI Darmstadt (2003).
- [Thy09] Datasheet for ELmedur X at Thyssenduro website: <http://www.thyssenduro.de>
- [Ulm09] S. Ulmer, private communication (2009).
- [Ull03] J. Ullrich, R. Moshhammer, A. Dorn, R. Dörner, L. Ph. H. Schmidt, H. Schmidt-Böcking, *Recoil-ion and momentum spectroscopy: reaction-microscopes*, Rep. Prog. Phys. **66** (2003) 1463.
- [Ver04] J. Verdú, S. Djekić, W. Quint, S. Stahl, T. Valenzuela, M. Vogel, G. Werth, *Electronic g Factor of Hydrogenlike Oxygen $^{16}\text{O}^{7+}$* , Phys. Rev. Lett. **92** (2004) 093002.
- [Vog05] M. Vogel, D.F.A. Winters, D.M. Segal, R.C. Thompson, *Proposed precision spectrometer for trapped, highly charged ions*, Rev. Sci. Instr. **76** (2005) 103102.
- [Wal99] P.M. Walker, G. Dracoulis, *Energy traps in atomic nuclei*, Nature **399**(1999) 35.
- [Wal06] P.M. Walker, *Nuclear isomers: stepping stones to the unknown*, AIP Conf. Proc. **819**(2006) 16.
- [Wan98] T.P. Wangler, *Principles of RF Linear Accelerators*, John Wiley and Sons, New York (1998).
- [Wap03] A. H. Wapstra, G. Audi, and C. Thibault, *The AME2003 atomic mass evaluation (I). Evaluation of the input data, adjustment procedures.*, Nucl. Phys. A **729**, (2003) 129.
- [Wei75] C. Weiffenbach, S.C. Gujrathi and J.K.P. Lee, *The Decay of ^{95}Rh to Levels of ^{95}Ru* , Can. Jour. Phys. **53** (1975) 101.

- [Wer08] J. Werner, *Flugzeitmassenspektrometrie und Designstudie fr einen neuen RF-Quadrupol-Buncher bei SHIPTRAP*, Bachelor thesis, Gieen, 2008.
- [Woo97] P.J. Woods and C.N. Davids, *Nuclei Beyond the Proton Dripline*, Ann. Rev. Nucl. Part. Sci. **47** (1997) 541.
- [Zie07] F. Ziegler, private communication (2007).
- [Zis73] M.S. Zisman, F.D. Becchetti, B.G. Harvey, D.G. Kovar, J. Mahoney and J.D. Sherman, *Heavy-Ion-Induced Single-Nucleon Transfer Reactions in the Zr-Mo Region*, Phys. Rev. C **8** (1973) 1866.
- [Zwi05] G. Zwicknagel, *Electron Cooling of Ions and Antiprotons in Traps*, AIP Conf. Proc. of of COOL05 (2005) 513.
- [Zwi06] G. Zwicknagel, *Electron Cooling of Highly Charged Ions in Penning Traps*, in: M. Drewsen, U. Uggerhoj, H. Knudsen, *Non-neutral Plasma Physics VI*, AIP Conf. Proc. **862** (2006) 281.

There is a theory which states that if ever anybody discovers exactly what the Universe is for and why it is here, it will instantly disappear and be replaced by something even more bizarre and inexplicable. There is another theory which states that this has already happened.

Douglas Adams

Acknowledgments

For sure never a lone warrior has ever survived the task of completing a PhD work, so my sincere thanks goes to all the people, who made this adventure possible.

- My supervisor Priv. Doz. Dr. Wolfgang Quint for accepting me as a PhD student. Thank you for introducing me to the interesting subject of trap physics and for all the helpful insights you shared.
- Prof. Dr. Andreas Wolf for accepting to be second referee for this thesis and Prof. Dr. Jürgen Schaffner-Bielich and Prof. Dr. Max Camenzind for completing the examination committee.
- Prof. Dr. H.-Jürgen Kluge for accepting me in the atomic physics department of GSI and thus making this PhD work possible.
- Dr. Frank Herfurth for taking the load of everyday supervision and especially for the good and helpful advices on writing the thesis.
- Dr. Michael Block for the possibility to take part in the SHIPTRAP experiments and the discussions on the results.
- All my fellow PhD students - recent and former. Thanks to Christian Rauth for introducing me to the wonders of LabVIEW, Giancarlo Maero for the lively discussions (not just on HITRAP) and the new insights in the heavier side of music. Jochen Pfister and Alexej Sokolov for a nice time at Hamburg, Michael Dworschak for the great atmosphere in the office. My thanks to the rest of the Russian crew, Gleb Vorobjev and Nikita Kotovski for all the nice talks on and apart from physics.
- My sincere thanks goes to Prof. Yuri Novikov, for the lively discussions and for giving me the insight into the quest for the neutrino mass.
- Dietrich Beck and Holger Brand for the help with seemingly unsolvable LabVIEW and *CS* problems. And Falk Ziegler for the ideas and discussions on the programming of the FPGA-card.
- A special thank goes to Davide Racano, who was very patient in making different designs of coil bodies.

- Mr. Kammer from the Technologielabor for all advice and the final realization of the electronics box.
- Harald Hahn for the final layout of the printed circuit board of the preamplifier and all his insights on this side of electronics.
- Peter Moritz for his network analyzer and his advice concerning RF measurement techniques.
- Oliver Kester, Michael Kaiser, Ludwig Dahl and all the people making HITRAP happening.
- Stefan Stahl for the discussions on cryogenic electronics and the Mainz people - especially Jens Ketelaer and Stefan Ulmer - for sharing their knowledge on high Q resonant circuits for FT-ICR measurements.
- Prof. R.J. Gumby for his catchphrase, coming to use at several occasions within this work.
- All would not have been possible without the love, patience and support of my wife Nadja and my son Nathanael.
- Last, but surely not least, I want to thank Jesus Christ,
...and you carried me all the way...